ELUCIDATION OF THE COUPLING BETWEEN MECHANICAL AND BIOPHYSICAL PROPERTIES OF BIOLOGICAL MEMBRANES

A Dissertation
Presented to
The Academic Faculty

By

Hyea Hwang

In Partial Fulfillment
of the Requirements for the Degree
Doctor of Philosophy in the
School of Materials Science and Engineering

Georgia Institute of Technology

May 2019

ELUCIDATION OF THE COUPLING BETWEEN MECHANICAL AND BIOPHYSICAL PROPERTIES OF BIOLOGICAL MEMBRANESELUCIDATION OF THE COUPLING BETWEEN MECHANICAL AND BIOPHYSICAL PROPERTIES OF BIOLOGICAL MEMBRANES

Approved by:

Dr. James C. Gumbart, Advisor
School of Physics
Georgia Institute of Technology

Dr. Karl Jacob
School of Materials Science and Engineering
Georgia Institute of Technology

Dr. Hamid Garmestani
School of Materials Science and Engineering
Georgia Institute of Technology

Dr. Donggang Yao
School of Materials Science and Engineering
Georgia Institute of Technology

Dr. Peter Yunker
School of Physics
Georgia Institute of Technology

Date Approved: December 3, 2018

Research is what I'm doing when I don't know what I'm doing.

Wernher von Braun

To my mom, dad, sister, and brother,

And all of my beautiful and adorable dogs,

Without whom none of my success would be possible.

P.S. Grandma, I miss you so much.

ACKNOWLEDGEMENTS

Thanks to my coworkers in the group who have been crucial to the success of my work, and have additionally become great friends. I also thank my advisor, who made me better.

TABLE OF CONTENTS

LIST OF TABLES

LIST OF FIGURES

SYMBOLS AND ABBREVIATIONS

AA	All-atom
K_{A}	Area compressibility modulus
AMBER	Assisted Model Building with Energy Refinement
APL	Area per lipid
CG	Coarse Grain
CHARMM	Chemistry at Harvard Macromolecular Mechanics software & force-field
cryo-EM	cryo-Electron Microscopy
D	Diffusion coefficient
D_{HH}	Membrane thickness
DMPC	1,2-Dimyristoyl-sn-glycero-3-phosphocholine
DPPC	1,2-Dipalmitoyl-sn-glycero-3-phosphocholine
GAL	Galactose
GLC	Glucose
GPCR	G-protein coupled receptor
GROMACS	GROningen MAchine for Chemical Simulations
HEP	Heptose
HMR	Hydrogen Mass Repartitioning
IM	Inner Membrane
NACl	Sodium Chloride
LIPA	Lipid-A
LPS	Lipopolysaccharide, assembly of LIPA, KDO, HEP, GLC, and GAL
MD	Molecular Dynamics
NAMD	Software for nanoscale Molecular Dynamics

NPT	Simulation in constant Number, Pressure, and Temperature
OM	Outer Membrane
PAMPA	Parallel Artificial Membrane Permeability Assay
PDB	Protein Data Bank
PME	Particle Mesh Ewald Summation Method for electrostatic calculations
PMF	potential of Mean Force
POPC	1-palmitoyl,2-oleoyl-sn-glycero-phosphatidylcholine
DOPC	1,2-oleoyl-snglycero-phosphotidylcholine
QSPR	Quantitative Structure-Property Relationship
S_{CD}	deuterium order parameters
SMD	Steered Molecular Dynamics
VMD	Visual Molecular Dynamics

SUMMARY

The membranes of practically all living organisms and many viruses are made of a semipermeable lipid bilayer, which is composed of two layers of fatty acids, often containing many embedded proteins. This bilayer, a self-assembled soft material, can take on a multitude of shapes and sizes depending on its composition and its environment. It is responsible for maintaining the boundary of a cell, distinguishing inside from outside, and for selectively mediating the permeability of molecules across it. Quantifying the diverse functionality of membranes requires elucidating their mechanical properties and how those properties depend on their constituents.

The cell envelope in Gram-negative bacteria comprises two distinct membranes with a cell wall between them. There has been a growing interest in the mechanical adaptation of this cell envelope to the osmotic pressure (or turgor pressure), which is generated by the difference in the concentration of solutes between the cytoplasm and the external environment. However, it remains unexplored how the cell wall, the inner membrane (IM), and the outer membrane (OM) effectively protect the cell from this pressure by bearing the resulting surface tension, thus preventing the formation of inner membrane bulges, abnormal cell morphology, spheroplasts and cell lysis. In this study, we have used molecular dynamics (MD) simulations combined with experiments to resolve how and to what extent models of the IM, OM, and cell wall respond to changes in surface tension. We calculated the area compressibility modulus of all three components in simulations from tension-area isotherms. Experiments on monolayers mimicking individual leaflets of the IM and OM were also used to characterize their compressibility.While the membranes become softer as they expand, the cell wall exhibits significant strain stiffening at moderate to high tensions. We integrate these results into a model of the cell envelope in which the OM and cell wall share the tension at low turgor pressure (0.3 atm) but the tension in the cell wall dominates at high values ($>$ 1 atm).

The second part of the proposed research involves an estimation of small-molecule permeation through membranes, which is of critical importance for the delivery of candidate drugs to an intracellular target. In this study, we consider the membrane deformation energy as the dominant factor in crossing the membrane into cells, as measured by in vitro cell-based experiments. We have investigated a new approach using the deformation free energy of a lipid bilayer based on the principle of a continuum theory. To gain atomistic insight into the passive permeability process, we have used physics-based methods, namely molecular dynamics simulations combined with the inhomogeneous solubility-diffusion model. The estimated permeabilities from our method are compared with other popular methods such as Parallel Artificial Membrane Permeability Assay (PAMPA) experiments.

The third part of the proposed research introduces the method that can make the computational calculation faster than what it used to be required. The time step of atomistic molecular dynamics (MD) simulations is determined by the fastest motions in the system and is typically limited to 2 fs. An increasingly popular solution is to increase the mass of the hydrogen atoms to 3 amu and decrease the mass of the parent atom by an equivalent amount. This approach, known as hydrogen-mass repartitioning (HMR), permits time steps up to 4 fs with reasonable simulation stability. While HMR has been applied in many published studies to date, it has not been extensively tested for membrane-containing systems. Here, we compare the results of simulations of a variety of membranes and membrane-protein systems run using a 2-fs time step and a 4-fs time step with HMR. For pure membrane systems, we find practically no difference in structural properties, such as area-per-lipid and order parameters, and very little difference in kinetic properties such as the diffusion constant. Conductance through a porin in an applied field, partitioning of a small peptide, hydrogen-bond dynamics, and membrane mixing also show very little dependence on HMR and the time step. We also tested a 9- cutoff compared to the standard CHARMM cutoff of 12 $\AA$, finding significant deviations in many properties tested. We conclude that HMR is a valid approach for membrane systems but a 9-A cutoff is often not.

CHAPTER 1

INTRODUCTION

1.1 Gram-negative bacteria

Gram-negative bacteria are classified by the color they turn after a chemical process called Gram staining is used on them. Gram-negative bacteria stain red when this process is used. Other bacteria stain blue, which are called gram-positive. Gram-negative and gram-positive bacteria stain differently because their cell walls are different. They also cause different types of infections, and different types of antibiotics are effective against them. Gram-negative bacteria have a characteristic cell envelope structure very different from Gram-positive bacteria. Gram-negative bacteria have a cytoplasmic membrane, a thin peptidoglycan layer, and an outer membrane containing lipopolysaccharide. There is a space between the cytoplasmic membrane and the outer membrane called the periplasmic space or periplasm. The periplasmic space contains the loose network of peptidoglycan chains referred to as the peptidoglycan layer. Additionally, the Gram-negative cell envelope contains an outer membrane composed of phospholipids and lipopolysaccharides that face the external environment. The highly charged nature of lipopolysaccharides confer an overall negative charge to the Gram-negative cell wall. The chemical structure of the outer membrane lipopolysaccharides is often unique to specific bacterial strains (i.e. sub-species) and is responsible for many of the antigenic properties of these strains. Many species of Gram-negative bacteria are pathogenic. This pathogenicity is often associated with the lipopolysaccharide (LPS) layer of the Gram-negative cell envelope.

1.2 Mammalian membrane

A great deal more is known about the functions of cell membranes than is known about their detailed structure. It is a truism of molecular biology, however, that before a satisfactory understanding of the functions of any biological system can be achieved, the structure of that system must be known. Membrane fatty acid composition, phospholipid composition, and cholesterol content can be modified in many different kinds of intact mammalian cells. The modifications are extensive enough to alter membrane fluidity and affect a number of cellular functions, including carrier-mediated transport, the properties of certain membrane-bound enzymes, binding to the insulin and opiate receptors, phagocytosis, endocytosis, depolarization-dependent exocytosis, immunologic and chemotherapeutic cytotoxicity, prostaglandin production, and cell growth.

CHAPTER 2

DISTRIBUTION OF MECHANICAL STRESS IN THE *ESCHERICHIA COLI* CELL ENVELOPE

Reproduced in part with permission from Distribution of mechanical stress in the Escherichia coli cell envelope. H. Hwang, N. Paracini, J. M. Parks, J. H. Lakey, and J. C. Gumbart. *Biochimica et Biophysica Acta (BBA) Biomembranes. 1860:2566-2575, 2018.*

2.1 Introduction

The Gram-negative bacterial cell envelope consists of two distinct membranes, inner and outer, along with a thin cell wall between them. The makeup of the inner, cytoplasmic membrane (IM) is broadly similar to the canonical picture of a membrane, being composed primarily of phospholipids. Unlike the IM, however, the outer membrane (OM) is highly asymmetric and has a completely different chemical composition [1]. The outer leaflet is composed primarily of lipopolysaccharide (LPS) contrasting with the inner leaflet of phospholipids. Whereas phospholipids have two aliphatic tails, these LPS molecules are large amphiphilic molecules with around six aliphatic tails, a core oligosaccharide head group, and in many variants, a repeating polysaccharide chain termed "O-antigen" that extends into the extracellular space [2]. Divalent cations promote ionic bridging between phosphate groups on the LPS core oligosaccharides, which creates a barrier to both hydrophobic and hydrophilic molecules [3].

Despite its name, the cell wall in Gram-negative bacteria is a single-layered ($\sim$4-nm thick [4, 5]) porous mesh-like network that surrounds the cell. Although similar in composition, the cell wall in Gram-positive bacteria, which lack an OM, is roughly an order of magnitude thicker and is likely composed of multiple layers [6, 7]. The cell wall is composed of peptidoglycan, a contiguous network of strands of repeating units of the disaccharide N-acetyl glucosamine (GlcNAc)–N-acetyl muramic acid (MurNAc) that are cross-linked by short (5-10 residue) peptide side chains, all running roughly parallel to the cell surface between the IM and OM [8]. Disruption of the cell wall, e.g.,

by β-lactam antibiotics, causes inner membrane bulges, abnormal cell morphology, spheroplast formation, or cell lysis [9, 10].

The three components of the cell envelope (IM, OM and the cell wall) contribute to the mechanical stability of the cell and serve as barriers that permit selective diffusion and transport of small molecules. There has been a growing interest in the mechanical adaptation of the Gram-negative cell envelope to turgor pressure [11, 12, 13, 14, 15, 16], which is generated by the difference in the concentration of solutes between the cytoplasm and the external environment. The turgor pressure under physiological conditions has been estimated using several techniques, including chemical and mechanical measurements, with values varying by more than an order of magnitude, from 0.3 atm to 5 atm under normal conditions [17, 18, 19, 20]. However, it has yet to be addressed how the surface tension, which protects against the expansion generated by the turgor pressure, is distributed between the cell wall and both membranes. Given the separation between the cell wall and both membranes observed in cryo-electron tomograms [21, 4, 22], stress transfer is unlikely to involve direct membrane-to-wall contact except, perhaps, in extreme conditions. However, the OM is often covalently connected to the cell wall in *Escherichia coli* by Braun's lipoprotein (Lpp), the most abundant protein in this species with at least 500,000 copies per cell (Fig. 2.1) [23, 24, 1, 22], and non-covalently connected through interactions with outer-membrane proteins such as OmpA [25] and Pal [26]. While elimination of Lpp does not inhibit cell growth and division [27], elimination of both Lpp and OmpA causes *E. coli* cells to lyse unless electrolytes are added [28].

Here, we focus on resolving how the macroscopic properties of the bacterial cell envelope arise from the underlying features of its constituents. To correlate the structural characteristics of the membranes and cell wall with the mechanical resistance of the cell against the turgor pressure, it is necessary to understand the mechanical properties, e.g., elasticity, of each component. There have been a number of computational investigations into the mechanical properties of membranes. For example, pioneering simulation work by Tieleman et al. demonstrated that the application of a large mechanical pressure of -200 bar led to pore formation, i.e., a water channel, and irreversible rupture of a DPPC bilayer [30]. In another study, simulations were used to quantify the effect of membrane tension on a number of properties, such as area per lipid molecule, molecular volume, layer thickness, hydration thickness, lateral diffusion coefficient, and others, for a DOPC bilayer [31].

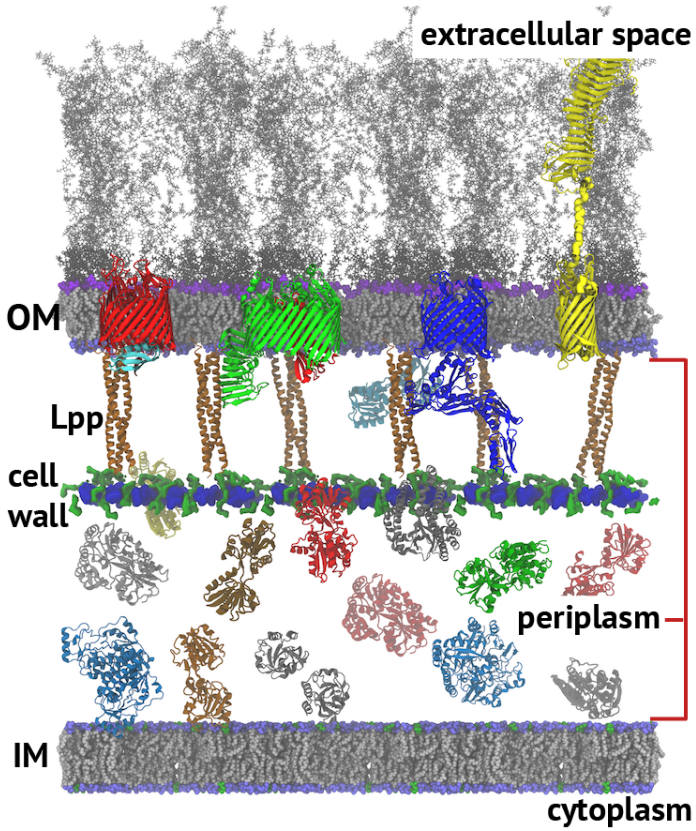

Figure 2.1: Model of the *E. coli* cell envelope. The two membranes, inner (IM) and outer (OM), along with the cell wall are labeled. The periplasm (between the membranes) is 240 Å thick. Proteins are shown to indicate scale but are of too low density [29]. Glycan strands of the cell wall are blue and peptide cross-links are green; Braun's lipoproteins (Lpp, tan) form triple-helices connecting the cell wall to the OM. From left to right, the OM proteins shown are BtuB, LptD/E, BamA, and pertactin.

Many experiments probing various mechanical properties of phospholipid bilayers have also been carried out [32, 33, 34, 35], including area compressibility [36, 37]. Recent simulations using the CHARMM36 force field [38], which is also used here, found good agreement with experiments for many of these mechanical properties, although not all; this is due in part to considerable uncertainty in the experimentally measured quantities [39].

In this paper, we carried out MD simulations of the individual components of the cell envelope (IM, OM, and the cell wall) with a variety of structural compositions, focusing on the effect of mechanical stress on each. As done in other MD simulation studies [40, 41, 42, 31, 43], our simulations utilize an applied surface tension to mimic the effect of osmotic pressure. We determined area compressibilities of the simulated membranes and compared them with those from experiments on monolayers of identical compositions. To address how proteins may alter the stiffness of the

membranes, we repeated the simulations with embedded, mechanically inert (i.e., not mechanosensitive) proteins. Lastly, we characterized the non-linear response of the cell wall to extreme stress in simulations, leading to the observation of stress stiffening.

2.2 Methods

2.2.1 Systems construction

All-atom systems were generated for all membranes and cell wall models. All membranes were periodic, thus avoiding any edge effects that would otherwise arise due to exposed hydrophobic lipid tails. Similarly, the cell-wall system was also periodic with both peptides and glycan strands covalently linked across the periodic boundaries.

Inner membrane. Two models of the inner membrane (IM) were generated. One of the IMs was modeled as a mixed 75% POPE/25% POPG bilayer [44] (Fig. 2.2A). This model contained 270 lipids in each leaflet; the full system was 140K atoms in total, including water and 150 mM NaCl (177 Na^+ and 42 Cl^- ions). The second IM model consisted of a mixture of six different kinds of saturated, unsaturated, and cyclic-moiety-containing lipids [45]. This complex membrane, referred to as Top6 (Fig. 2.2B), accurately reflects the diverse population of lipids within the *E. coli* cytoplasmic membrane. The model contained 296 PMPE, 80 POPE, 80 QMPE, 64 PMPG, 56 PSPG, and 48 OSPE lipids evenly distributed between the two leaflets; it was generated using the CHARMM-GUI membrane builder [46]. After the addition of water and 150 mM NaCl (189 Na^+ and 69 Cl^- ions) to neutralize the system, the final system size was 150K atoms.

Outer membrane. An asymmetric outer membrane (OM) model was constructed with 75% POPE/25% POPG lipids for the inner leaflet and 100% LPS for the outer leaflet (Fig. 2.3A). This LPS is the rough form from *E. coli* K-12 (i.e., no O-antigen), also known as the RaLPS chemotype. The outer leaflet contained 108 LPS molecules and the inner leaflet had 261 POPE and 87 POPG lipids (phospholipid:LPS ratio of 3.22). After the addition of water and 530 Mg^{2+}, 92 Ca^{2+}, 168 Na^+, and 168 Cl^- ions, the asymmetric OM system had a total of 300K atoms. This LPS model was validated in our previous simulations of the OM protein BtuB [47].

Addition of proteins. Biological membranes contain a substantial number of membrane proteins that are heterogeneously distributed [48, 49, 50]. A rough estimate from red blood cells is that $\sim$25% of the membrane area is occupied by proteins [51], while computational modeling has been used to predict that the maximum growth rate is achieved at 25% and 42% area occupancy for OM and IM, respectively [49]. Therefore, we have also created membranes containing *E. coli* aquaporin Z (PDB ID: 1RC2; Fig. B.2) in the IM and *E. coli* OmpF (PDB ID: 4GCP; Fig. B.5) in the OM. For simplicity, the protein occupancy was set at 25% of the lateral area for all membranes.

Cell wall. The cell walls of Gram-negative bacteria consist of a thin layer of peptidoglycan. The glycan strands consist of alternating residues of β-1,4-linked N-acetylglucosamine (GlcNAc) and N-acetylmuramic acid (MurNAc), which is a uniform composition across all bacteria. In *E. coli*, a five-residue peptide chain is attached to the MurNAc, with the sequence L-Ala (1), γ-D-Glu (2), meso-A_2pm (3), D-Ala (4), and D-Ala (5). In the mature molecule, the last D-Ala residue is lost when the peptide chain is cross-linked to the meso-A_2pm residue of another peptide [8]. The system used in this study, which had an average glycan-strand length of 17 disaccharides and a cross-linking fraction of 50%, was taken from a previous study [5]. This cell wall model was fully solvated in explicit water with K^+ ions added to the solution to neutralize its high negative charge. The initial system size with water was 19 nm $\times$ 33 nm in area and contained 545K atoms. Once the cell wall patch was stretched to over 50% of its initial area, extra water was added, resulting in a system size of 829K atoms.

2.2.2 MD simulation

Molecular dynamics simulations were carried out with NAMD 2.12 [52] for the cell wall simulations and GROMACS 5.0.2 [53] for the membrane simulations, both using the CHARMM36 force field [38, 54]. All models were solvated with TIP3P water, and ions were added to neutralize the system at a concentration of 150 mM NaCl. A constant temperature of 310 K = 37°C was maintained using Langevin dynamics (NAMD) or a Nosé-Hoover thermostat (GROMACS) [55, 56]; The pressure was coupled semi-isotropically with the Langevin piston (NAMD) [57] or the Parrinello-Rahman barostat (GROMACS) [58] at 1 atm and a coupling constant of 1.0 ps^{-1}. The x- and y-

directions were coupled independently from the z-direction. A 2-fs time step was used, and bonded and short-range nonbonded interactions were calculated every time step. Long-range electrostatic interactions were treated with the particle-mesh Ewald (PME) method [59], using a short-range cut-off of 1.2 nm; Lennard-Jones 6-12 (i.e., van der Waals) interactions were switched off between 1.0 to 1.2 nm using a force-based switching function. Buffered neighbor lists in GROMACS were maintained using the Verlet cutoff scheme. System setup, visualization, and analysis were performed with Visual Molecular Dynamics (VMD) [60].

2.2.3 Applied tension

When a periodic system consists of several phases that are separated by surfaces parallel to the xy-plane, the surface tension and the z-component of the pressure can be coupled to a pressure bath. Pressure was kept constant for all simulation runs using the semi-isotropic Parrinello-Rahman pressure coupling algorithm, with the pressure set to 5-100 mN/m (note that 1 mN/m = 1 dyn/cm). A pressure of 1 bar was always applied in the normal direction. The average surface tension $\gamma(t)$ can be calculated from the difference between the normal and the lateral pressure, resulting from the external pressure applied to the system as

$$\begin{aligned}\gamma(t) &= \frac{1}{n}\int_0^{L_z}\left\{P_{zz}(z,t) - \frac{P_{xx}(z,t)+P_{yy}(z,t)}{2}\right\}dz \\ &= \frac{L_z}{n}\left\{P_{zz}(t) - \frac{P_{xx}(t)+P_{yy}(t)}{2}\right\}\end{aligned} \tag{2.1}$$

where L_z is the length of the simulation box in the z-direction, P_{zz} is the pressure along the z axis, P_{xx} and P_{yy} are the lateral pressure in the x and y plane respectively, and n is the number of surfaces, which in this work is two.

To compute K_{A} for our systems, we ran a series of simulations in which increasingly large negative lateral pressures were imposed to stretch the membrane. Starting from an equilibrated system, a tension of 5 mN/m was targeted, simulated, and then increased by 5-10 mN/m in each subsequent simulation. Performing the simulations in this manner allowed the bilayer to respond to the applied stress, maintaining quasi-equilibrium and, thus, minimizing the disruption to the system during each incremental increase.

2.2.4 Experiments

Pressure-area isotherms. Pressure-area isotherms were recorded on a Langmuir trough (NIMA, Coventry, UK) with a total surface area of 280 cm^2 and the surface tension measured using a paper Wilhelmy plate connected to a film balance. The trough was enclosed in a custom-built case saturated with water vapor to minimize evaporation of the subphase and the temperature controlled with a water bath connected to the trough. Phospholipids and *E. coli* polar lipid extract were dissolved in chloroform while RaLPS was dissolved in a mixture of phenol, chloroform and petroleum ether (2:5:8); all the solutions were at a concentration of 1 mg/ml. The aqueous subphase was buffered at pH 7.4 with 10 mM HEPES and contained 150 mM NaCl. The calcium concentration was controlled by adding calcium chloride to the subphase while 1 mM EDTA was used to remove any residual calcium in the Ca-free subphase. Lipids were spread on the buffered water surface using a Hamilton syringe and the solvent allowed to evaporate for 15 minutes before starting the experiments. Each isotherm was repeated three times by depositing monolayers on a freshly made subphase. The compression rate was 10 cm^2/min.

2.3 Results

The mechanical properties of biological membranes determine their thickness, their ability to compress, expand, and bend. The elastic modulus, or area compressibility (K_A), characterizes the resistance of membrane to areal expansion or compression. K_A is calculated in MD simulations as the proportionality constant relating surface tension and surface area according to the equation

$$K_\mathrm{A} = A_0 \left(\frac{\partial \gamma}{\partial A} \right)_T = \left(\frac{\Delta \gamma}{\Delta A / A_0} \right)_T \tag{2.2}$$

where A is the system area, A_0 is the equilibrium area, T is the temperature (held constant at 37 °C), and γ is the surface tension. Because all of our simulations used periodic boundary conditions, the lateral dimensions of the box provide the surface area. Focusing on the linear regime of expansion, K_A was taken to be the slope of γ with respect to the fractional increase in area ($\Delta A / A_0$).

In experiments, the surface pressure of a monolayer is measured as a function of the area per

molecule in a Langmuir trough. From this relationship, K_{A} is calculated as

$$K_{\mathrm{A}} = -A_0 \left(\frac{\partial P}{\partial A_{\mathrm{M}}} \right)_T \tag{2.3}$$

where A_{M} is the area per molecule (Å^2), P is the surface pressure (mN/m), and T is the (constant) temperature (°C). We take A_0 to be the value at $P = 35$ mN/m, which is assumed to be the surface pressure of a tension-less membrane [61].

2.3.1 Determination of K_{A} of the IM from simulations

Two models of the inner membrane (IM) were constructed as described in the Methods (Fig. 2.2). Briefly, one is a two-component mixture of a 3:1 ratio of POPE:POPG, as has been used in other studies [62, 44, 45]. The other is a mixture of six types of lipids meant to be an accurate representation of the *E. coli* IM, first developed by Pandit and Klauda [45], and referred to as Top6. Each targeted surface tension was simulated for 50 ns for both IM models. The area over time for the first tension simulated for each of the inner membrane models is given in Fig. B.1, demonstrating that they reach an equilibrated state roughly halfway (25 ns) into the simulation period; similar behavior was observed at other tensions.

Averages of both the surface tension and the new area of the bilayer were calculated over the last 25 ns of each 50-ns simulation. Tension-area isotherms at 37 °C are plotted for both IMs in Fig. 2.2C, and K_{A} was determined according to Eq. 2.2. We note that each data point represents an individual simulation. The initial linear regime ($\Delta A/A_0$ between 0 and 0.35) displays an elastic response of both membranes to tension. The calculated K_{A} values are 182 $\pm$ 21 and 195 $\pm$ 23 mN/m for the POPE/POPG and Top6 membranes, respectively. Previous simulations of the same membranes produced much larger values of K_{A}, specifically 250 $\pm$ 40 mN/m for POPE/POPG and 340 $\pm$ 40 mN/m for Top6 [45]. The difference may be due to the method used; while we determined K_{A} from tension-area isotherms, Pandit and Klauda calculated it from the area fluctuations of a zero-tension simulation [45]. The latter approach has been demonstrated to depend on the length of the simulation, with very short ones ($<$ 1 ns) drastically overestimating K_{A} by nearly an order of magnitude due to poor sampling of large fluctuations [63]. However, although the simulations of

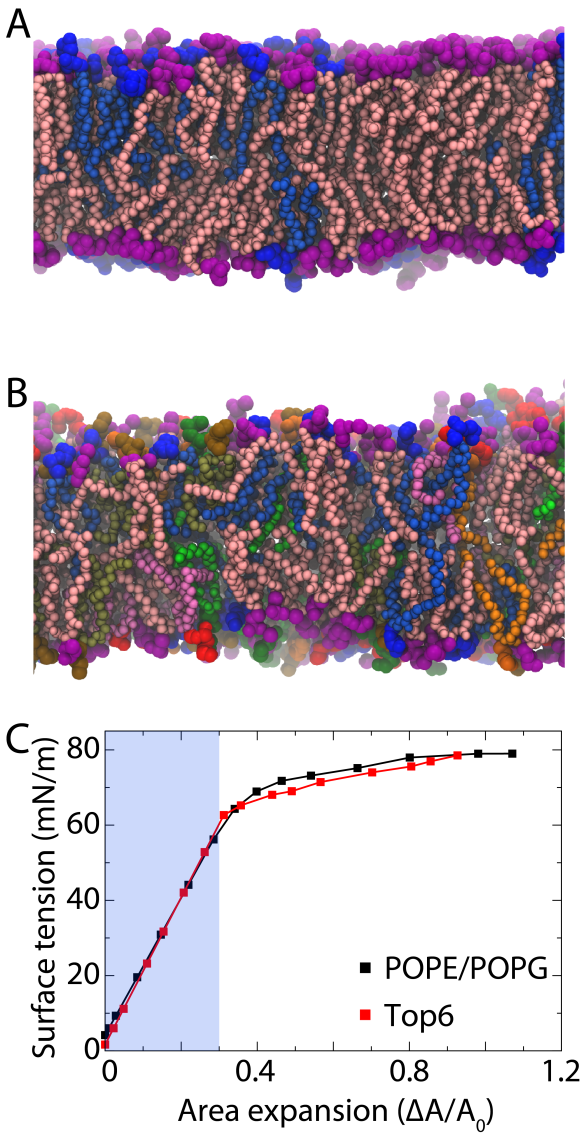

Figure 2.2: Simulation models of the inner membranes. (A) 3:1 POPE (pink tails/purple head groups):POPG (blue tails/blue head groups) bilayer. (B) Top6 bilayer (see Methods for composition). (C) Tension-area isotherms for inner-membrane models from simulation. The 3:1 POPE:POPG membrane is in black, and the Top6 membrane is in red. R^2 values from the linear regression over the initial range ($\Delta A/A_0$ between 0 and 0.35, shaded in blue) were 0.95 or higher for all IM models.

Pandit and Klauda were only 50 ns long (compared to ours, which were 50 ns per data point), more recent simulations of pure bilayers over 400 ns long produced K_{A} values greater than 200 mN/m for a variety of pure membranes [39]. We also considered finite-size effects, as our membranes are 4$\times$ larger in area than those in Pandit and Klauda (312 lipids per leaflet vs. 78) [45]; however, Venable et al. concluded that there was no consistent dependence of K_{A} on size [39]. Nonetheless, contribu-

tions from membrane undulations may be missed, particularly for small systems and/or those under applied tension [64].

To identify any effects of embedded proteins on mechanical properties of the membranes, we also simulated each IM model with an embedded aquaporin Z tetramer, which occupied 25% of the area (Fig. B.2). Using the same protocol as for the pure membranes, K_{A} was determined to be 199 ± 25 mN/m for POPE/POPG and 218 ± 26 mN/m for Top6, i.e., roughly 10% larger than the pure membranes (Fig. B.3). This increase can be explained by the relative incompressibility of the protein compared to the membrane, which focuses all of the expansion on fewer lipids than in the pure membrane system.

2.3.2 Bilayer rupture by incremental tension and stress-softening

After an initial linear portion lasting up to about 35% of the ultimate load for both IMs, the stress-strain relationship enters a new regime in which large strains are observed for small increments of stress. Unlike a bulk material where the resistance to expansion comes from intermolecular bonds, the resistance to expansion in a bilayer is a result of non-polar interactions between the hydrophobic tails of each individual leaflet. The membrane displays an initial linear response at relatively low strain since the lipids in a fluid bilayer rearrange easily under the corresponding tension. However, once it gets stretched further, the interactions between hydrophobic tails becomes weaker and the membrane undergoes a phase change (Fig. 2.2C).

We continued to apply incremental stretching to each membrane until it ruptured. Rupture occurs when a membrane reaches its critical lateral tension, which was found to be 79 mN/m and 78 mN/m for POPE/POPG and Top6 membranes, respectively (Fig. 2.2C). These values are in good agreement with other simulation results [65, 30, 40]. For example, a dipalmitoylphosphatidylcholine (DPPC) membrane withstood a surface tension of $\sim$90 mN/m prior to rupture [65]. Another study also showed that an applied lateral pressure of -200 bar ($\sim$89 mN/m for their membrane) led to the formation and expansion of a water pore [40]. At the critical tension, water pores begin to form and destabilize the membrane, which causes the pores to grow further, resulting in bilayer rupture. Both membranes ruptured at approximately double their initial, relaxed area.

When proteins were embedded in the membranes, rupture occurred at slightly lower tensions

compared to the pure membranes. This finding is consistent with the increase in K_A described in the previous section, which we attributed to the relative incompressibility of the protein. The location of the incipient water pore preceding rupture was in the middle of the membrane for both models, rather than between the protein and lipids, suggesting that the protein-lipid interactions are stronger than lipid-lipid interactions in these systems. See Figs. 2.2C and B.4 for details of the rupture events.

We also found that both membranes exhibit a strong inelastic response, or stress-softening effect, at high tension. As a membrane is stretched further, the slope of the isotherm, which gives K_A, decreases (Fig. 2.2C). This strain-induced softening has been observed in viscoelastic materials with very weak intermolecular forces, and it results in a lower Young's modulus and higher failure strain compared to other materials [66, 67]. Using the last five data points before a water pore formed in the membranes, the K_A value was as low as 15 mN/m and 26 mN/m for POPE/POPG and Top6 membrane simulations, respectively.

2.3.3 Determination of K_A of the OM from simulations

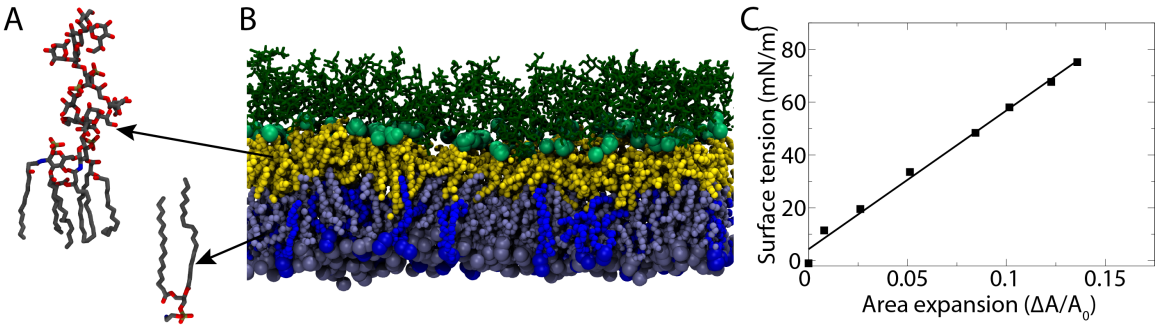

Figure 2.3: OM properties. (A) Single RaLPS molecule (left) and a POPE molecule (right). (B) Model of the OM. The hydrophobic region is shown as space-filling spheres with POPE in grey, POPG in blue, and lipid A of LPS in yellow. Phosphate groups of LPS are shown as large, light-green spheres, while phosphorus and nitrogen atoms of the inner leaflet lipids are colored grey or blue according to their type. The core oligosaccharides are shown as dark green sticks. (B) Tension-area isotherm for the OM model from simulations. The R^2 value is 0.97. See Fig. B.5 for the protein-containing OM.

Similar to the calculations done for the IM models, we determined the area compressibility moduli for a pure outer membrane and for one with embedded proteins (Figs. 2.3B and B.5, respectively). While the properties of the IM models stabilized relatively quickly (within 50 ns), the

OM models were much slower to equilibrate. This finding was not unexpected, as the diffusion constant for LPS in the OM is two orders of magnitude lower than for phospholipids, due in part to the larger size of LPS as well as the numerous divalent ions bridging them [47]. To address this slow equilibration, simulations of the OM at each target surface tension were extended to 100 ns and their properties were measured over the last 50 ns.

Unlike the IM models, which showed a linear response to tension up to a 45% increase in area, the OM was very rigid. It was only 10% stretched at a tension of ∼75 mN/m, which is the tension that caused rupture in the IM models. The calculated area compressibility modulus, $K_{\mathrm{A}} = 524 \pm 25$ mN/m, is much higher than that found for the IM; this difference in K_{A} agrees with another simulation study in which it was found that the outer membrane is more resistant than a phospholipid bilayer to rupturing via electroporation [68]. The rigidity and low mobility of the outer leaflet of the OM, composed purely of LPS molecules, are mainly attributed to the divalent (Ca^{2+}, Mg^{2+}) ion-mediated cross-links, which form an electrostatic interaction network with the negatively charged PO_4^{2-} and COO^- groups of lipid A and the core sugars that make up LPS.

We also calculated the area compressibility modulus of the OM with embedded proteins, namely an OmpF trimer occupying 25% of the area. For this protein-membrane system, we obtained $K_{\mathrm{A}} = 528 \pm 25$ mN/m, which is practically identical to that found for the pure OM (Fig. B.6).

2.3.4 Experimental determination of K_{A} of the IM

To compare with the values of K_{A} from simulations, we also carried out experiments on monolayers representative of the simulated systems, namely a 3:1 POPE/POPG mixture and *E. coli* polar lipids, the latter being roughly equivalent to the Top6 membrane simulated. Pressure-area isotherms at 37 °C were determined in triplicate using a Langmuir trough with areas ranging from ∼60-120 Å^2/lipid (Fig. 2.4A). In both cases, the monolayers remained in the liquid-expanded (LE) phase and no plateau indicating a transition to the liquid-condensed (LC) phase was observed. A surface pressure of 35 mN/m has been determined to be equivalent to the internal pressure of a bilayer in a tension-free state and also the pressure at which various monolayer properties agree best with those measured in bilayers [61]. Thus, we compared the values of A_{M} and K_{A} at a pressure of 35 mN/m to the simulation results. At this pressure, A_{M} for the POPE/POPG mixture is 69.4

$\pm$ 1.0 Å^2 and for Top6 is 63.0 $\pm$ 1.9 Å^2. Although the latter value is in good agreement with our simulated A_{M} of 62 Å^2 for Top6, the former is quite different from the simulated value of 59 Å^2 for POPE/POPG. A similar discrepancy between experimental and simulated A_{M} of 3:1 POPE/POPG monolayers emerges from a comparison between independent published results. Although an MD study found an A_{M} of 57.7 Å^2 [69], a separate investigation reported an experimental value of 65 Å^2 for the same lipid mixture under the conditions used here [70], suggesting a potential underestimation of the simulated result for this particular system.

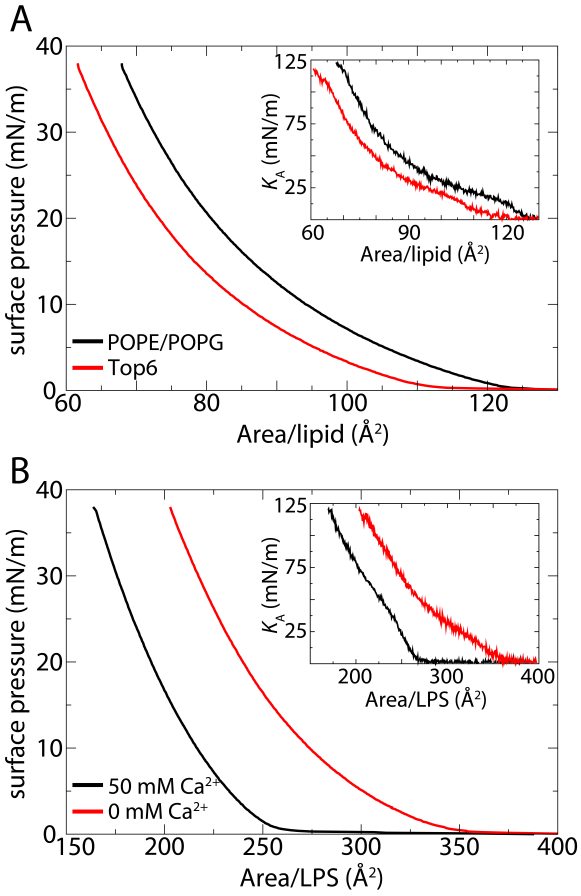

Figure 2.4: Surface pressure-area isotherms at 37 °C for monolayers from experiment. The inset in each panel shows K_{A} as a function of A_{M}. (A) IM models. The 3:1 POPE:POPG membrane is in black, and the Top6 membrane is in red. (B) OM model. Data for LPS with (black) and without (red) Ca^{2+} are shown.

Based on the surface pressure-area isotherms, K_{A} of IM was calculated according to Eq. 2.3. For both IM models, a range of K_{A} = 0 to 125 mN/m was observed. At a surface pressure of 35 mN/m, K_{A} = 123 $\pm$ 3 mN/m for POPE/POPG and 120 $\pm$ 8 mN/m for Top6. As K_{A} for a bilayer is just twice that of a monolayer [71], we conclude from experiments that K_{A} is 246 $\pm$ 6 mN/m for

POPE/POPG and 240 $\pm$ 16 mN/m for Top6 membranes under zero tension.

2.3.5 Experimental determination of K_{A} of the OM

For the outer membrane, pressure-area isotherms were determined for the longest form of rough LPS (RaLPS), which was used to model the outer leaflet in the simulations (Fig. 2.3A), at Ca^{2+} concentrations of 0 (Ca^{2+}-free) and 50 mM (Ca^{2+}-loaded). The latter concentration, well above the physiological concentration, was employed in several previous studies to investigate the effects of Ca^{2+} on LPS monolayers and is expected to saturate all Ca^{2+} binding sites on LPS [72]. Unsurprisingly, A_{M} was much higher when no Ca^{2+} was present, due to the repulsion of the negatively charged groups on LPS, which are normally bridged by divalent cations, allowing for much tighter packing [73]. At a surface pressure of 35 mN/m, A_{M} was 207.8 $\pm$ 4.9 Å^2 for the Ca^{2+}-free state and 168.6 $\pm$ 1.4 Å^2 for the Ca^{2+}-loaded state (Fig. 2.4B).

To our knowledge, these are the first RaLPS monolayers to be characterized at 37 °C. Thus, we also collected isotherms at 21°C (Fig. B.7) to enable comparison with the published values for these systems. At this temperature and 35 mN/m, we obtained an A_{M} of 187.9 $\pm$ 1.3 Å^2 in the absence of Ca^{2+} which decreased to 156.2 $\pm$ 3.2 Å^2 in the presence of 50 mM Ca^{2+}. These values are in good agreement with those reported by previous studies, both differing by less than 10% [72].

The area compressibility varied from K_{A} = 0 to 120 mN/m (Fig. 2.4B). Surprisingly, this compressibility of RaLPS is similar to the IM models, despite its apparent stiffness in the simulations. At a surface pressure of 35 mN/m, K_{A} for Ca^{2+}-loaded RaLPS was 120 $\pm$ 8 mN/m and for Ca^{2+}-free RaLPS, it was 117 $\pm$ 3 mN/m. The resistance to expansion in a bilayer is a result of the extra hydrophobic area exposed to water upon pulling the lipids apart. Therefore, K_{A} for a bilayer is taken to be twice that for a monolayer, as done in previous studies [61, 71]. In this work, because the OM is asymmetric, we combined K_{A} for the outer leaflet of LPS with K_{A} for the Top6 monolayer, which is representative of the inner leaflet of the OM, giving $K_{\mathrm{A}} = 237$ mN/m for the Ca^{2+}-loaded OM at zero tension.

2.3.6 Determination of K_A for the cell wall from simulations

The cell wall, a cross-linked polymer mesh of peptidoglycan (PG), is located in the periplasm between the IM and OM and is assumed to bear the majority of the turgor-pressure-induced stress [74]. The tensile elasticity, or Young's modulus, has been calculated previously from simulations for a specific arrangement of PG and was found to be anisotropic with $E_{\mathrm{circum.}} = 66.3\,\mathrm{MPa}$ and $E_{\mathrm{lateral}} = 17.5\,\mathrm{MPa}$ [5], in agreement with AFM experiments [75]. The stiffer direction corresponds to the glycan strands encircling the cell circumferentially, and the more flexible direction corresponds to the peptide crosslinks that bridge the strands laterally [4, 76]. While previous simulations have focused on the elastic regime, we have performed additional simulations here to quantify the degree of strain stiffening, which has been observed for other biopolymer networks [77, 66, 67], including the cell wall [20].

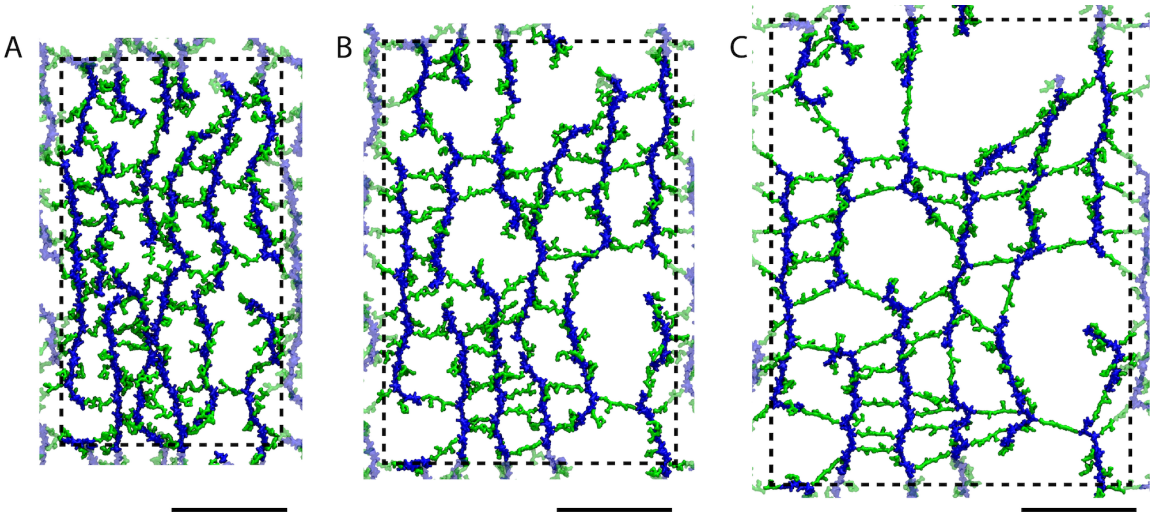

Figure 2.5: Representative states of the cell wall. Glycan chains are shown in blue and peptide cross-links in green; the cross-linked fraction of peptides is 50% [5]. The scale bar below each image is 10 nm. (A) Relaxed cell wall. (B) Cell wall stretched to 1.5× its original area. (C) Cell wall stretched to 2× its original area. Although covalent bonds cound not be broken in the simulations, we saw no change in average bond lengths in any simulations (Fig. B.8B).

Rather than treating the two axes of the cell wall individually as done previously [5], multiple surface tensions were applied sequentially to a representative model patch of peptidoglycan and the resulting area change was monitored over a 10-ns simulation (see Methods). This patch, taken from a previous study [5], was first allowed to relax for 20 ns under zero applied tension, resulting in the configuration shown in Fig. 2.5A. Even with a very small applied surface tension of 6 mN/m, the

area of the cell wall expanded to over 40% of its initial value (Fig. 2.6). Most of this expansion was due to the softer peptides, which expanded by ∼30%, compared to the glycans, which expanded by only 10% (Fig. B.8A). While extraordinarily soft at low tension, greater tensions applied to the cell wall quickly revealed strain stiffening behavior as expected. For example, at the highest tension applied, more than 11× the lowest tension (∼68 vs. 6 mN/m), the cell wall expanded by just over 100%, i.e., doubling its original area (Fig. 2.5C). This expansion arose from a 68% increase in the peptide direction and a 23% increase in the glycan direction. Although the peptidoglycan is apparently highly stretched at this expansion, it has not reached its elastic limit; average bond lengths in the glycan and peptide directions varied by 0.5% at most across all simulations (Fig. B.8B).

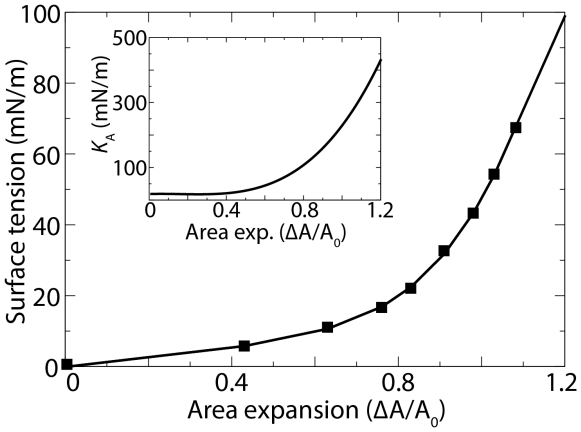

Figure 2.6: Tension-area isotherms for the cell wall model from simulation. The inset shows K_{A} as a function of the change in area due to applied tension. Standard deviation of the tension was ∼3 mN/m, contributing to an error in K_{A} of at most 2%.

To compare with the values of K_{A} from IM and OM simulations, K_{A} of the cell wall, $K_{\mathrm{A}}^{\mathrm{CW}}$, was calculated according to Eq. 2.2, and the full isotherm is plotted in Fig. 2.6 (inset). While at low expansions, the compressibility is negligible, it quickly rises to over 200 mN/m at 100% expansion, i.e., comparable to those for the IM models from both simulations and experiments. In a living bacterial cell, the cell wall is strained, as upon cell lysis it shrinks by as much as 45% in area [78]. The cell wall shrinks mainly along the long (peptide) axis, forming wrinkles, with no change observed in the circumference in electron cryo-tomography (ECT) images [4]. Experiments in which *E. coli* are subjected to hyperosmotic shock show an ability to shrink 33% in area, i.e., the cell wall $\Delta A/A_0 = 0.5$ where A_0 is the relaxed area [79, 16], and, in extreme cases, over 50% in area ($\Delta A/A_0 = 1.25$) [16]. This range of $\Delta A/A_0$ for our model of the cell wall predicts $K_{\mathrm{A}}^{\mathrm{CW}}$

ranges from 29 to 500 mN/m (Fig. 2.6). We also note that the spacing in our relaxed model between strands is 2-4 nm (Fig. 2.5A), in agreement with findings from AFM for cell wall fragments [76]; however, neither account for the ability of the continuous, intact cell wall to form wrinkles, which would shrink its area even further.

2.4 Discussion

Bacterial cells are very crowded due to the presence of metabolites and macromolecules, which can occupy a significant fraction of the total cellular volume (up to 30%) [80, 81]. When compared to the external environment, the cell interior usually possesses a higher concentration of solutes, resulting in turgor pressure. This results in a net water influx and cytoplasmic expansion which, when limited by the cell envelope comprising the IM, OM, and cell wall, results in turgor pressure. The turgor pressure in turn induces surface tension in the cell envelope. In this work, we have performed MD simulations of atomistic lipid bilayers and a model of the cell wall to gain insight into the distribution of surface tension between these three components of the cell envelope. K_{A} of each cell envelope component was determined from simulations and, for the IM and OM, compared to that derived from experimentally determined pressure-area isotherms.

The agreement between simulated and experimental values of K_{A} was mixed. For both IM models, simulations underpredicted the experiments by 15-25%: K_{A} for POPE/POPG was 182 mN/m in simulations and 238 mN/m in experiments, whereas for Top6, it was 195 mN/m in simulation and 226 mN/m in experiment. For the OM, simulations dramatically overpredicted the experimental result: K_{A} was 524 mN/m in the simulation and only 233 mN/m in the experiments. It is surprising that our experimental compressibilities for phospholipid (113-119 mN/m) and LPS (110-120 mN/m) monolayers are nearly identical given their significantly different structures (Fig. 2.3A). Similar experiments on monolayers of other LPS variants have found a range of K_{A} values, e.g., from 130 mN/m for *Salmonella enterica* ReLPS (an LPS variant shorter than RaLPS) [82] to 225 mN/m for *Pseudomonas aeruginosa* LPS [83]. X-ray studies of LPS at the air-water interface revealed the coexistence of crystalline domains and compressible disordered regions in the monolayer, with the former prevailing at higher surface pressures [84]. The low compressibility obtained in the simulations might indicate that the in silico model of an LPS leaflet displays properties similar to the

crystalline regions observed in the X-ray studies, possibly due the slow diffusion of LPS and the limited timescale of the simulation [47]. On the other hand, the presence of the more compressible disordered regions in the monolayer at the air-water interface would explain the lower K_{A} measured experimentally.

Additional simulations were performed with transmembrane proteins to determine whether their presence alters the stiffness of membranes. In both the IM and OM models, inclusion of proteins at a physiological protein density of 25% had at most a minor effect on K_{A}. Membrane proteins (AqpZ) in the IM made both POPE/POPG and Top6 membranes stiffer by $\sim$10% (199 mN/m and 218 mN/m, respectively). This finding is consistent with coarse-grained simulations, which showed that the bending rigidity increased when aquaporin was in the membrane at a similar density [85]. In contrast, membrane proteins (OmpF) in the OM had practically no effect on K_{A}. The effect on K_{A} may be protein-dependent, as demonstrated previously for BtuB and OmpF, which have similar shapes but different effects on the rigidity of the membrane [85]. However, those simulations were performed in a phospholipid membrane that did not contain LPS, which clearly plays a role in the mechanical properties of simulated membranes, and also forms specific LPS-OmpF complexes [86].

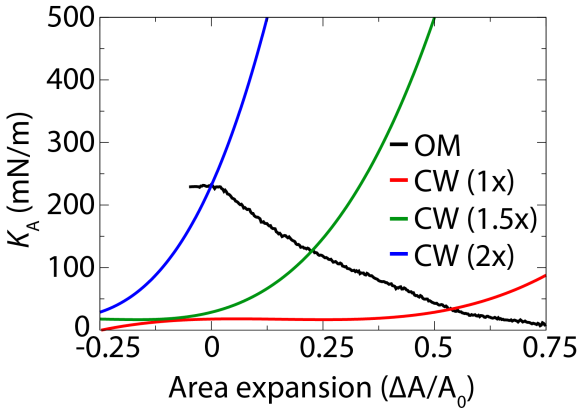

Figure 2.7: Strain-dependent area compressibility of the cell wall (CW) from simulations and the outer membrane (OM) from experiments. The cell wall is shown for three different assumed values of A_0. Due to strain stiffening, for a pre-strained cell wall, K_{A} rises drastically over a small range of ΔA. See Fig. 2.5 for images of the cell wall at the same pre-strained values, i.e., $1\times$, $1.5\times$, and $2\times$ the fully relaxed area.

If we assume that all three components of the cell envelope share the tension resulting from turgor pressure, we can calculate the fraction of tension each component bears based on their mechanical properties (see Appendix B). From just a few inputs, including a turgor pressure of 1 atm

and our measured K_{A} values for the IM and OM, we find that $K_{\mathrm{A}}^{\mathrm{CW}}$ = 1386 mN/m and 1161 mN/m when using $K_{\mathrm{A}}^{\mathrm{OM}}$ of 233 mN/m (experiment) and 524 mN/m (MD simulation), respectively. Both calculated $K_{\mathrm{A}}^{\mathrm{CW}}$ values are nearly an order of magnitude higher than the value calculated from our simulations; furthermore, these values imply a tensile elasticity of 336 MPa and 281 MPa, which are also both an order of magnitude greater than practically all experimental estimates (see Ref. [87] and references therein). This discrepancy cannot easily be resolved by assuming a different Poisson's ratio for the membranes, and it only grows for larger values of the turgor pressure. Under these assumptions, the IM and OM each bear 10% of the tension and the cell wall bears 80%.

If, however, the turgor pressure is more modest, e.g., 0.3 atm as measured in some experiments in growth media [20, 19], we find $K_{\mathrm{A}}^{\mathrm{CW}} = 167$ mN/m using the experimental $K_{\mathrm{A}}^{\mathrm{OM}}$ = 233 mN/m. This value is slightly less than that found in our simulations of the cell wall at $2\times$ its relaxed area (Fig. 2.6). In this case, each of the three components, IM, OM, and cell wall, has the same amount of tension (one third of the total). If the IM does not participate directly in bearing the turgor pressure, then $K_{\mathrm{A}}^{\mathrm{CW}}$ = 342 mN/m, again using $K_{\mathrm{A}}^{\mathrm{OM}}$ from experiment. This $K_{\mathrm{A}}^{\mathrm{CW}}$ occurs at only 6% area expansion beyond the assumed $2\times$ starting point (Fig. 2.7). In this case, the cell wall bears two-thirds of the tension and the OM bears the remaining one-third. Other possible distributions are presented in Table B.1.

As O-antigen, which is usually present in pathogenic *E. coli* strains, is attached to the core oligosaccharide, one might assume that it will have an effect on the elasticity of the OM. Although the K-12 strain, which lacks O-antigens, was modeled here, a recent study found that the stiffness of *E. coli* cells increased when the O8 antigen, an electrically neutral linear poly-mannose, is present [16]. Thus, we expect that the OM in O-antigen-presenting bacteria would bear an even higher tension than that calculated above.

Recent work from Huang and colleagues also investigated the mechanical properties of the Gram-negative cell envelope [16]. Based on experiments in which the *E. coli* OM, cell wall, or both was compromised and then subjected to hyperosmotic shock, they concluded that the OM is an essential load-bearing element in addition to the cell wall, in agreement with our conclusions here, especially at low (0.3 atm) turgor pressure (Table). They also found that the cell wall length was between 25% and 50% expanded from its most relaxed state [16]. Using a simple model of *E. coli* as

a cylinder of radius r, length $2r$, and capped by hemispheres of radius r [88], this change in length translates to an area expansion of $\sim$1.5-2.25$\times$ the relaxed cell-wall area in the living cell. This area expansion is precisely the regime where we see overlap of the K_{A} values of the cell wall and OM. In particular, when the cell wall is twice its relaxed area, $K_{\mathrm{A}}^{\mathrm{CW}}$ is identical to $K_{\mathrm{A}}^{\mathrm{OM}}$(Fig. 2.7), further supporting the conclusion of Rojas et al. that the OM and cell wall share the mechanical load due to the turgor pressure.

In conclusion, the high predicted $K_{\mathrm{A}}^{\mathrm{CW}}$ values suggest that a turgor pressure of 1 atm is not feasible for the *E. coli* K-12 strain regardless of whether or not the IM plays a role in bearing it. At a turgor pressure of 0.3 atm, the cell wall can bear 0% – 65% of the pressure, depending on $K_{\mathrm{A}}^{\mathrm{OM}}$ and whether or not the IM contributes. Assuming that the true K_{A} of the OM is between our experimental and simulated values, it bears 35% – 78% of the 0.3-atm turgor pressure. Lastly, we demonstrated the inelastic behavior of the cell wall. When the turgor pressure rises due to an osmotic downshock, which is caused by a sudden decrease in the solute concentration outside of a cell, the distribution of surface tension will shift toward the cell wall bearing an increasingly large fraction of the tension, due to its ability to undergo strain stiffening, effectively increasing its K_{A}, in agreement with previous measurements [20].

CHAPTER 3

THEORETICAL AND COMPUTATIONAL INVESTIGATIONS INTO LIPID BILAYER PERMEATION OF DRUGS

3.1 Introduction

Transport across biomembranes is essential for a number of cellular functions and also becoming increasingly important in many medical, pharmaceutical and environmental technologies [89]. For example, drug permeation is crucial for their effective delivery to intracellular targets and is at the basis of the technology of liposomal transport systems. Although many important permeation mechanisms, such as those responsible for the translocation of sugars and amino acids, are actively controlled by proteins, passive permeation is the most common way by which solutes cross cell membranes. Therefore, the study of passive drug absorption is of critical importance in drug development. The path of a drug from the site of administration to its target cells or compartments requires the crossing of several semipermeable cell membranes, making it relevant to be able to predict whether and to which extent a molecule can pass through the cell membranes.

From an experimental point of view, data on permeability can be obtained by experimental studies such as the Parallel Artificial Membrane Permeability Assay (PAMPA) [90, 91], the human colon adenocarcinoma (Caco-2) cell line assay [92, 93], the Madin-Darby Canine Kidney (MDCK) cell assay [94], among others. However, since these experiments can be time consuming and expensive, they are only performed only after the number of candidates has been significantly culled. Moreover, experimental approaches cannot provide adequate information on mechanism or structural information of passive transport at the molecular level.

As a result of the aforementioned limits, several well-characterized in silico permeability prediction methods have been developed. One popular example is Quantitative Structure-Property Relationship (QSPR) [95]. This is an informatics-based predictive method using statistical correlations and learned models (e.g. regression models, neural networks, Bayes models, etc.). However, due to the nature of linear response training models, QSPR methods exhibits mediocre predictive

performance when compared across a broad range of experimental test sets [96, 97, 98]. Despite advances in these technologies, neither experimental nor QSPR methods provide detailed atomistic insight into the biophysics of membrane permeation.

To gain atomistic insight into the passive permeability process, physics-based methods, such as molecular dynamics (MD), have become increasingly popular. Molecular dynamics (MD) simulation is a powerful technique yielding atomic details that are not available in experiments. Most MD studies evaluate membrane permeability using the solubility-diffusion model, which traditionally has been used to study the membrane permeation of small molecules. The bulk solubility-diffusion model of permeability was proposed [99] in which lipid membranes were considered as homogeneous bulk bodies. Later work [100] accounted for the heterogeneity of membranes by developing the inhomogeneous solubility-diffusion model, whereby the permeation coefficient P of a solute through a membrane can be predicted as

$$R = \frac{1}{P} = \int_{z_1}^{z_2} \frac{\exp[W(z)/k_B T]}{D(z)} dz \tag{3.1}$$

where k_B is Boltzmann constant, T is the temperature, and z is a collective variable describing the relative position of the solute along the transmembrane axis, with z_1 and z_2 representing the bulk water regions on the two sides of the membrane. Mathematically, the potential of mean force (PMF), $W(z)$, and local diffusivity coefficient, $D(z)$, are related to the resistivity, R, and both $W(z)$ and $D(z)$ can be estimated from MD simulations, provided that all zs are well sampled. $W(z)$ can be obtained by using various sampling techniques, e.g., umbrella sampling (US) [101], adaptive biasing force (ABF) [102, 103], or metadynamics [104]. Although these techniques are frequently used to obtain sufficient sampling of transition states, since conventional MD is not ideal for sampling transition states, they are computationally very expensive. Even the calculation of PMFs of small solutes requires a sampling period of at least 10 ns per window, which can add up to 1 μs or more [105, 106].

In this work, we suggest that the membrane deformation energy is the dominant factor in drug absorption and permeation. Instead of using computationally expensive sampling methods, we propose a novel way to predict the permeation of drugs by calculating membrane deformation free

energy (See Methods and Results). With this approach, it requires less than 100 ns of simulation time to estimate the permeability. We used Steered MD (SMD) simulation for 15 drugs with two different membranes, a simple DMPC membrane and a complex mammalian membrane, to observe the effect of lipid composition on membrane deformation by a drug. The estimated permeabilities from our method are compared with other popular method such as PAMPA and QSPR.

3.2 Methods

3.2.1 System construction

We constructed two model membrane bilayers, one consisting of pure DMPC (1,2-dimyristoyl-sn-glycero-3-phosphocholine) and one mimicking the mammalian membrane, using the CHARMM-GUI membrane builder [46]. We generated two different size for each membrane system; the small and large membranes contain 53 and 150 lipids per leaflet, respectively. Our model of mammalian membrane is based on rat liver plasma membrane [107, 108] (see Table. 3.1 and 3.2 for the details of lipid composition). All models were solvated with TIP3P water, and ions were added to neutralize the system at a concentration of 150 mM NaCl. Both membranes are equilibrated for 100 ns before starting the production simulations.

In this study, we have chosen fifteen small-molecule compounds (acyclovir, lisinopril, tetracycline, azithromycin, chlorothiazide, pravastatin, indinavir, ketoconazole, ritonavir, chlorpromazine, acetaminophen, ibuprofen, diphenhydramine, tamoxifen, levodopa) which cross the cell membrane by passive diffusion, and for which experimental $\log P$ values are available [109, 110, 111]. The $\log P$ values and other molecular property values have been documented in SI (Table S mol.pro). Most importantly, these compounds cover a wide range of $\log P$, between -6.52 and -2.43, and molecular size, between 151.17 and 748.99 g/mol, as evenly distributed as possible.

Lipid	Number	Percentage
Cholesterol	50	25.0
PC (Phosphatidylcholine)	60	30.0
PE (Phosphatidylethanolamines)	33	16.5
SM (Sphingomyelin)	38	19.0
PS (Phosphatidylserine)	11	5.5
PI (Phosphatidylinositol)	8	4.0
TOTAL	200	100.0

Table 3.1: Lipid headgroup distribution by number per leaflet (left) and percentage (right).

Tail	PC	PE	SM	PS	PI
16:0	30	30	20	12	12
18:0	30	35	24	50	50
18:1	10	7	8	5	5
18:2	15	13	6	5	5
20:4	15	15	16	28	28
24:0	-	-	24	-	-
Total	100	100	100	100	100

Table 3.2: Fatty acid distribution by percentage; Palmitic acid (16:0), Stearic acid (18:0), Oleic acid (18:1), Linoleic acid (18:2), Arachidonic acid (20:4), and Lignoceric acid (24:0)

3.2.2 Membrane deformation free energy

The elastic properties of lipid bilayer membranes that are regarded as continuous media have been studied in many different contexts. These studies ranged from local phenomena, such as lipid-protein interactions [112], to the shape fluctuations (the flicker phenomenon) of whole cells [113]. During the last decade or so, ingenious techniques were developed to measure the basic elastic

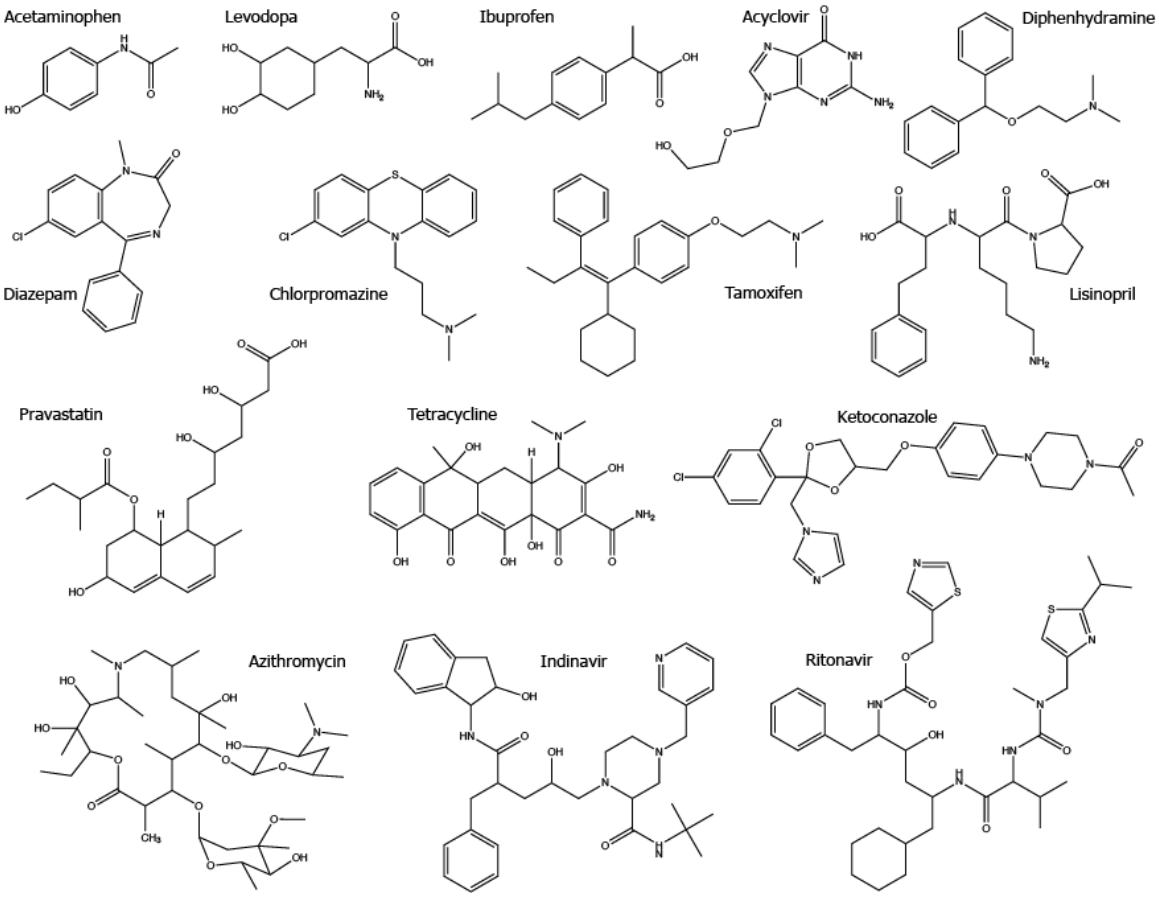

Figure 3.1: Skeletal chemical structures of the permeants simulated in this study.

constants of membranes, such as the thickness compressibility, the surface tension coefficient, the lateral compressibility, and the curvature elastic modulus [114, 115, 116].

The elastic deformation of the bilayer surrounding a channel is approximated with a model developed by previous studies [117, 118], and Huang (1986) [119] has applied this model to calculate the deformation energies induced by inclusions. These calculations have been elaborated upon by others: notably by Andersen and co-workers [120, 121, 122] and Dan and co-workers [123, 124]. Specifically, Goulian et al. [122] have studied a similar model including applied tension. The bilayer deformation energy in this model is given by

$$\Delta G_{mem} = \frac{1}{2}\int_{\Omega}[\frac{K_{\alpha}}{L_0^2}(u)^2 + \frac{K_c}{2}(\nabla^2 u^+)^2 + \frac{\alpha}{2}(\nabla u^+)^2]dxdy \tag{3.2}$$

where K_a is the area compressibility modulus, K_c the membrane bending modulus, α is the surface tension, L_0 is the equilibrium thickness of the membrane, and u is the deviation of the leaflet height(h) from its equilibrium value, u = h - L_0/2.

3.2.3 MD simulation

Molecular dynamics (MD) simulations were carried out with NAMD 2.12 [52]. The CHARMM General Force Field (CGenFF) program [125, 126] was used for atom typing and assignment of parameters for the drugs, and all simulations were run using CHARMM36 parameters [127].

A constant temperature of 310 K was maintained using Langevin dynamics; The pressure was coupled semi-isotropically with the Langevin piston [57] at 1 atm and a coupling constant of 1.0 ps^{-1}. A 2-fs time step was used. Bonded and short-range nonbonded interactions were calculated every time step, while long-range electrostatics were calculated every other time step using the particle-mesh Ewald (PME) method [59]. Visualization was done with Visual Molecular Dynamics (VMD) [60] and analysis was performed with Matlab and Mathematica.

3.3 Results

In the solubility-diffusion model, the PMF is a critical component of the permeability (see Eq. 3.1). Given its exponential weighting, the PMF may be considered the greatest contributor to the perme-

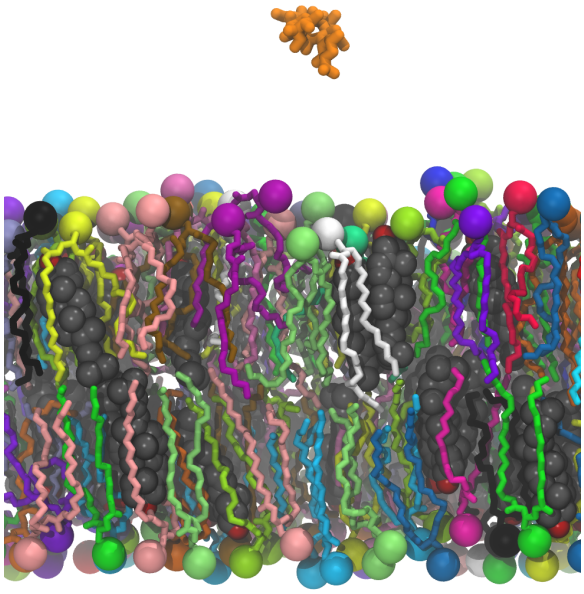

Figure 3.2: A snapshot of a drug on top of the membrane. Cholesterol molecules are shown as grey spheres. The phosphorus atoms of the lipid head groups are also shown as spheres; lipids are colored differently according to their type.

ability, making its accurate calculation of paramount importance. Rather than calculate the PMF directly, however, we have considered membrane deformation as the dominant factor in the PMF; the deformation energy calculation is detailed below.

3.3.1 Steps to calculate the membrane deformation energy (ΔG_{mem})

After each membrane was equilibrated for 100 ns, one of the 15 drugs studied here was added to the system. The drug was positioned in the water domain about 20 $\mathring{A}$ away from the phosphorus atoms of the leaflet (Fig. 3.2). In this work, a constant-speed Steered MD (SMD) simulation was performed to pull the drugs from outside of the membrane to the center of the membrane at a speed of 0.5 $\mathring{A}$/ns. Fig. 3.3A shows a perturbed membrane with a drug near the center of the membrane as a result of this SMD simulation.

The coordinates of phosphorus atoms of the upper leaflet were saved every 200 ps. Five frames that contain the lowest z-positions of the phosphorus atoms were selected, and all other phosphorus atoms except the ones within 15 $\mathring{A}$ of the lowest phosphorus atom were excluded for fitting

(Fig. 3.3B). The positions of the phosphorus atoms were considered the representative data points of the shape of the upper leaflet of the perturbed membrane and were fitted to the second order polynomial equation as

$$u(x, y) = p_0 + p_1 x + p_2 y + p_3 x^2 + p_4 xy + p_5 y^2 \tag{3.3}$$

where p_0, p_1, p_2, p_3, p_4 and p_5 are constants. This $u(x, y)$ is plugged into Eq. 3.3 to calculate ΔG_{mem}.

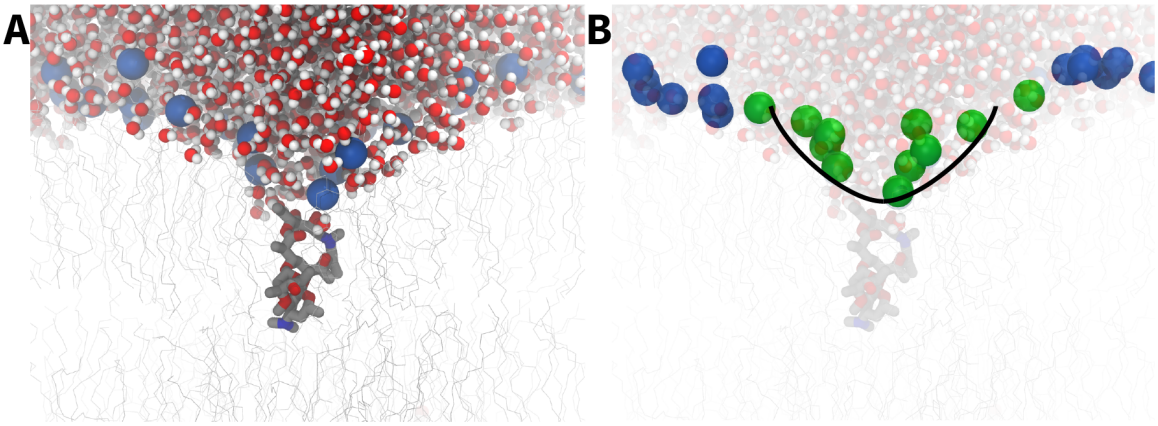

Figure 3.3: Snapshots of a drug in the membrane. (A) A perturbed membrane with a drug pulled to the center of the membrane. Phosphorus atoms are shown as blue spheres and water molecules are in red/white VDW representation. (B) Water molecules, membrane, and a drug are transparent. Phosphorus atoms that are within 15 $\mathring{A}$ of the phosphorus atom at the lowest z position are in green, and the rest is in blue. The black line indicates the fitted curve in 1D.

3.3.2 Compare log*P* value with RRCK and PAMPA experiments

To calculate permeability, as in Eq. 3.1, we need two variables; $W(z)$ and $D(z)$. While $D(z)$ depends on z position, we considered it as a constant value in this work: 15×10^{-6} cm^2/s at the outside of the membrane and 1×10^{-6} cm^2/s at the middle of the lipid tails and at the center of the membrane. With our calculated ΔG_{mem} value, which was used as a value at the peak of $W(z)$, we interpolated the full $W(z)$. To compare with the experimental values, log$P$ was determined according to Eq. 3.1. Table 3.3 shows the log$P$ values from the simulations and experiments.

The values from simulations are averaged over 5 frames that were chosen based on the lowest position of the phosphorus atoms, and each simulation was ran twice (giving a total of 10 frames) for

Drug	RRCK	PAMPA	MAM.	DMPC	Drug	RRCK	PAMPA	MAM.	DMPC
Acyclovir	-6.52		-6.2	-6.52	Ritonavir	-5.08	-1.68	-5.42	-5.74
Lisinopril	-6.30	-6.7	-5.98	-5.9	Chlorpromazine	-4.99	-0.22	-5.21	-5.32
Tetracycline	-6.15	-5.54	-5.99	-6.41	Acetaminophen	-4.91	-5.82	-3.43	-4.12
Azithromycin	-6.15		-6.23	-6.9	Ibuprofen	-4.52	-4.92	-2.97	-2.53
Chlorothiazide	-5.89		-5.32	-5.99	Diazepam	-4.44	-2.44	-4.73	-5.53
Pravastatin	-5.68		-5.43	-5.78	Tamoxifen	-4.241	0.78	-4.14	-5.15
Indinavir	-5.47	-3.6	-5.78	-5.62	Levodopa	-3.78	-7.52	-3.1	-3.98
Ketoconazole	-5.38	-1.46	-5.69	-5.89					

Table 3.3: log$P$ values of 15 molecules from simulations and experiments. The unit of P is cm/s. Experimental values are obtained from [109, 110, 111].

all the simulations with a speed of 0.5 $\mathring{A}$/ns. We also simulated three of the systems (Azithromycin, Pravastatin, and Acetaminophen) with a SMD simulation with a speed of 1 $\mathring{A}$/ns to see the effect of a different speed of pulling the drug, and also with a smaller mammalian (53 lipids and 17 cholesterols per leaflet) membrane to see the size effect of the membrane. The results can be found in SI. Fig. 3.4 shows a correlation between RRCK data and predicted permeability using our described method in this work, which showed a good ability to predict relative permeability among compounds.

In this work, it is substantial to use experimentally measured permeability data under consistent conditions, for highly diverse classes of drugs with a wide range of molecular sizes. For this reason, to compare with our measured values, we use primarily data generated by Pfizer, Inc. from in vitro RRCK (Ralph Russ Canine Kidney) cell-based permeability assay, which uses an MDCK cell line with a low expression of P-glycoprotein and has exhibited lower active efflux than both the MDCK-WT and Caco-2 cell lines [128]. Based on R^2 values shown in Fig. 3.4, all the permeability derived from the simulations are within 1-2 order of magnitude from the experimental value measured in RRCK assay. PAMPA experiments predict permeability poorly for the chosen data set with anR^2 value of 0.0297. Although there are five drugs that don't have PAMPA values to compare, this R^2 value indicates that PAMPA experiments are not reliable at all. For our predicted value using membrane deformation energy, we found that our complex mammalian membrane predicted better (R^2 value of 0.7184) than a simple DMPC membrane (R^2 value of 0.5145). This finding was expected because the mammalian membrane has 25% cholesterol, which makes it thicker and stiffer so it is closer to the real membrane that drugs have to pass through.

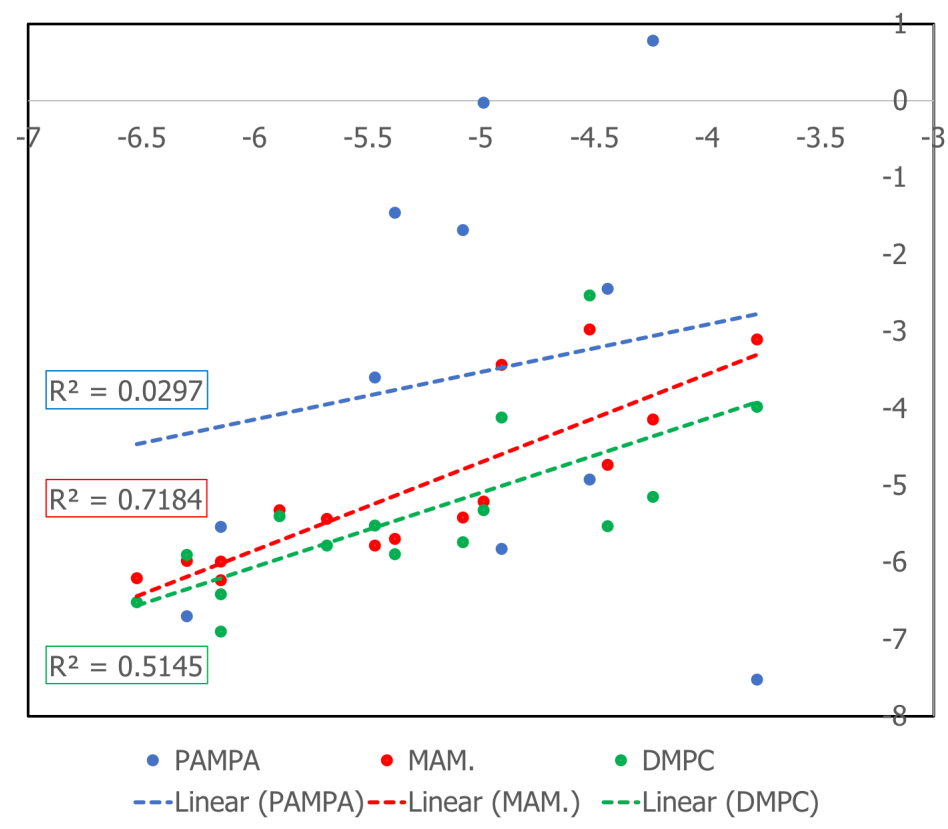

Figure 3.4: Correlation between RRCK data with PAMPA (blue) and predicted permeability; mammalian (red) and DMPC (green) membranes. Dashed lines show the linear fitting of PAMPA and predicted values to the experimental RRCK data.

3.4 Discussion

Defining the physicochemical properties of bilayer defects may allow advances in drug delivery and novel therapeutics and improve our understanding of membrane protein structure and function. Here, we consider the membrane deformation energy as a dominant factor in drug absorption, rates of crossing the barrier, and simply entering cells, as occurs in in vitro cell-based experiments. The deformation free energy of a lipid bilayer is presented based on the principles of a continuum theory [119].

In this work, we introduced a novel way to predict log$P$ using ΔG_{mem} by calculating membrane deformation energy. We still use the solubility-diffusion model, which is typically used for permeation prediction, but with our method, we can save up to 10 times the computational resources over traditional MD-based approaches. We found that calculating log$P$ using our method can predict it fairly well, especially compared to PAMPA experiments. As R^2 values are commonly used to compare different methods, our mammalian membrane has the highest values of 0.7184. While a simple DMPC membrane is still better than PAMPA, its R^2 value of 0.5145 is still not good enough to be used to predict permeability. By comparing these two different results from different membranes, we found out that the membrane composition is important for calculating permeability computationally. Mammalian membranes have 25% of cholesterol, and also extremely long fatty acid tails (24:0). This different composition of lipids changes membrane characteristics, and as a result, affects the penetration of the membrane by the drug. Along the same lines, since a DMPC membrane is thinner and softer, the drug tends to perturb it more than the mammalian membrane.

The free energy of flip-flop (Gflip-flop) may then be determined as the free energy cost to move from the free energy minima (in this case, the membrane partitioned position, approximately 10 from the bilayer center) to the membrane core.

One limitation of this work is that we assume the membrane composition is the same in both leaflets, and the interpolated PMF graph is symmetric for our calculation. In physiological biological systems, cell membranes consist of different lipid components in the inner and outer leaflets of the bilayer. While the asymmetric lipid bilayer is dominant for a variety of cell types, the roles of bilayer asymmetry in determining various membrane properties still need to be investigated with

respect to permeability.

CHAPTER 4

ON THE VALIDITY OF HYDROGEN MASS REPARTITIONING (HMR) FOR CHARMM36 MEMBRANE SYSTEMS IN NAMD

Reproduced in part with permission from On the validity of Hydrogen Mass Repartitioning (HMR) for CHARMM36 membrane systems in NAMD. Curtis Balusek, Hyea Hwang, Chun Hon Lau, Karl Lundquist, Anthony Hazel, Anna Pavlova, Diane Lynch, Patricia Reggio, Yi Wang and James Gumbart. *Submitted to Journal of Chemical Theory and Computation*.

4.1 Introduction

Biological membranes are an essential component of all living cells [129]. They serve as a barrier between the cell and the outside world, preventing entry of many potentially harmful compounds, as well as regulating cellular import and export through membrane proteins. Cell membranes are typically composed of a phospholipid bilayer with embedded and/or associated proteins[129]. Phospholipids are amphiphilic molecules that are characterized by a hydrophilic head group containing a phosphate, which is glycerol-linked to one or more hydrophobic fatty-acid tails (Fig. 4.1A) /citeLombard2014.

Membrane models are frequently used in molecular dynamics (MD) studies because of their biological relevance. As such, MD simulations can be used to study membrane properties and provide an atomistic description of membrane structure and dynamics[130, 131, 132, 39, 133, 134, 135]. For example, membrane-embedded proteins often require the incorporation of a membrane in the model for protein stability[136, 137, 138]. Additionally, membrane permeability and small molecule interactions are often of interest in drug design, which can be investigated computationally using membrane models /citeWang2014,Lee2016.

In order to make predictions from MD simulation, accurate lipid force fields are necessary when studying membrane systems[139, 140]. To date, multiple force field models are available: AMBER14 [141], SLIPIDS [142], CHARMM36 [38], and multiple GROMACS united atoms mod-

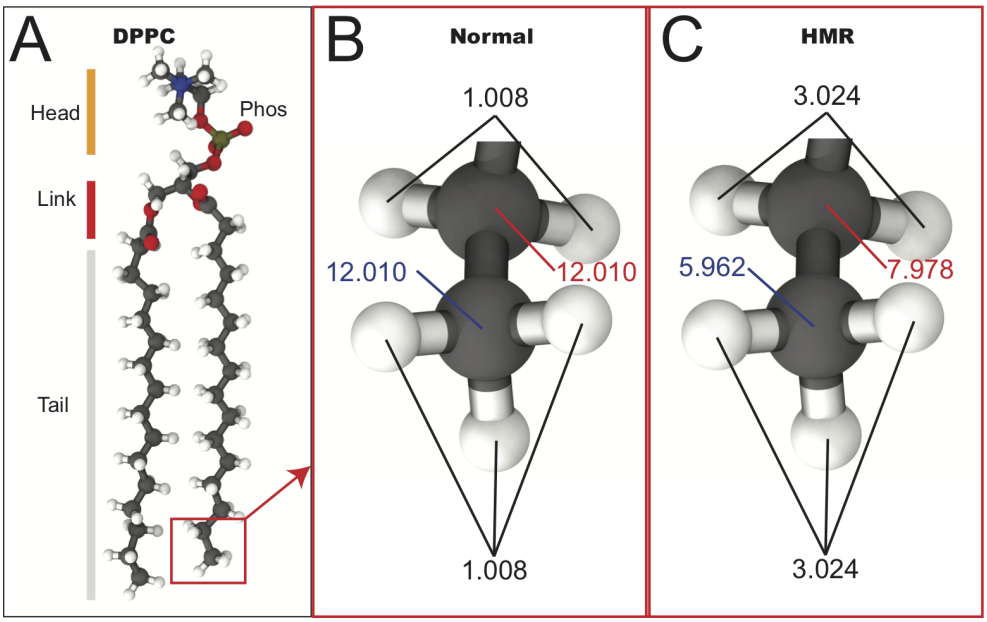

Figure 4.1: (A) Structure of DPPC lipid, phos and link denote phosphate and ester link, respectively. (B) Normal mass distribution for the atoms in the acyl-chain tail. (C) Mass distribution for the same atoms with HMR.

els[143, 144, 145]; several studies have compared present lipid models and improved upon existing ones[146, 130, 145, 139, 140]. Force-field parameters are typically evaluated based on their ability to reproduce experimentally known structural and dynamical properties of pure-lipid bilayers, e. g., lipid area, bilayer thickness, compressibility modulus, deuterium order-parameters, and diffusion coefficients[130, 140, 135, 139]. In some cases partition coefficients have been calculated to validate lipid:small-molecule interactions[134]. Furthermore, compatibility with water and protein force fields should also be considered when choosing a lipid force field[147, 127].

The CHARMM36 (C36) lipid force field is frequently used in MD simulations because it can accurately reproduce a number of physical properties of lipids, as well as its compatibility with the C36 protein and general small-molecule force field[38, 130, 140, 134, 135, 147, 127]. The most recent C36 lipid force field update resulted in improved agreement with experimental order parameters, compressibility modulus, and area per lipid[38]. Furthermore, the recently launched CHARMM-GUI web interface, which supports several MD software packages, has greatly facilitated the construction of membrane systems for MD simulations, specifically utilizing the C36 force field[148, 149, 46, 150]. CHARMM-GUI automatically generates structure, coordinate, parameter

and input for pure membrane and membrane-protein systems, supporting numerous phospholipid molecules through lightweight object oriented structure–analysis (LOOS)[151, 152].

In order to study properties of a membrane system, multiple simulations of sufficiently long time scales are typically required[153, 146]. As such, there is significant benefit to running longer MD simulations without the prohibitive computational cost, particularly for membrane-containing systems, which can be much larger than protein-only systems. One previously suggested approach to speed up MD simulations is by using a longer time step[154, 155]. Implementing a longer time step decreases the accuracy when integrating the equations of motion in MD; however, it has been shown that the introduced errors are typically much smaller than the statistical errors due to limited sampling /citeRao2012 Additionally, the increased energy drift introduced by a longer time step can be dampened by using a thermostat[156, 155]. Currently, the magnitude of the time step in atomistic MD is limited by the fastest moving atoms in the simulation, which are the vibrational motions of the hydrogen atoms[154]. Therefore, increases in time step can be achieved by slowing down or restricting the movement of the hydrogens[154]. Common practice in MD simulation has been an increased time step from 1 to 2 fs by keeping the covalent bonds involving hydrogen atoms rigid using SETTLE and SHAKE algorithms for water and other molecules, respectively[157, 158]. The implementation of these algorithms doubles the available simulation time at fixed computational cost; however, the SHAKE algorithm is likely to fail at time steps beyond 2 fs for conventional MD[157, 155].

Recently, MD simulation studies have shown that time steps of up to 4 or 5 fs can be acheived by altering hydrogen masses[154, 155, 159]. It is important to note that when implementing mass modifications, it is requisite that the total mass of the system does not change[154, 155]. As described by Feenstra et al., increasing the the total mass of the system will result in a slower time scale for various events of interest, e. g., diffusion[154]. Similarly, in the virtual site technique (VST), the hydrogens' masses are assigned to the adjacent heavy atoms and their positions are calculated and updated based upon the positions of the heavy atoms[160, 159]. However, implementing VST requires re-optimization of force field parameters, such that when applied to the C36 force field, VST was shown to alter several lipid properties, leading to thinner and more disordered bilayers [159]. Recently, it was shown that the combination of VST with HMR on every fourth methyl group in

the lipid tails resulted in strong agreement with measured lipid properties in standard MD simulations[161].

To clarify, HMR modifies the atomic input by repartitioning mass from each heavy atom to its covalently bonded hydrogens, while conserving the overall molecular mass[154, 155]. For example, when applying HMR, the reweighted hydrogen mass should not be greater than 3 amu because a larger mass transfer would make methyl carbons lighter than their bonded hydrogens. Hopkins et al. illustrated this method for both a small peptide as well as a large protein in explicit solvent [155]. They found that the protein/peptide with HMR applied, using a hydrogen mass of 3 amu and a time step of 4 fs, consistently reproduced conformations observed without HMR. However, when HMR was applied to both protein and water molecules, there was an increase in the viscosity of water and, consequently, slower transition rates between different protein conformations. Therefore, HMR should not be applied to water. Since its inception, HMR has been used in several software packages such as NAMD[52], AMBER[162] and ACEMD [163], in order to speed up MD simulation output.

It has also been shown that additional speed up can be obtained by decreasing the cutoff for non-bonded interactions. Although C36 lipids were parameterized and validated using a 12-Å cutoff with a switching function applied at 10 Å [38], most HMR studies employing lipids to date have used the C36 lipid force field with a 9 Å (default setting) cutoff in ACEMD or AMBER[164, 165, 166]. Previous MD simulations have shown that membrane properties are highly sensitive to the cutoff value and Lennard-Jones (LJ) switching functions because lipids dynamics are primarily drive by LJ interactions[38, 150]. Additionally, lipids are more hydrogen rich than proteins, for which HMR was previously validated[155]. However, to date, the effects of HMR and a shorter 9-Å cutoff with the C36 lipid force field have not been investigated.

In this paper we aim to test the application of HMR with a 4-fs time step for membrane systems by comparing lipid properties and lipid-protein interactions. Additionally, the effects of 9-Å cutoff are examined. Several single-lipid, mixed-lipid, and protein-embedded membrane systems were studied. It is found that applying HMR with a 12-Å cutoff provides consistent results in comparison to conventional 2-fs time step and 12-Å cutoff MD across all studied systems. However, employing a 9-Å cutoff altered several structural and kinetic properties for lipid bilayers, even though no significant difference was observed in protein-lipid and protein-protein interactions.

4.2 Methods

4.2.1 Construction and analysis of pure membrane systems

All-atom lipid bilayers were generated for pure membranes systems using CHARMM-GUI [46]. Three pure-membrane models (DPPC, POPE, and DOPC) were generated, as well as a fourth, multiple-lipid "Top6" model [45]. Each system contained 480 lipids (240/leaflet) and was solvated and ionized to a concentration of 150 mM NaCl. Although smaller (60 lipids/leaflet) membranes were initially tried, it was found that many of the properties measured did not converge well in 100-ns simulations (data not shown). Further details about each system and constitutive components can be found in Table S1).

Upon completion of the simulations, trajectories were analyzed to measure structural and kinetic properties such as areas per lipid (APL), membrane thickness, deuterium order parameters, mass density profiles, compressibility moduli (K_{A}), diffusion coefficient, dihedral trans-gauche transition rates.

In the present work, the $\langle$APL$\rangle$ was computed from the area of the simulation box in the x-y plane divided by the number of lipids in each leaflet whici is 240. Since we employed pressure coupling, the simulation box was allowed to fluctuate during the simulation; APL was used to monitor simulation equilibrium. Membrane thickness is reported as the head-to-head average distance as measured in the lipid electron density profiles [167, 168, 169]. The K_{A} is a measure of the stiffness of the membrane and it was calculated as,

$$K_{\mathrm{A}} = k_{\mathrm{B}}T\left(\frac{A}{\sigma_A^2}\right) \tag{4.1}$$

where k_{B} is Boltzmann's constant, T is the temperature, A is the area, and ${\sigma_A}^2$ is the variance of the area during the simulation.

Diffusion values are measured from the the mean-squared displacement of lipid center of mass motion in the x-y plane according to

$$< \Delta r(\tau)^2 >= \sum_{i=1}^{n} \left\langle \|\vec{r}_i(t+\tau) - \vec{r}_i(t)\|^2 \right\rangle = 2nD\Delta t. \tag{4.2}$$

The sum occurs over all molecule mass centers and averaged for all time separations τ. Due to an equilibration phase, the first 0-1 ns of time lag is discarded. The diffusion coefficient then is proportional to the slope of the linear regime of mean-squared displacement versus time-separation. All diffusion values are measured over the last 50 ns of simulation up to $\tau = 20$ ns.

Deuterium order-parameters (S_{CD}) are used to compare lipid simulations to experimental results of membrane-systems for each acyl carbon in the aliphatic tail, which are given by

$$S_{\mathrm{CD}} =< \frac{1}{2}(3\cos^2\theta - 1) > \tag{4.3}$$

where θ is the angle measured between the carbon-hydrogen bond vector and the membrane normal. The pure membrane simulations run here are small enough to not observe large membrane undulations, such that the normal vector to the bilayer can be assumed to be parallel to the z-axis.

4.2.2 Construction and analysis of a GPCR system

The model of a GPCR was taken from the study Hurst2010, in which CB2 was simulated in a POPC bilayer. The receptor was extracted and rebuilt in a slightly larger simulation cell with 83/75 phospholipids in the upper/lower leaflets as well as 53 2-arachidonoyl glycerol (2-AG) molecules, an endongenous ligand for CB2. Three separate 10 ns trajectories utilizing each of the three schemas were run. Data was saved at a 10-ps time interval. Additional 1-ns simulations with trajectory data saved every 100 fs were also run to provide a more accurate measure of the hydrogen-bonding autocorrelation functions.

The hydrogen bonding analysis and auto-correlation functions for the GPCR CB2 were computed with the LOOS ver 2.3.2 toolset [151]. For each frame, a hydrogen bond is defined as present (1) or absent (0) using a given geometric criterion between pairs of donors and acceptors. The auto-correlation function is subsequently computed using half of the trajectory and averaged over all pairs. Distance/angle cutoffs of 2.5 Å between the polar hydrogen and acceptor with a maximum deviation from linearity of 35 degrees was employed. Standard error was computed from the three separate trajectories. In addition, an alternate approach to computing hydrogen bond dynamics is through a procedure introduced by Rapaort1983. Here the hydrogen bond between an

acceptor/donor pair, h_{ij}, is again defined as 1 or 0 based on the above geometric criterion. The intermittent hydrogen bond autocorrelation function is given by:

$$C_I(t) = \left\langle \frac{\sum h_{ij}(t_o) h_{ij}(t_o + t)}{\sum h_{ij}(t_o)^2} \right\rangle \tag{4.4}$$

The sum in the above equation is over all paris of hydrogen bonds that exist at time t_o. Intermittent refers to a definition where a givien hydrogen bond pair is allowed to break and subsequently reform. Finally an averaging over multiple start times is performed. This approach produces an autocorrelation function that represents the hydrogen bond population. In this work the hydrogen bond autocorrelation module of MDAnalysis [170] was used to compute the above correlation function.

4.2.3 Construction and analysis of L8 peptide system

An ac-L_8-nme (L8) peptide was constructed and embedded into the water phase of a box containing a pre-formed POPC lipid bilayer with a upper leaflet of 53 lipids and a lower leaflet of 52 lipids. The initial conformation was an ideal α-helix, placed 10 Å from the bilayer surface. Dihedral restraints were applied to the peptide backbone to maintain the helicity due to the high temperature used (423 K), which has been validated previously for the same system [171]. The 200 kcal/mol·deg.^{2} dihedral force constant used previously in a non-HMR system produced instabilities in the HMR system due to the smaller masses of the heavy backbone atoms, which are reduced by $\sim$15%. Therefore, in order to maintain roughly the same mass-to-force-constant ratio, we similarly reduced the dihedral force constant to 175 kcal/mol in the HMR system.

The insertion propensity, p_{TM}, of the L8 peptide was calculated as the probability of the peptide being in the TM state. To distinguish the TM state from the S state, a criterion of $z < 8$ Å was found to be optimal. The free energy of S$\rightarrow$TM partitioning was then calculated as

$$\Delta G_{\mathrm{S}\rightarrow\mathrm{TM}} = +k_{\mathrm{B}}T \log(1/p_{\mathrm{TM}} - 1). \tag{4.5}$$

4.2.4 Construction and analysis of membrane mixing systems

System construction and Anton simulation details of the mixed POPC:cholesterol membrane were described in Hong et al. [172]. The POPC bilayer with 680 lipids were constructed by duplicating four times an equilibrated bilayer with 170 POPC [172]. All simulation conditions of this large POPC bilayer as well as HMR simulations using a 4-fs timestep and 12-Å or 9-Å cutoff of the mixed POPC:cholesterol membrane were identical to those of the pure lipid bilayers described above.

Radial pair distribution function and clustering analysis of the mixed POPC:cholesterol membrane were performed following Hong et al. [172] Undulation analysis was performed using the MDAnalysis package [170]. Error analysis was performed following the procedure of Grossfield et al. [173]. Briefly, a simulation trajectory was divided into M blocks, each of length τ_b. The average of $u^2(q)$ from each block was determined and then used to compute a standard deviation σ_{τ_b}, based on which we obtained the the blocked standard error (BSE):

$$BSE = \frac{\sigma_{\tau_b}}{\sqrt{M}}. \tag{4.6}$$

The error in k_c was then determined by assuming a 'worst-case-scenario combination' of errors from the four wavenumbers analyzed here: we subtracted the BSE from $\langle u^2(q)\rangle$ for the lowest wavenumber and added the corresponding the BSEs to $\langle u^2(q)\rangle$ for the remaining three wavenumbers, followed by re-fitting of a first-order polynomial, which produced the upper-bound error in k_c. Conversely, a lower-bound error was obtained. We note that the obtained errors were asymmetric, as illustrated in Fig. D.9.

4.2.5 Construction and analysis of OmpF systems

OmpF porin is a nonspecific pore protein from the outer membrane of *Escherichia coli*. An OmpF membrane-protein system was created using the crystal structure reported by Yamashita et al. [174](PDB: 2ZFG) and embedded in a POPE phospholipid bilayer to replicate the systems used in Pezeshki, Chimerel, Bessonov, Winterhalter, and Kleinekathofer. The system contained 99,157 atoms with 176 POPE lipids, 19,421 water molecules, and 420 potassium (K^+) and 396 cloride (Cl^-) ions, giving 1.12 M KCl solution. Three replica simulations of 10 ns each were carried out at 0 V, $\pm$0.2 V,

$\pm$0.5 V, and $\pm$1 V mirroring a previous OmpF conductance study [175]. We report the average and standard deviation of the current at each applied voltage by summing up the movement of the charges in the z direction [175, 176, 177].

4.2.6 MD simulations

After construction, HMR was applied to each unique system using a VMD [60] script provided in the supplement (hmr.tcl), which created two copies, standard and modified, with the difference being the repartitioned mass in the latter. For the standard copy, MD was performed with a 2-fs time step, a 12-Å cutoff (2-12), and a force-based switching function starting at 10 Å. The modified copy was simulated using a 4-fs time step and either a 12-Å cutoff with switching starting at 10 Å (4-12) or a 9-Å cutoff with no switching (4-9). In all simulations, long-range electrostatic interactions were evaluated every 4 fs using the particle-mesh Ewald method [59]. Unless otherwise stated, constant temperature was enforced using Langevin dynamics and constant pressure was enforced using a Langevin piston [57]. All simulations used NAMD2.12 [52] and the CHARMM36 force field for proteins [127] and lipids [38]. Configuration files representative of each simulation schema can be found in the supplement. System visualization and analysis was performed with Visual Molecular Dynamics (VMD).

4.3 Results

To determine the effects of HMR, time step, and cutoff on structural and dynamical properties, we performed all-atom MD simulations employing three different simulation schema. As a reference, we first simulated each system studied using a 2-fs time step and 12-Å cutoff with force-based switching from 10-12 Å (referred to as 2-12 throughout the text). The other two schema implement HMR along with a 4-fs time step and either a conventional 12-Å cutoff (referred to as 4-12) or a truncated 9-Å cutoff with no switching (referred to as 4-9). Results of lipid membrane simulations are compared with observations from X-ray or neutron scattering, or NMR experiments by considering temporal and spatial averages of various observables, e.g., bilayer thickness (D_{HH}) or APL [35, 178].

4.3.1 DPPC membrane

Dipalmitoylphosphatidylcholine (DPPC) is a common lipid that has been widely utilized in both experiments and simulation, and thus it has ample data for comparison [179, 180, 38, 181]. Therefore, we used it here as a first test case for determining the possible role of HMR and cutoff on structural and dynamical properties of a pure DPPC membrane. We examined multiple static and kinetic properties of this membrane based on 100-ns simulations, including electron density, area per lipid (APL), area expansion modulus (K_{A}), order parameters (S_{CD}), diffusion constant (D), and dihedral trans-gauche transition rates.

First, static properties of the pure DPPC membrane were measured to compare with previous experimental and MD results, beginning with the APL avalues in each system. The APL for DPPC at 323 K in the 2-12, 2-12-HMR, and 4-12 simulations is around 60-61 Å^2 (Table 4.1 and Fig. 4.2A). Experimental values are slightly larger at 63.3-64.3 Å^2 [179, 180]. In the 4-9 simulation, the APL increases substantially, to 65.5 Å^2. This increase is due to a reduction in the dispersion interactions, which are dominant in the aliphatic tails region (Fig. SD.1), also reflected in the decreased order (Fig. 4.2C) and thinning of the electron density profile (Fig. 4.2B). Similar to APL, K_{A} was measured for each of the systems to, based on Eq. 4.1 using the membrane area fluctuations. K_{A} values from each of the DPPC systems (Table 4.1) are in reasonable agreement with the experimentally observed value (231 mN/m [35]), with no observable pattern between the different simulation schema.

Next, we looked at order parameters (Fig. 4.2C), finding that the values from our 2-12 simulation agree well with previous experimental [179] and simulation [182, 183, 184, 38] results. When comparing the 4-12 simulation to the 2-12 simulation, there is a small decrease in lipid order resulting in a $5.7 \pm 2.8\%$ difference on average over all the carbon positions; when comparing 2-12 and 4-9 simulations, the decrease is much larger ($17.4 \pm 6.4\%$), suggesting that the cutoff has a significant effect on lipid order. To discriminate between HMR and the 4-fs time step, we performed an additional simulation with 2-fs time step and 12-Å cutoff as well as HMR (2-12-HMR), which showed a decrease of $1.0 \pm 0.8\%$ on average in the order parameters (Fig. 4.2C), similar to the 2-12 simulation. This result suggests that HMR causes little to no effect on the lipid order parame-

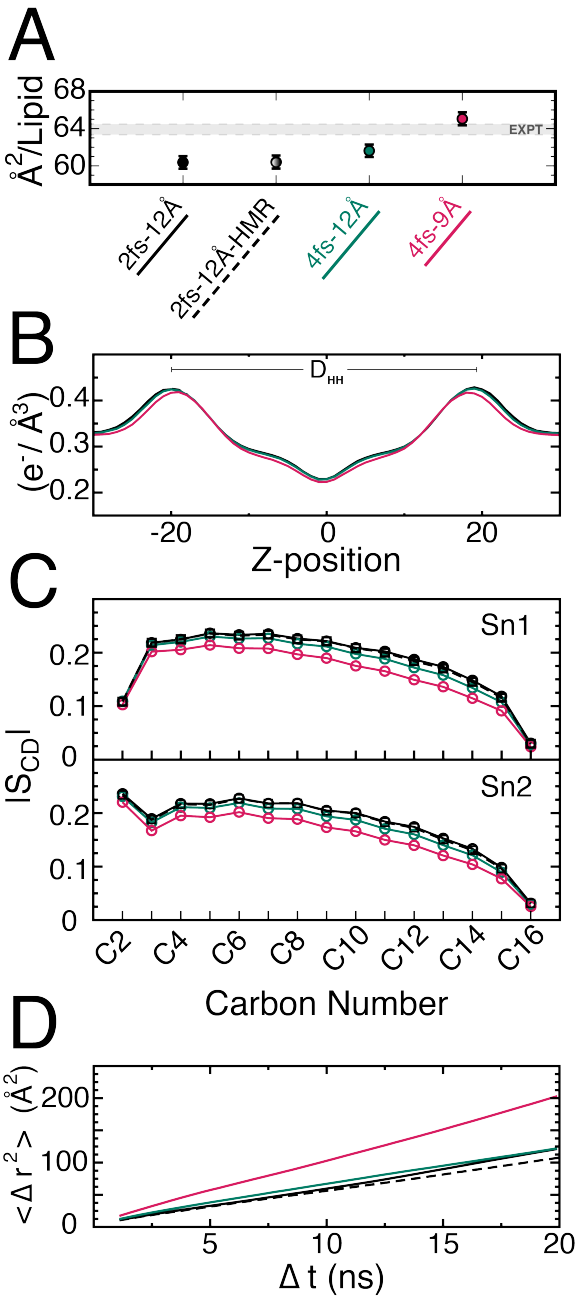

Figure 4.2: DPPC membrane properties. For each panel, 2-12 is colored in black, 4-12 in green, and 4-9 in red. An additional 2-12 with HMR is shown as a dashed black line. (A) Area per lipid with standard deviation bars taken from last 50 ns of production. (B) Plot of electron density; membrane thickness (D_{HH}) is measured from left peak to right peak of each distribution. (C) Plot of sn1 (top) and sn2 (bottom) lipid order parameters (circles) for the 2-12 (black), 4-12 (green), and 4-9 (red) simulations. The 2-12-HMR values are shown as black squares. (D) Mean-squared displacement vs. time averaged over all lipids and times for each simulation.

ters, a 4-fs time step causes a slight but measurable decrease in order, and a reduced cutoff causes a substantial decrease in order. The decrease in order is also evident from an increased interdigitation of the aliphatic tails in the 4-9 simulation (Fig. SD.1, bottom) compared to 2-12 (Fig. SD.1, top) and 4-12 (Fig. SD.1, middle) simulations. Furthermore, aliphatic interdigitation between membrane leaflets results in membrane thinning by 1 Å in the 4-9 simulation compared to the 2-12 simulation (Fig. 4.2B).

We also examined kinetic properties for each simulation, such as the rate of lipid diffusion, dihedral transition rates for the aliphatic tails, and spin relaxation times. While diffusion values from simulation are not reliable for a number of reasons, including a dependency on box size [185] and thermostat [186], they provide a useful comparison between simulation schema. Diffusion coefficient (D) are calculated from the slope of the mean-square displacement vs. time, averaged over lipids and time (Fig. 4.2D). For simulations with a 12-Å cutoff (2-12, 2-12-HMR, 4-12), diffusion values ranged from 1.30-1.64 Å^2/ns, slightly smaller than the experimental value of 1.78 Å^2/ns [187, 188]. For the 4-9 simulation, D was much larger at 2.53 Å^2/ns. However, it has been demonstrated that Langevin dynamics, used in all simulations here to control the temperature, reduces D by 35% [186]. Therefore, we also ran the 2-12 simulation using the Lowe-Andersen thermostat instead, yet found that D was significantly larger at 2.47 Å^2/ns (Fig. S D.2). The increase in D was even greater for 4-12 at 2.47 Å^2/ns and 4-9 at 6.56 Å^2/ns.

4.3.2 Other membranes

System	Setting	APL (Å^2)	D_{HH} (Å)	K_{A} (mN/m)	D (Å^2/ns)
DPPC (323 K)	2fs-12Å	60.37 $\pm$0.67	39.05	249.2	1.45
	2fs-12Å HMR	60.41 $\pm$0.70	38.96	227.7	1.27
	4fs-12Å	61.62 $\pm$0.67	38.73	252.5	1.43
	4fs-9Å	65.1 $\pm$0.69	38.04	250.9	2.42
	Exp.	63.1 – 64.2[179, 180, 189]	37.8-38.0[180, 189]	231[35] (318K)	1.78[187]
POPE (310 K)	2fs-12Å	57.36 $\pm$0.59	40.4	281.9	0.64
	4fs-12Å	57.96 $\pm$0.67	40.3	222.4	0.97
	4fs-9Å	61.07 $\pm$0.61	39.5	279.7	1.18
	Exp.	59.8 – 60.8[190]	40.0[190] (303K)	233[191]	–
DOPC (295 K)	2fs-12Å	66.95 $\pm$0.57	38.7	350.3	0.65
	4fs-12Å	66.97 $\pm$0.62	38.7	288.6	0.61
	4fs-9Å	70.31 $\pm$0.71	38.0	241.4	1.13
	Exp.	67.4[189] (303K)	36.7[192] (303K)	265[34] (303K)	1.0[193] (296.5K)
Top6 (310 K)	2fs-12Å	61.54 $\pm$0.57	37.2	327.4	0.78
	4fs-12Å	62.46 $\pm$0.63	37.0	269.0	0.87
	4fs-9Å	64.75 $\pm$0.62	36.9	290.0	1.41
	Exp.	63.0 $\pm$0.19[194]	–	240[194] (310K)	–

Table 4.1: Average properties of lipid bilayer; Area per lipid (APL), membrane thickness (D_{HH}), area compressibility modulus (K_{A}), and diffusion coefficient (D). The values of temperature in the parentheses indicate that the property was measured at that specific temperature.

After measuring the effects of HMR, longer time-step, and a shorter cutoff on an unsaturated membrane which is DPPC, we proceeded to simulate three additional membranes to determine if varying lipid composition would alter our initial observations. We performed simulations on 1-palmitoyl,2-oleoyl-sn-glycero-phosphatidylcholine (POPC, one unsaturated tail), 1,2-oleoyl-snglycero-phosphotidylcholine (DOPC, two unsaturated tails), as well as the so-called Top6 membrane, which is a mixture of saturated, unsaturated, and cyclic-containing lipids. In order to expand upon the same measurements as the DPPC simulations, each of these membranes were simulated using the 2-12 schema as a control, as well as the additional 4-12 and 4-9 schemas applying HMR. We report the various physical properties of the membranes in Table 4.1, together with experimental values from the literatures. These properties from the simulations were calculated over the last 50 ns of each 100-ns simulation.

The APL is a sensitive and easily calculated measure for the ordering of the lipids and may be used to validate the quality of simulations. We calculated APL as a projected area from the size of the periodic simulation box for each systems. Table 4.1 shows that the values of APL in all the system settings are in a good agreement with experimental measurements, resulting in a 0.6 to 4.3 % difference (See Fig.SD.3 for graphs of APL fluctuation over the entire simulation period). It was also observed that the 4-9 system has the larger APL values in each of the systems than 2-12 and 4-12, demonstrating that APL increases with a shorter cutoff (9 Å vs. 12 Å) for all the systems. The higher values from the simulation using 4-9 were expected due to the reduction in long-range electrostatics between atom pares with 9 Å cutoff.

One particular result of interest is the difference in diffusion values observed in each of the pure membrane systems. There is a small increase going from 2 fs to 4 fs; however, each 4-9 system has a diffusion value approximately 40% greater than in either the 2-12 or 4-12. This is due to the increased fluidity of the membrane as is also seen in the lipid order parameters (See diffusion plots for each systems in SI). The values of K_{A} using Eq. 4.1 for each system are shown in Table 4.1. However, unlike other properties, the values of K_{A} showed no consistency between simulation schema. It is known that K_{A} values from MD simulation can be sensitive to the time frame used for measurement; because K_{A} is calculated based on the area fluctuation, the discrepancy with experimental values were expected.

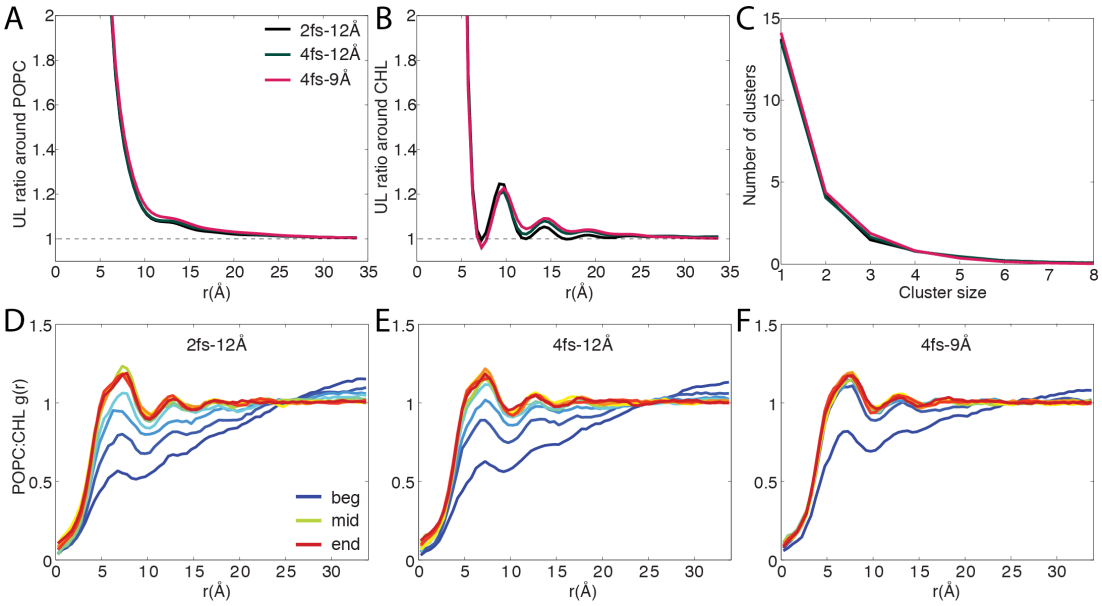

Figure 4.3: Impact of HMR, time step and cutoff on lipid mixing. (A-B) Average ratio of unlike neighbors to like neighbors (UL) around a given lipid species. The expected values based on mixing ratio are indicated by dashed lines. (C) Clustering analysis results of the POPC:CHL mixture. (D-F) Time evolution of the radial pair distribution functions $g(r)$ for POPC:CHL. $g(r)$ is averaged in 100-ns blocks and colored by simulation time, with blue, green and red indicating the beginning, the middle and the end of a simulation, respectively.

4.3.3 Lipid mixing and membrane bending modulus

To examine the impact of time step, HMR and cutoff on lipid mixing, we turn to the POPC:cholesterol mixture previously investigated by microsecond Anton simulations[172]. Each leaflet of the mixture was composed of 70 POPC and 35 cholesterol, with the latter initially placed at the center of the bilayer. This mixed membrane was simulated for 1 μs with either the 4-9 or the 4-12 schema (the Anton simulation reported previously [172] provides the reference for 2-12). Unless otherwise noted, we analyzed the trajectory from the first microsecond of the 2-μs Anton simulation for a fair comparison with the 1-μs runs performed in this work.

As shown in Fig. 4.3, regardless of the schema used, the final structures of the mixtures are similar to each other, as reflected by the ratios of unlike-to-like (UL) neighbors (Fig. 4.3A,B) and the size distribution of cholesterol clusters (Fig. 4.3C). Therefore, the equilibrium distribution of the lipids is unaffected by the choice of time step, use of HMR, or cutoff. The APL of the mixtures, however, is clearly affected: averaging over all POPC and cholesterol yields an APL of 46.4 Å^2,

47.1 Å^2 and 49.4 Å^2 for the 2-12, 4-12, and 4-9 simulations, respectively, reflecting a trend consistent to that observed in our pure lipid simulations (Table 4.1). Comparison of the three simulations also reveals a clear difference in the speed of mixing. Semi-quantitatively, this can be seen from Fig. 4.3D-F and Fig. D.8, which show the evolution of the radial pair distribution function $g(r)$ over the course of the 4-9 and the 4-12 simulations as well as the first 1 μs of the previously performed 2-12 simulation. The $g(r)$ curves, drawn every 100 ns, suggest that the 4-9 run converges much faster than the other two simulations. Quantitatively, the lateral diffusion coefficient of cholesterol in the 4-9 simulation (6.5×10^{-8} cm^2/s) is over 2$\times$ larger than that in the 2-12 simulation (2.5×10^{-8} cm^2/s). Similarly, POPC diffuses significantly faster in the former system, with a diffusion coefficient of 6.1×10^{-8} cm^2/s (2.2×10^{-8} cm^2/s in the 2-12 run). In the 4-12 simulation, diffusion of cholesterol (4.4×10^{-8} cm^2/s) and POPC (3.0×10^{-8} cm^2/s) is also accelerated compared with the 2-12 simulation, although to a much smaller degree than in the 4-9 simulation.

Apart from lipid lateral diffusion, it is worth noting that a cholesterol flip-flop event was recorded in both the 4-9 and the 4-12 simulation, in contrast to zero flip-flop events recorded throughout the 2-μs 2-12 simulation. The larger APL in the 4-12 and 4-9 simulations may have contributed to their increased cholesterol flip-flop events, as the APL is linked to the free energy barrier of defect formation in a membrane [195]. Overall, our data indicate that the choice of time step, cutoff and use of HMR has a negligible effect on the distribution of lipids in an equilibrated mixture, although other equilibrium properties, such as the APL, are evidently affected. On the speed of lipid mixing, while increasing the simulation time step from 2 fs to 4 fs and applying HMR has a rather moderate effect, decreasing the cutoff from 12 Å to 9 Å significantly accelerates mixing.

Following our investigation on lipid mixing, we went on to evaluate how HMR may affect one of the most important material moduli of a membrane, namely, its bending modulus (k_c). Using a bilayer with 680 POPC, we performed three 1-μs simulations with 2-12, 4-12, and 4-9 schema, respectively. The $\sim$150 Å$\times$150 Å bilayer supported relatively long-wavelength undulation modes, thereby, allowing us to determine k_c from $\langle u^2(q)\rangle$, the average square amplitude of undulation at a given wavenumber q. More specifically, k_c was calculated from the last 900 ns of the 1-μs trajectories according to $\langle u^2(q)\rangle = k_c k_B T A^{-1} q^{-4}$ using the MDAnalysis package [170] and methods presented in Refs. brandt2011interpretation,braun2011determination. As shown in Fig. D.9, k_c was

found to be 30.9 k_BT (12.9×10^{-20} J) in the 2-12 simulation, which is comparable to the experimental value (9.0×10^{-20} J) reported for a similar lipid bilayer (1-stearoyl-2-oleoyl-*sn*-glycero-3-phosphocholine) [196].

To estimate the uncertainty in k_c, we first examined the blocked standard error in $\langle u^2(q)\rangle$. The undulation mode with the smallest wavenumber (longest wavelength) was found to have the largest error, calculated from the last 900 ns (Fig. D.9). The error is approximately an order of magnitude greater if only the last 50 ns of trajectories are used in the analysis instead of the last 900 ns (data not shown). This behavior supports the need for microsecond-long trajectories in reliable analysis of k_c. Here, the uncertainty in our k_c values was found to be approximately 2 k_BT. Compared with the 2-12 run, k_c decreased slightly to 28.6 k_BT in the 4-12 simulation. In the 4-9 simulation, a further decrease was seen, with k_c reaching 25.4 k_BT. We note that the difference between the 2-12 and the 4-9-simulations is well beyond the estimated uncertainty in k_c, indicating that the comparison is statistically meaningful. The average projected APL was found to be 64.2, 64.9 and 67.3 Å^2 in the 2-12, 4-12, and 4-9 simulations, respectively. Taken together, these results again reflect the weakened lipid interactions when a short cutoff (9 Å) is adopted. Such weakened interactions not only produce an increased area per lipid, but also reduced the energetic cost of bending the membrane and, thereby, resulting in a decreased k_c.

4.3.4 Electric Field Simulations of OmpF

One of the most important functions of membrane proteins is the channeling of ions into and out of the cell. OmpF is a well-characterized trimeric protein that acts as a nonspecific ion channel in the outer membrane of Gram-negative bacteria [197, 198]. To continue the investigation into the effect of timestep, cutoff, and HMR on properties like conductance, we performed simulations with an applied electric field on the outer membrane ion channel OmpF. We note here again that HMR was never applied to water molecules. Scaling by molarity, our results across all simulation schema compare favorably to those reported by Pezeshki et al., [175] including the higher current for positive voltages due to a slight cation selectivity of the channel. At low voltages we observe a near exact agreement between all three simulation protocols (Fig. 4.4). At higher voltages, 4-9 underestimates the current, while 4-12 slightly overestimates the current with respect to the conventional

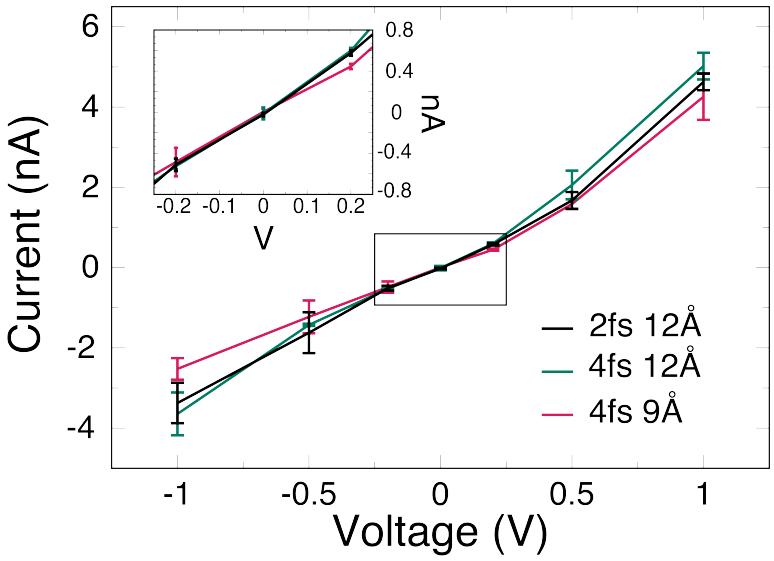

Figure 4.4: Current vs. voltage for OmpF membrane protein systems. 2-12 in black, 4-12 in green, and 4-9 in red. Inset graph shows the lower potentials and little distinguishable difference in measured current in each system.

2-12. However, the deviation for each of the HMR systems is within, or very nearly within the standard deviation of the conventional 2-12 system indicating that the effect of HMR, longer timestep, or shorter cutoffs on the membrane dynamics does not significantly affect the dynamics of OmpF and, therefore, the conductance.

4.3.5 Hydrogen bonding capacity in GPCRs

G-protein coupled receptors (GPCRs) are integral membrane proteins that share a common architecture of seven transmembrane helices connected by intracellular (IC) and extracellular (EC) loops. These membrane-bound proteins are central among the classes of proteins involved in signal transduction. Ligand binding to, and subsequent conformational changes of, GPCRs leads to activation of intracellular heterotrimeric G-proteins and ultimately cellular response. To a large part this functionality is achieved by the inherent flexibility of GPCRs[199]. As a result functional outcomes can and are modulated by their lipid environment. Therefore one should anticipate that the structure and function of these membrane bound systems would be coupled to the details of the treatment of the membrane environment. Given the importance of hydrogen bonding in maintaining the structure of GPCRs in a membrane environment, we have explored the effects of HMR, as well as the potential

energy truncation, on both the occurrence and lifetime of intra- and inter-molecular hydrogen bonding for the cannabinoid type-2 receptor (CB2). Using the CB2 model of Hurst et.al. [200] we have examined the hydrogen bonding capacity as a function of HMR, time step, and cutoff. We ran three 10-ns simulations for each of the 2-12, 4-12, and 4-9 schema. In Fig. D.10 the fraction of hydrogen bonds is plotted for each transmembrane helix in each schema. Overall, given the overlap of the error bars, the three simulation schemes produce essentially the same helical hydrogen bonding patterns.

In addition to the percent occurrence of the intra-molecular hydrogen bonds of CB2, we examined the intra- and inter-molecular hydrogen bonding autocorrelation functions. Given that water was not subjected to HMR and polar hydrogens are not present in POPC, hydrogen bonding between CB2 donors (polar hydrogens) and the available acceptors in the simulation, including CB2, water, and lipid acceptors, have been considered. Due to the short lifetime of a typical hydrogen bond, particularly with water, 1-ns trajectories, with conformations output in 100-fs intervals, were analyzed. These correlation functions are reported in Fig. 4.5. Hydrogen bonding between CB2 and itself as well as CB2 and water is unaffected by the HMR/cutoff schema used. However, there is a slight decrease in lifetime of hydrogen bonds between CB2 and lipids for 4-12 and 4-9 compared to 2-12, as evidenced by the lower correlation at long times. In addition to these individual hydrogen bond autocorrelation functions, MDAnalysis [170] was used to generate population autocorrelation functions Rapaort1983. Analogous to the previous results, there is very little difference the correlation functions between CB2 and either acceptors in CB2 or water, with a more noticeable depression in the curves for the hydrogen bonding to the lipid species. These are presented in Fig. 4.6.

4.3.6 Peptide partitioning in POPC

To further investigate how membrane-protein kinetics are affected by HMR, we performed long equilibrium simulations of an octoleucine (L8) helix embedded within a symmetric POPC bilayer (see Methods) using the 4-12 and 4-9 schema for comparison to a previous work on Anton [171]. With the peptide starting in a transmembrane (TM) state and using a high temperature (423 K), we measured the number of transitions between the TM and surface-associated (S) states over the course of a 1.3- and 1.5-μs production run for the 4-12 and 4-9 schema, respectively. The TM

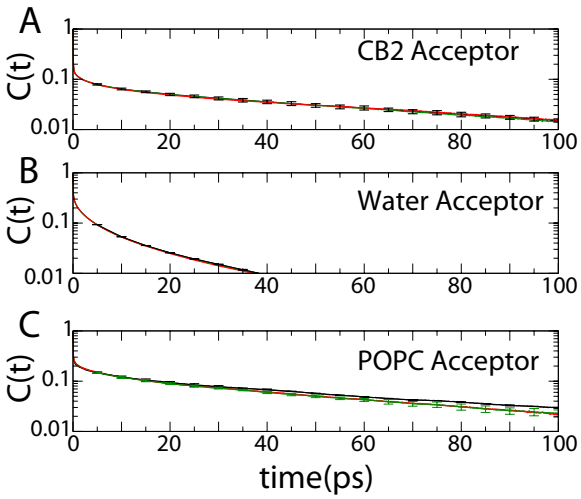

Figure 4.5: Hydrogen Bonding auto-correlation functions. 2-12 data is shown in black, 4-12 in green, and 4-9 in red. Values reported are averaged over three separate runs with the standard error reported.

state was defined as $|z| < 8$ Å, where z is the distance between the center of mass of the peptide backbone and the center of the membrane, consistent with previous studies of L8 insertion into a lipid bilayer [171]. The high temperature was necessary for sufficient sampling of the two states, and backbone dihedral restraints were added to ensure the peptide did not unfold at this temperature (see Methods) [171]. We observed 14 transitions in 1.3 μs (10.7 transitions/μs) in the 4-12 simulation, while we only observed 10 transitions in 1.5 μs (6.7 transitions/μs) in the 4-9 simulation (see Fig. 4.7A). In addition, the peptide spent far less time in the S state for the latter, with $\Delta G_{\mathrm{S}\rightarrow\mathrm{TM}} = -2.8$ kcal/mol for the 4-9 simulation compared to -0.9 kcal/mol for the 4-12 simulation (see Fig. 4.7B and Methods for calculation of $\Delta G_{\mathrm{S}\rightarrow\mathrm{TM}}$). Previous multi-$\mu$s-scale simulations of L8 at 423 K run on the Anton supercomputer with a 2.5-fs timestep and a 13–14-Å cutoff without HMR produced roughly 12 transitions/μs, with a temperature-independent $\Delta G_{\mathrm{S}\rightarrow\mathrm{TM}} = -0.9 \pm 0.2$ kcal/mol [171]. Results from the 4-12 simulation are in good agreement with these values, reproducing the free energy difference and only slightly underestimating the S→TM transition rate. The 4-9 simulation, however, significantly underestimates both the free energy difference and the transition rate.

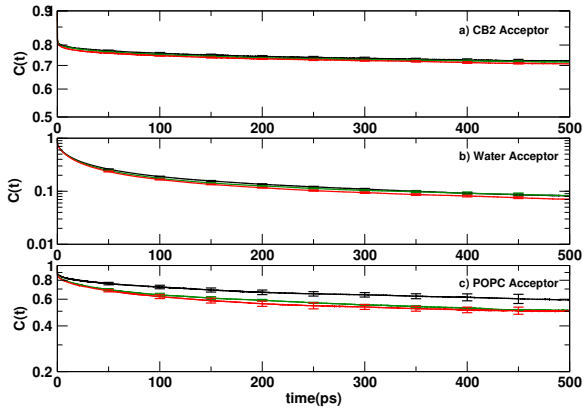

Figure 4.6: Population Hydrogen Bonding auto-correlation functions. 2-12 data is shown in black, 4-12 in green, and 4-9 in red. Values reported are averaged over three separate runs with the standard error reported.

4.3.7 Benchmarks

Benchmarking simulations were carried out for the DPPC membrane (113,064 atoms) and the large, 680-lipid POPC membrane (170,844 atoms). Each system was run on 1, 2, 4, 8, 12, 16, and, for the larger system, 24 CPU-only nodes of (1) Stampede2 at Texas Advanced Computing Center (Intel Xeon Skylake CPUs; 48 cores/node) and (2) Bridges at Pittsburgh Supercomputing Center (Intel Haswell CPUs; 28 cores/node). Each simulation system was run using (1) the 2-12 schema, (2) the 4-12 schema, (3) the 4-12 schema and PME evaluated every 8 fs, (4) the 4-9 schema, and (5) the 4-9 schema and PME evaluated every 8 fs.

As expected, the 4-9/8-fs-PME simulations had the greatest performance (measured in ns/day) at practically all node counts (Fig. Sxx). However, the benefits accruing from each approximation were not equal. The 4-12 simulations are consistently $\sim$75% faster than the 2-12 simulations on CPUs (Fig. Sxx). However, employeeing a 9-Å cutoff only speeds up simulations by an additional 20-45%. Evaluating PME electrostatics every 8 fs instead of 4 fs is of mixed benefit at either cutoff, giving at most 40% improvement in speed at high node counts; at reasonable (efficiency $>$ 75%; Fig. Sxx) node counts, the speedup is 20% at most.

Although no production simulations in this paper used GPUs, we also benchmarked on 1-4 NVIDIA GTX 980 cards on a single node with two Intel Xeon Haswell CPUs (24 cores, using 6 cores/GPU). Going from 2-fs to 4-fs time steps gives a consistent speedup of 40%. No improvement

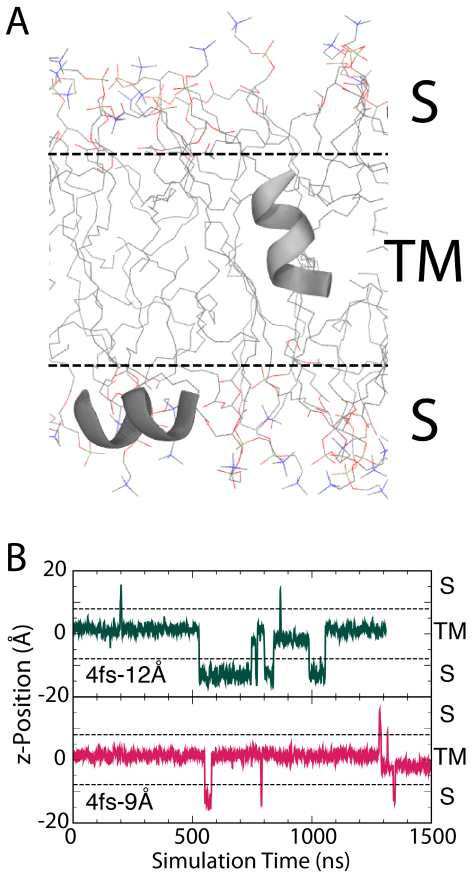

Figure 4.7: Transmembrane to surface-associated transitions of L8 helix in a POPC bilayer with HMR. (A) Position and orientations of L8 in surface-associated (S) and transmembrane (TM) states. The peptide is shown in cartoon representation and colored grey. Lipid molecules are shown in line representation and colored by atom name (hydrogen atoms omitted). (B) Position of helix within the membrane for the (top) 4-12 simulation and (bottom) 4-9 simulation. Center of the membrane is defined as $z = 0$ Å and TM states are defined as $|z| < 8$ Å.

was seen when shortening the cutoff; short-range interactions are evaluated on the GPU(s), but these simulations are CPU-limited. Additionally, no benefit was seen when evaluating PME every 8 fs instead of 4 fs (Fig. SxxE,F).

4.4 Discussion

MD simulations of membranes and membrane proteins have become increasingly common over the last two decades, and the need for longer trajectories has grown concomitantly. Thus, methods to improve the efficiency of these simulations are highly desirable. One approach, although also at least two decades old [154], has gained prominence recently: hydrogen-mass repartitioning (HMR). HMR accelerates the simulation by redistributing the mass from a parent atom onto its bonded hydrogens, thus slowing their motions and permitting a larger time step, typically 4 fs instead of 1-2 fs [155]. We applied HMR to a variety of membrane-only and membrane-protein systems using NAMD [52] along with the CHARMM36 [38, 127] force field. Our results show little difference between the standard masses with a 2-fs time step and the repartitioned masses with a 4-fs time step.

We also investigated another common approach used to speed up simulations, namely reducing the Lennard-Jones potential cutoff. Although CHARMM36 is parameterized for membranes based on a 12-Å cutoff with a force-based switching function starting at 10 Å, a number of studies have pushed this to 9 Å with no switching function [164, 165, 166]. However, our results here show that there are trade-offs involved with this approximation, such as an increased APL, disorder, and rate of diffusion (Fig. 4.2). While these altered properties do not necessarily invalidate a simulation's results, their effects should be carefully considered before using a shorter cutoff. Looking ahead, approaches such as Lennard-Jones PME (LJ-PME) [201, 202], which obviates the need for a cutoff, and the Drude polarizable force field [203] are likely to overcome the problems noted here [204].

Our benchmarks showed clear benefits of using HMR and a 4-fs time step in NAMD. Simulations are approximately 1.75× faster using a 4-fs time step, whereas reducing the cutoff from 12 Å to 9 Å made them only an additional 1.2-1.45× faster. Applying HMR incurs practically no overhead and a script for converting one's PSF file in VMD as well as sample NAMD configuration files are provided in the supplement.

CHAPTER 5

CONCLUSION

All living things are made from cells. Each of these cells, be they plant, animal, fungus, or bacteria, has a cell membrane. The cell membrane is the semipermeable covering that surrounds all cells indicating that it will allow certain substances to pass through it, while prohibiting the passage of others. It also is elastic, deforming as needed by the cell to respond to stresses and signals from inside and out. These two features, elasticity and selective permeability, make cellular membranes much more than a rigid wall and both were investigated in this thesis.

First, the Gram-negative cell envelope comprises three layers, an inner membrane, a cell wall, and an outer membrane. The cell wall of Gram-negative bacteria consists of a thin layer of peptidoglycan in the periplasmic space between the inner and outer lipid membranes. The outer membrane contains lipopolysaccharides on its outer leaflet and facilitates non-vesicle-mediated transport through channels such as porins or specialized transporters. We investigated the mechanical properties of individual components of the Gram-negative cell envelope to find out how turgor pressure is distributed between the cell wall and both membranes. We measured the area expansion modulus (K_{A}) values for both membranes and the cell wall using MD simulation, and compared those values with experiments. Our determined $K_{\mathrm{A}}^{\mathrm{CW}}$ values suggest that a turgor pressure of 1 atm is not feasible for the *E. coli* regardless of whether or not the IM participates in bearing it. At a more feasible turgor pressure of 0.3 atm, the cell wall can bear 0% – 65% of the pressure, depending on $K_{\mathrm{A}}^{\mathrm{OM}}$ and whether or not the IM contributes. Assuming that the true K_{A} of the OM is between our experimental and simulated values, it bears 35% – 78% of the 0.3-atm turgor pressure. When the cell wall is twice its relaxed area, $K_{\mathrm{A}}^{\mathrm{CW}}$ is identical to $K_{\mathrm{A}}^{\mathrm{OM}}$ (Fig. 2.7), in agreement with recent experiments [16]. We also demonstrated the inelastic behavior of the cell wall, i.e., that it strain stiffens, making the cell wall bearing an increasingly large fraction of the tension. Future work includes investigating how the mechanical response differs in other bacteria as well as when challenged by antibiotics, e.g., beta-lactams, that disrupt the peptidoglycan network.

Second, the study of passive absorption is of critical importance in the development of effective

drugs. Especially, estimation of passive permeation rates of drugs is key, primarily for the delivery of candidate drugs to their intracellular targets. Because lipid bilayers are an effective barrier to passive diffusion of drugs, bilayer composition and properties will play an important role in the prediction of permeability. Although there are many previous studies on predicting permeability experimentally and computationally, they are expensive and time consuming. We introduced a novel way to calculate the permeability, considering the membrane deformation energy as the dominant factor in crossing the membrane into cells. We chose 15 drugs and built both a complex mammalian membrane and a simple DMPC membrane to find out the effect of having cholesterol as well as a different lipid composition. The R^2 of our results using mammalian membrane compared to cell-based assays has the highest value, while the experimental PAMPA method has the lowest R^2 value. This indicates that our method can predict permeability more accurately than PAMPA experiments, at least for the compounds chosen, and it is less expensive than other computational methods. Also, since the DMPC membrane has an R^2 in between those two values, we found that the membrane composition is important to calculate permeability computationally. Future work in this area will include extending the method to other membranes and a wider range of drugs. In addition, the scripts developed across multiple tools will be packaged into an easy-to-use self-contained tool accessible from within the visualization and analysis program VMD.

Last, we analyzed two methods growing in popularity that can make molecular dynamics (MD) simulations faster. The conventional time step of atomistic MD simulations is determined at 2 fs by the fastest motions in the system. Hydrogen-mass repartitioning (HMR) is an approach to achieve a 4-fs time step with reasonable simulation stability. While this HMR method has been tested for soluble protein systems, it has not been extensively tested for membrane-containing systems. To test it, we increased the mass of the hydrogen atoms of membrane and protein to 3 amu and decrease the mass of the parent atom by an equivalent amount. We also investigated another common approach used to speed up simulations, namely reducing the Lennard-Jones potential cutoff. These HMR and short-cutoff methods were applied to a variety of membrane-only and membrane-protein systems. These two methods can make simulations 1.2 to 1.75$\times$ faster than conventional MD simulations. Our results show that while HMR has little effect on the dynamics of the system, there is a trade-off involved with a shorter cutoff, such as an increased APL, disorder, and rate of diffusion. Future

work can include testing the application of HMR to water molecules as well, which can change the viscosity and stress at water/membrane interfaces. HMR can also be tested with the Drude force field, a polarizable force field based on the classical Drude oscillator. The Drude force field can more accurately describe electrostatic interactions in MD simulation, but at $\sim 2\times$ the computational cost, which could be mitigated by combining it with HMR.

Appendices

APPENDIX A

COMPUTATIONAL METHODS

A.1 MD simulation

MD simulations solve Newtons equations of motion for a system of N interacting atoms as

$$m_i \frac{\partial^2 r_i}{\partial t^2} = F_i, i = 1...N. \tag{A.1}$$

where the forces are the negative derivatives of a potential function $U(r_1, r_2, ..., r_N)$:

$$F_i = \frac{\partial U}{\partial r_i} \tag{A.2}$$

The equations are solved simultaneously in small time steps. The system is followed for some time, taking care that the temperature and pressure remain at the required values, and the coordinates are written to an output file at regular intervals. The coordinates as a function of time represent a trajectory of the system. After initial changes, the system will usually reach an equilibrium state. By averaging over an equilibrium trajectory, many macroscopic properties can be extracted from the output file.

A.2 Steered MD

Steered molecular dynamics (SMD) is a technique used to force a selection of atoms within a system along a desired direction or reaction coordinate. This process involves attaching an imaginary bead via an imaginary spring to the aforementioned selection of atoms and then proceeding to pull this imaginary particle at a constant speed or constant force. For the membrane deformation simulations, constant speed SMD was performed to pull the drugs from outside of the membrane to the center of the membrane with a speed of 0.5 Å/ns.

APPENDIX B

SUPPLEMENTAL INFORMATION

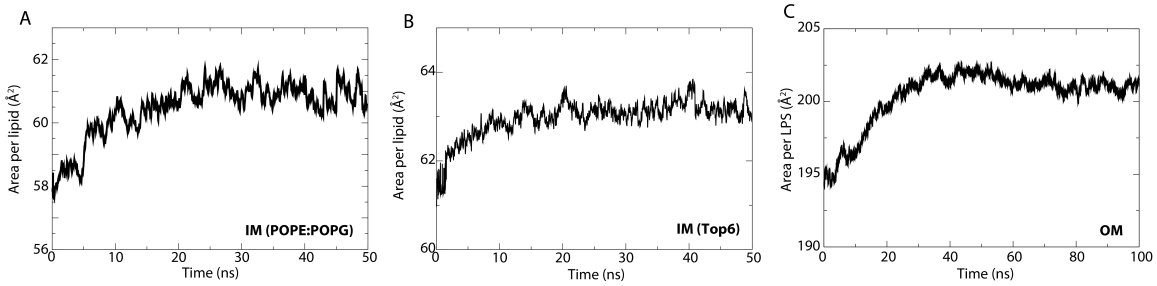

Figure B.1: Area per lipid/LPS over time for the first simulated tension for (A) POPE:POPG IM, (B) Top6 IM, and (C) OM. The average area for the latter half of the simulation for the POPE:POPG IM is 60.02 $\pm$ 0.42 Å^2, for the Top6 IM is 63.55 $\pm$ 0.59 Å^2, and for the OM is 201.39 $\pm$ 1.40 Å^2.

B.1 Membranes with a protein

IM models with embedded proteins. Protein-lipid interactions are an essential part of cell physiology. The membrane is estimated to have $\sim$25% or more of its area covered by proteins, yet their effects on mechanical properties is often neglected [51, 49]. Thus, we examined the impact of proteins on the elastic properties of membranes using the same protocol as for pure IM simulations. Both IM models with 25% the area occupied by an Aquaporin Z tetramer were subjected to incremental stretching over multiple runs. As seen in Fig. B.3, the slopes of linear fits for each membrane were determined, giving K_{A} values of 199 and 218 mN/m for POPE/POPG and Top6, respectively. These values are larger than for pure membrane (182 mN/m for POPE/POPG and 195 mN/m for Top6), indicating that the proteins stiffen the membrane.

Bilayer rupture by incremental tension and stress-softening. Rupture occurred at the last data point of each IM simulated. The POPE/POPG membrane ruptured at a tension of 79 mN/m when it was stretched to 92% over its relaxed area. The Top6 membrane ruptured at 78 mN/m when it was stretched to 107% over its relaxed area. Both inner membranes exhibit an inelastic response after 40% of area expansion. The slope (K_{A}) of the graph using the last few data points

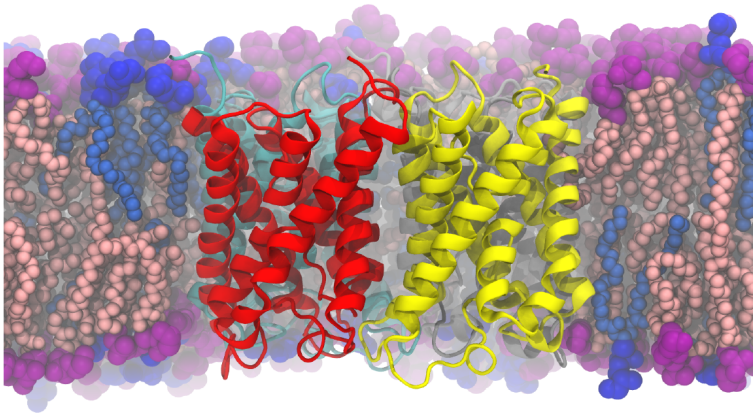

Figure B.2: Simulation model of one of the inner membranes (3:1 POPE:POPG) with an embedded Aquaporin Z tetramer (red, yellow, cyan, and tan, respectively). The proteins occupy 25% of the system's lateral area.

Figure B.3: Tension-pressure isotherms for inner-membrane models with 25% of the area occupied by AqpZ tetramer. R^2 values from the linear regression were 0.95 and higher for all IM models.

were determined to be 15 mN/m and 26 mN/m for POPE/POPG and Top6 membrane, respectively, indicative of significant strain softening preceding rupture.

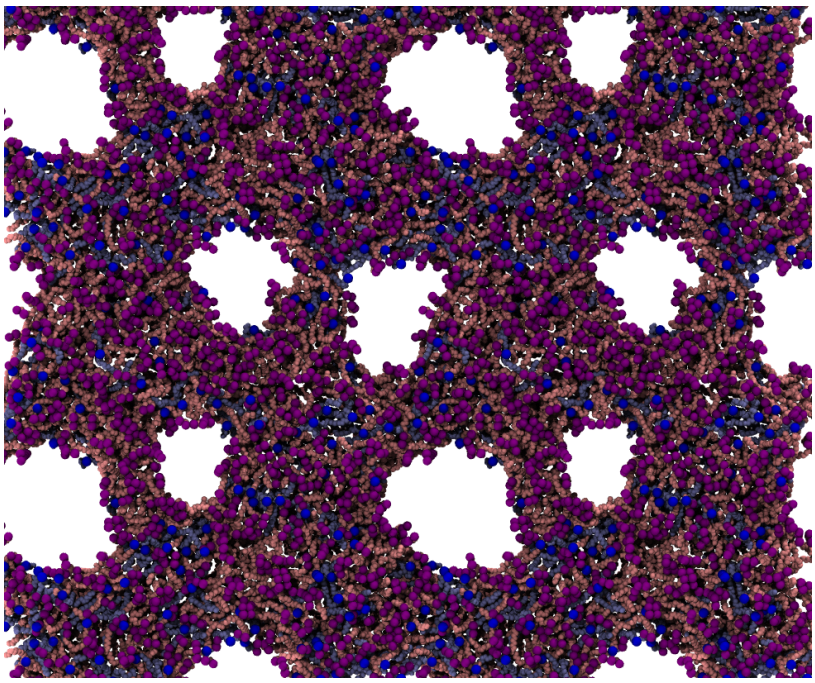

Figure B.4: Top view of a ruptured POPE/POPG membrane. Water pores form due to the surface tension applied at a critical value. POPE lipids are shown as pink tails/purple head groups, while POPG lipids are blue. Water molecules are not shown.

OM models with embedded proteins. The area compressibility (K_A) of the OM with an embedded OmpF trimer (Fig. B.5) was found to be 528 mN/m in simulation (Fig. B.6), which is practically identical to the pure OM (524 mN/m). The difference in alteration of the stiffness of the OM, if any, is much less apparent than both of the IM models. This suggests that the resistance to area expansion of OmpF is greater than Aquaporin Z.

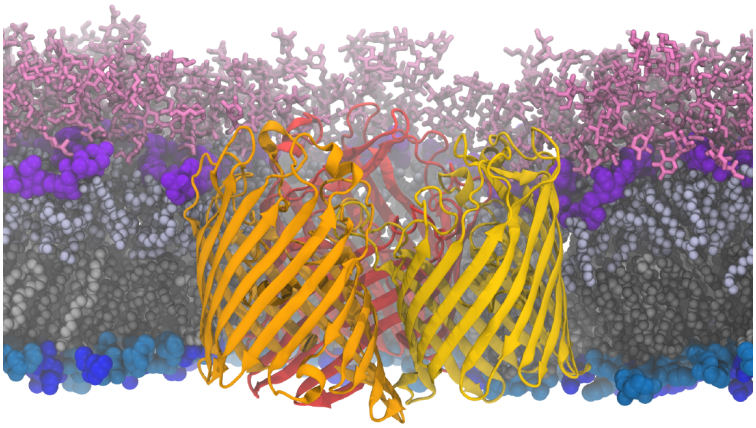

Figure B.5: (A) Model of the OM with an embedded OmpF trimer. The hydrophobic region is shown as grey space-filling spheres. The head groups are in purple (LPS), cyan (POPE), and blue (POPG). The core oligosaccharide is shown as pink sticks. OmpF is in orange, yellow, and red cartoon representation.

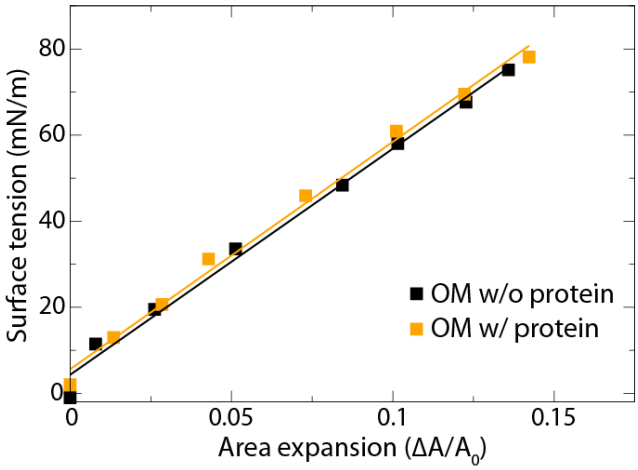

Figure B.6: Tension-area isotherms for the OM model. The pure OM is repeated from Fig. 3 in the main text; the OM with an embedded OmpF trimer (25% by area) is in orange. The R^2 values are 0.97 and 0.98 for the pure OM and protein-containing OM, respectively.

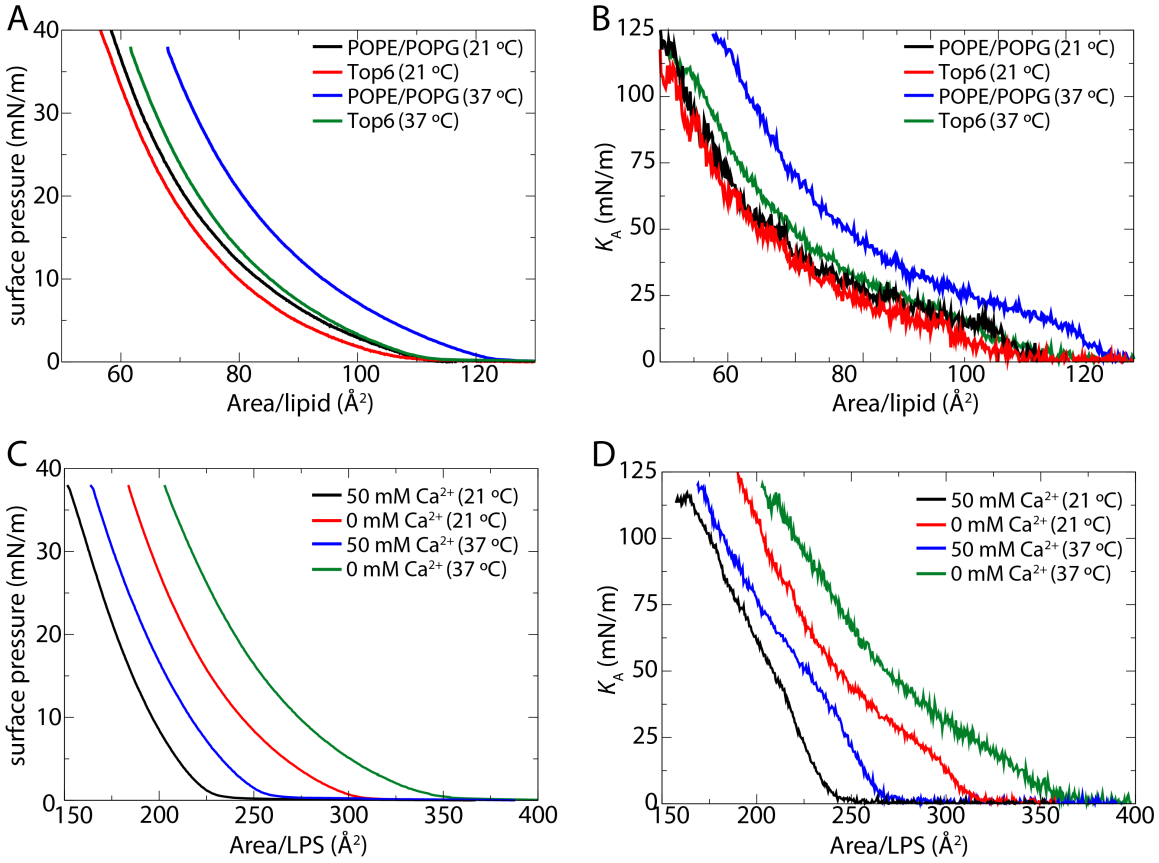

Figure B.7: Surface pressure-area isotherms and area compressibility (K_A) for monolayers as a function of temperature. (A) Surface pressure-area isotherms and (B) K_A for IM models at 21 °C and 37 °C. (C) Surface pressure-area isotherms and (D) K_A for LPS monolayers at 21 °C and 37 °C.

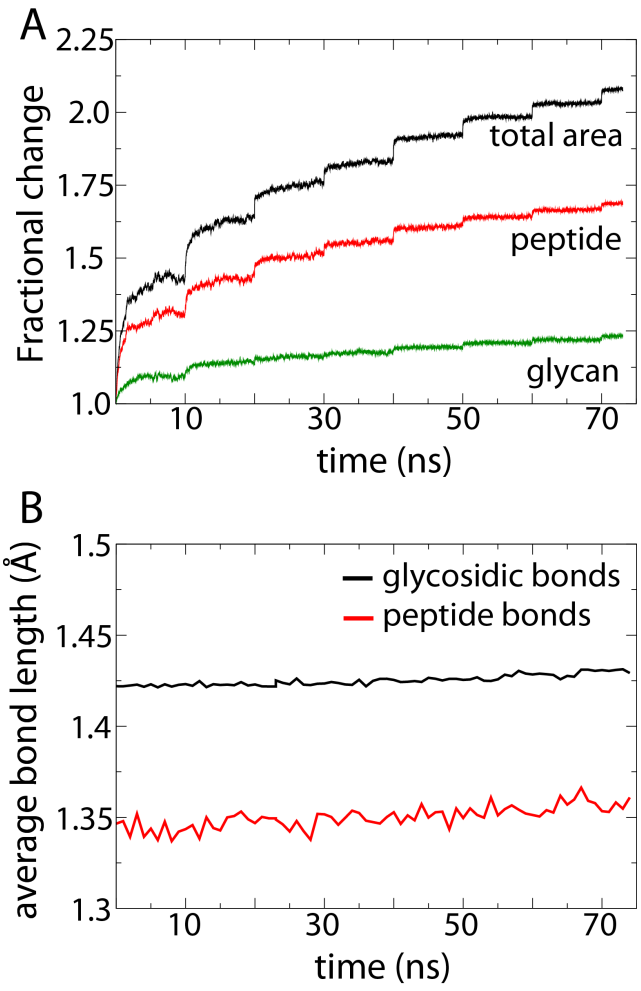

Figure B.8: Cell wall properties under applied surface tension. (A) Change in area and individual peptide and glycan-strand dimensions over time. The surface tension was increased every 10 ns. (B) Average bond length for glycosidic bonds and peptide bonds over time for the same simulations.

B.2 Calculating distribution of stress

The Young-Laplace relation for a cylinder is given by

$$\Delta P = \frac{\gamma}{R} \tag{B.1}$$

where ΔP is the pressure drop across the boundary, R is the radius, and γ is the induced surface tension. We can expand it to account for multiple layers as

$$\Delta P_{\text{total}} = \Delta P_{\text{IM}} + \Delta P_{\text{OM}} + \Delta P_{\text{CW}} = \frac{\gamma_{\text{IM}}}{R} + \frac{\gamma_{\text{OM}}}{R} + \frac{\gamma_{\text{CW}}}{R} \tag{B.2}$$

in which we have made the approximation that the three cell envelope components, inner membrane (IM), outer membrane (OM), and cell wall (CW), are closely packed on the scale of the cell and, thus, have roughly the same radius. The surface tension can be expressed in terms of the area compressibility K_{A} as

$$\gamma = \sigma t = (E\epsilon)\, t = K_{\text{A}}(1-\nu^2)\epsilon \tag{B.3}$$

where ν is the dimensionless Poisson's ratio for the material, σ is the surface stress, t is the layer thickness, ϵ is the strain, and E is Young's modulus. We made use of the relationship between K_{A} and E [34]

$$K_{\text{A}} = Et\frac{1}{1-\nu^2}. \tag{B.4}$$

If we also assume that due to close packing, the individual strains in each layer are identical, then

$$\Delta P_{\text{total}} = \left[K_{\text{A}}^{\text{IM}}(1-\nu_{\text{IM}}^2) + K_{\text{A}}^{\text{OM}}(1-\nu_{\text{OM}}^2) + K_{\text{A}}^{\text{CW}}(1-\nu_{\text{CW}}^2)\right]\frac{\epsilon}{R}. \tag{B.5}$$

As membranes are commonly considered nearly incompressible, we take the Poisson's ratios ν_{IM} and ν_{OM} to be 0.5, as used in other works [205]. For the cell wall, the Poisson's ratio is anisotropic and, thus,

$$1-\nu_{\text{CW}}^2 = 1-\nu_{\text{gp}}\nu_{\text{pg}} \tag{B.6}$$

where the subscripts gp and pg indicate the spontaneous strain in one direction given an applied strain in the other; g and p refer to glycan and peptide directions, respectively. From previous work, we take these values to be $\nu_{\mathrm{gp}} = 0.324$ and $\nu_{\mathrm{pg}} = 0.087$ for the cell wall model used here [5]. Finally, we arrive at the relationship between turgor pressure, cell radius, strain, and the area compressibilities of the individual components of the cell envelope:

$$\Delta P_{\mathrm{total}} = \left[0.75K_{\mathrm{A}}^{\mathrm{IM}} + 0.75K_{\mathrm{A}}^{\mathrm{OM}} + 0.97K_{\mathrm{A}}^{\mathrm{CW}}\right] \frac{\epsilon}{R}. \tag{B.7}$$

If we take the values $r = 500\,\mathrm{nm}$ and $\epsilon = dr/r = 0.03$ as measured for *E. coli* subjected to hypoosmotic shock [88] and assume $\Delta P_{\mathrm{total}} = 1.0\,\mathrm{atm}$, we find that

$$\left[0.75K_{\mathrm{A}}^{\mathrm{IM}} + 0.75K_{\mathrm{A}}^{\mathrm{OM}} + 0.97K_{\mathrm{A}}^{\mathrm{CW}}\right] \approx 1689\,\mathrm{mN/m}. \tag{B.8}$$

Using values found in our experiments for the IM (240 mN/m) and OM (237 mN/m), we conclude that $K_{\mathrm{A}}^{\mathrm{CW}} = 1372\,\mathrm{mN/m}$, nearly an order of magnitude greater than in our simulations at areas up to $2\times$ the relaxed area (see Fig. 5 in the main text). Furthermore, from Eq. B.4, for a cell wall of thickness 4 nm [4, 5], the elasticity E would be $343\,\mathrm{MPa}$, also an order of magnitude greater than practically all estimates [87].

We also calculated $K_{\mathrm{A}}^{\mathrm{CW}}$ assuming that the IM can not be responsible for bearing any pressure; this is supported by multiple lines of evidence that point to the periplasm being isoosmotic with the cytoplasm [17, 29]. If so, the IM will not respond to turgor pressure under typical conditions; instead, the OM and cell wall will work together to withstand it. Under this assumption, we get $K_{\mathrm{A}}^{\mathrm{CW}}$ = 1558 mN/m and 1336 mN/m with experimental and simulated $K_{\mathrm{A}}^{\mathrm{OM}}$ values, respectively. Again, these $K_{\mathrm{A}}^{\mathrm{CW}}$ values are an order of magnitude greater than our simulated value or experimental estimates.

If, on the other hand, we assume $\Delta P_{\mathrm{total}} = 0.3\,\mathrm{atm}$, which has been measured in experiments probing the cell wall mechanically [19, 20], we find

$$\left[0.75K_{\mathrm{A}}^{\mathrm{IM}} + 0.75K_{\mathrm{A}}^{\mathrm{OM}} + 0.97K_{\mathrm{A}}^{\mathrm{CW}}\right] \approx 507\,\mathrm{mN/m}, \tag{B.9}$$

Table B.1: Calculated $K_{\mathrm{A}}^{\mathrm{CW}}$ based on $K_{\mathrm{A}}^{\mathrm{IM}}$ from experiment and $K_{\mathrm{A}}^{\mathrm{OM}}$ from either experiment[a] or simulation[b]. A blank entry indicates that the IM is assumed to bear no pressure.

	ΔP = **1 atm**			ΔP = **0.3 atm**		
$K_{\mathrm{A}}^{\mathrm{OM}} = 237\,\mathrm{mN/m}$	IM	OM[a]	CW	IM	OM[a]	CW
K_{A} (mN/m)	240	237	1372	240	237	154
%	10.7	10.5	78.8	35.5	35.0	29.5
K_{A} (mN/m)		237	1558		237	339
%		10.5	89.5		35.1	64.9
$K_{\mathrm{A}}^{\mathrm{OM}} = 524\,\mathrm{mN/m}$	IM	OM[b]	CW	IM	OM[b]	CW
K_{A} (mN/m)	240	524	1151	240	524	-
%	10.6	23.3	66.1	31.4	68.6	-
K_{A} (mN/m)		524	1336		524	118
%		23.3	76.7		77.5	22.5

from which we conclude $K_{\mathrm{A}}^{\mathrm{CW}} = 154\,\mathrm{mN/m}$, slightly less than that found in our simulations of the cell wall at $2\times$ its relaxed area. Under these assumptions, the IM, OM, and cell wall each bear roughly one-third of the pressure.

Finally, we consider the possibility that K_{A} for the OM is equal to our simulated value, 524 mN/m, which should represent an upper limit. In this case, $K_{\mathrm{A}}^{\mathrm{CW}}$ is effectively 0, i.e., the OM bears nearly 70% of the pressure and the IM bares the rest. If we assume that the IM plays no role, then the cell wall bares $\sim$20% of the pressure and the OM $\sim$80% instead.

APPENDIX C

SUPPLEMENTAL INFORMATION

C.1 Molecular properties of chosen drugs

Table C.1: Molecular properties and calculated Log$P$ of drugs

Compounds	MW (g/mol)	V (A^3)	CSA (A^2)	Surface area	Polar surface area	Porlar area %	# of polar atom	RRCK Log$P$	Calculated Log$P$ MAM.	Calculated Log$P$ DMPC	PAMPA Log$P$
Acyclovir	225.21	705.82	38.30	395.55	217.98	55.11	12	-6.52	-6.2	-6.52	-
Lisinopril	405.49	1175.51	63.18	601.3	201.13	33.45	13	-6.30	-5.98	-5.9	-6.70
Tetracycline	444.44	1208.70	63.31	596.46	247.65	41.52	17	-6.15	-5.99	-6.41	-5.54
Azithromycin	748.99	2043.24	102.31	872.51	111.44	12.77	19	-6.15	-6.23	-6.9	-
Chlorothiazide	295.72	725.62	38.00	399.1	132.4	33.17	10	-5.89	-5.32	-5.99	-
Pravastatin	424.53	1304.07	71.31	656.54	207.42	31.59	11	-5.68	-5.43	-5.78	-
Indinavir	613.80	1824.56	93.46	759.55	59.64	7.85	13	-5.47	-5.78	-5.62	-3.6
Ketoconazole	531.44	1467.36	78.01	757.81	87.83	11.59	8	-5.38	-5.69	-5.89	-1.46
Ritonavir	724.98	1959.47	102.32	832.1	180.3	21.67	15	-5.08	-5.42	-5.74	-1.68
Chlorpromazine	318.86	1017.39	50.65	512.62	4.93	0.96	2	-4.99	-5.21	-5.32	-0.22
Acetaminophen	151.17	567.70	23.52	308.92	101.14	32.74	5	-4.91	-5.82	-3.43	-4.12
Ibuprofen	206.28	800.00	34.01	431.073	83.45	19.36	3	-4.52	-2.97	-2.53	-4.92
Diazepam	284.74	895.64	52.36	524.64	30	5.72	2	-4.44	-4.73	-5.53	-2.44
Tamoxifen	371.52	1302.69	60.01	380.63	15	3.94	2	-4.24	-4.14	-5.15	0.78
Levodopa	197.19	641.05	33.35	201.2	103.78	51.58	10	-3.78	-3.10	-3.98	-7.52

APPENDIX D

SUPPLEMENTAL INFORMATION

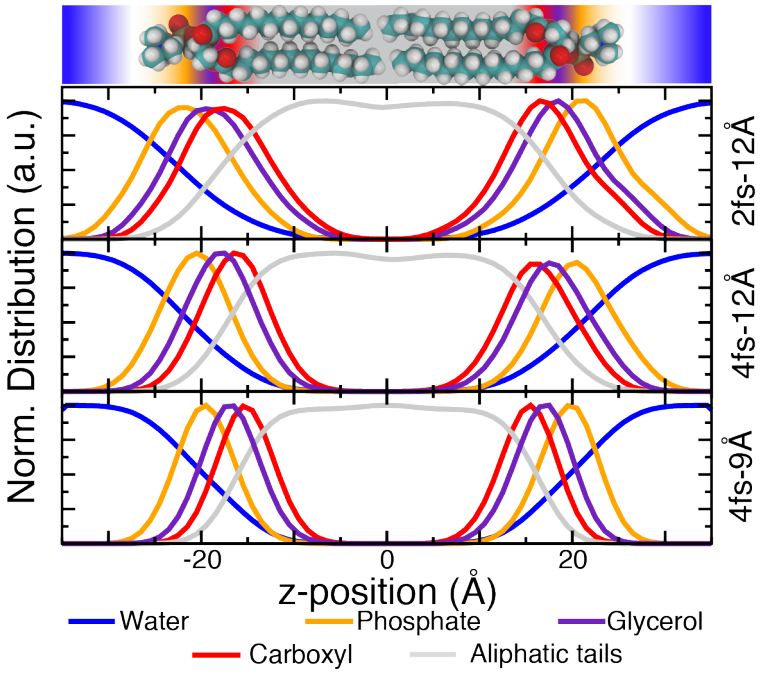

Figure D.1: Plot of molecular densities of DPPC in the 2-12(top), 4-12(middle), and 4-9(bottom) simulations. The overlap in aliphatic tails (grey) is shown to increase from 2-12and 4-12to 4-9suggesting that the shorter (9Å) cutoff compresses and interdigitates the lipid tails more than the 12Å cutoff.

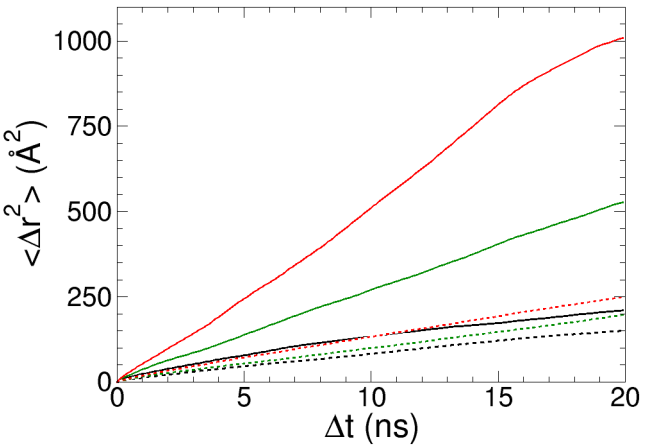

Figure D.2: Diffusion plot of DPPC simulated using Lowe-Anderson thermostat (solid) with the langevin piston simulations (dashed) as reference. The 2-12simulations are shown in black, 4-12in green and 4-9in red. Applying the Lowe-Anderson thermostat results in significantly larger diffusion values across all simulation protocols. Increases in diffusion are approximately 70% in for the 2-12system and grow to 300% when comparing the 4-9system.

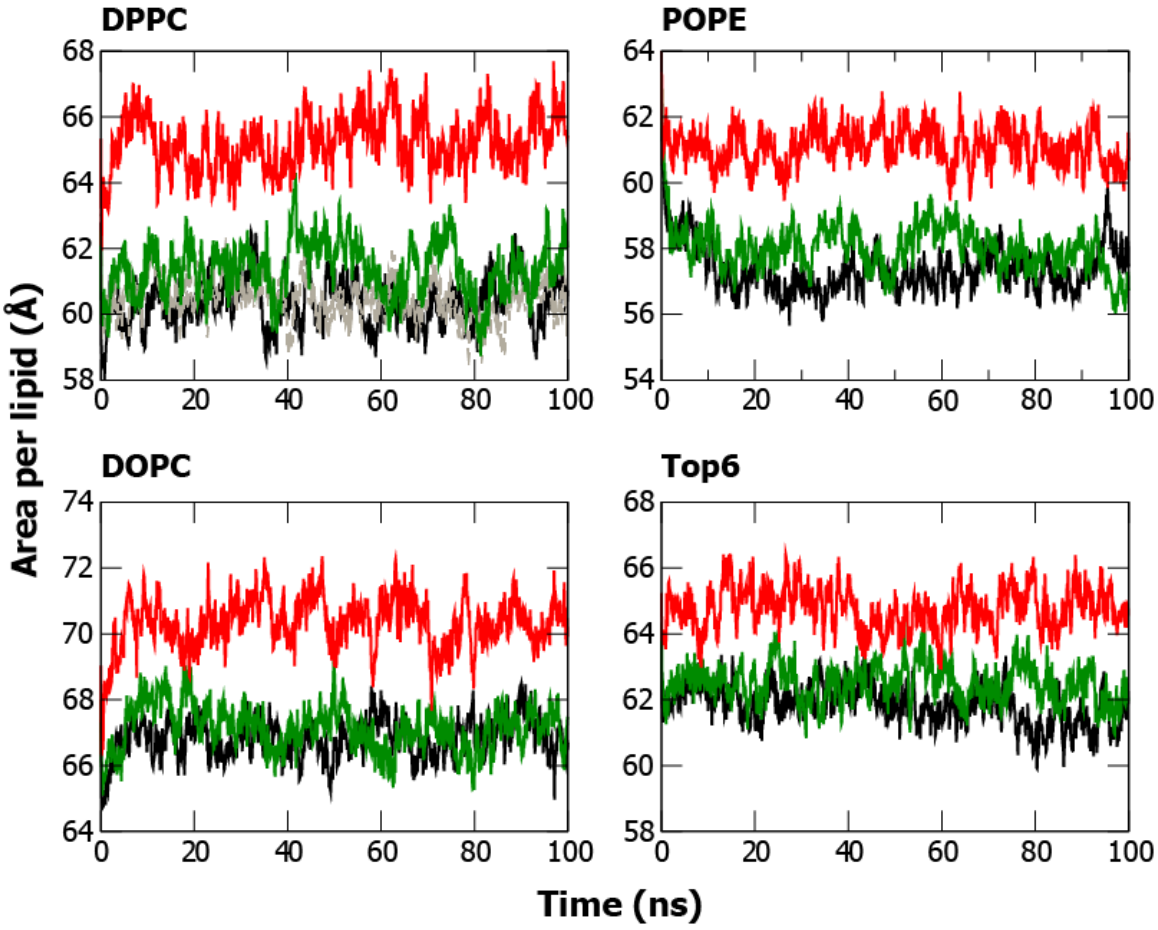

Figure D.3: Plots of Area per lipid over 100 ns simulation period. Results presented for analysis were obtained from the last 50 ns of each simulation. In each panel, 2-12 in shown black, 4-12 in green, and 4-9 in red. A separate 2-12-HMR simulation performed in the DPPC (top left) bilayer is shown in grey.

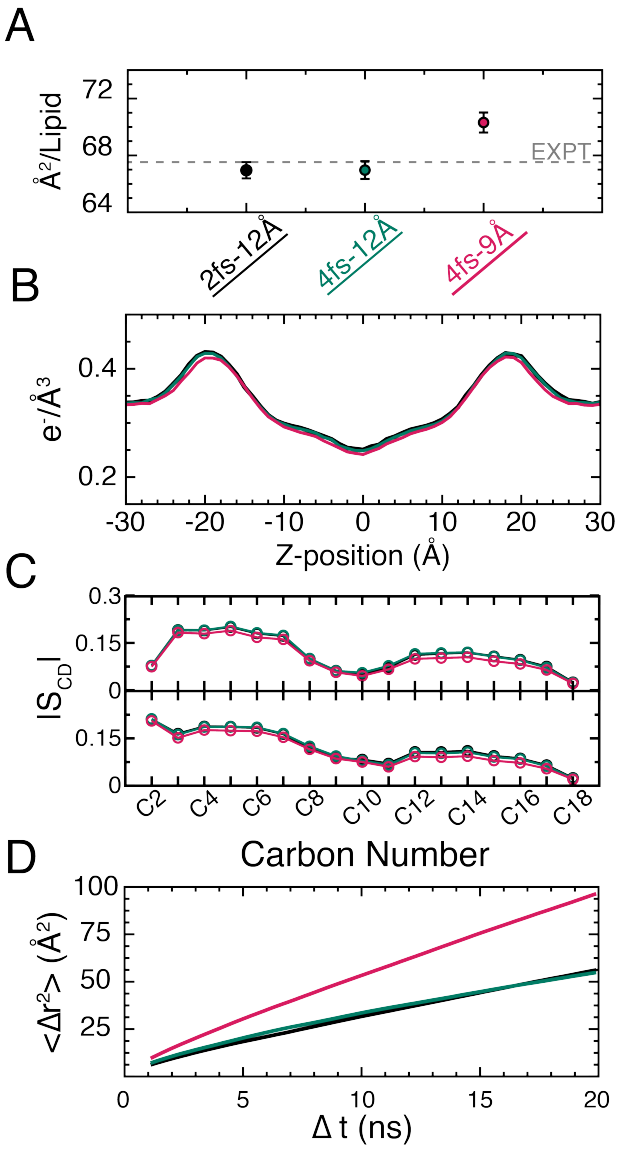

Figure D.4: Plot Summary information for large DOPC system. A) Area per lipid for the three systems tested. B) Electron Density plots. C) Order parameters for Sn2 (top) and Sn1 (bottom). D) Diffusion Plots.

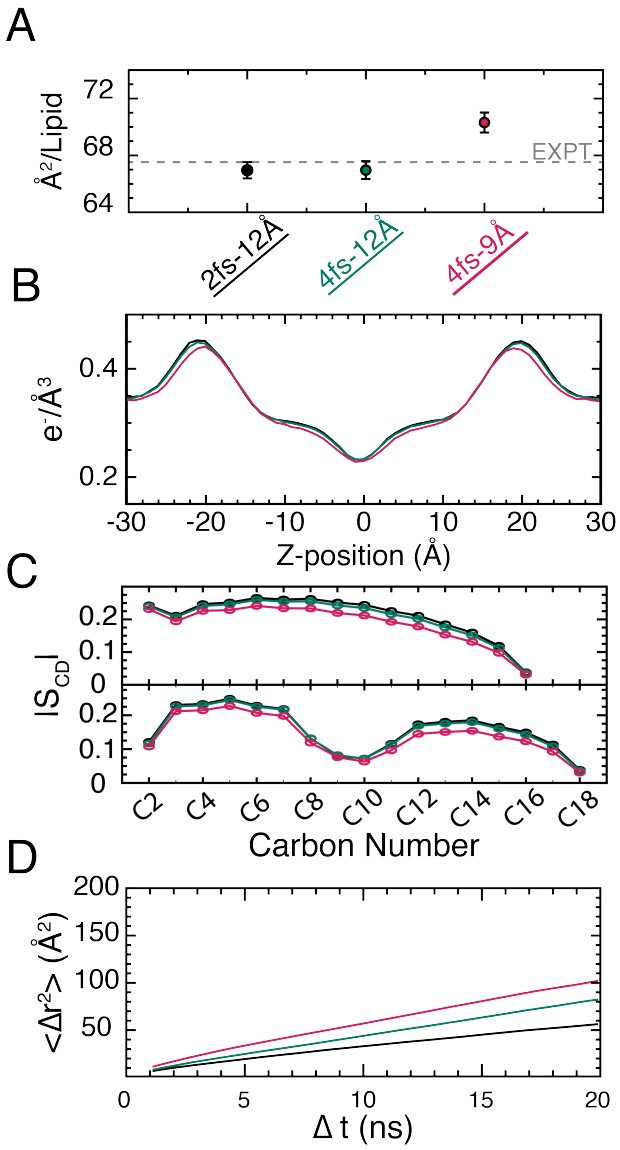

Figure D.5: Plot Summary information for large POPE system. A) Area per lipid for the three systems tested. B) Electron Density plots. C) Order parameters for Sn1 (top) and Sn2 (bottom). D) Diffusion Plots.

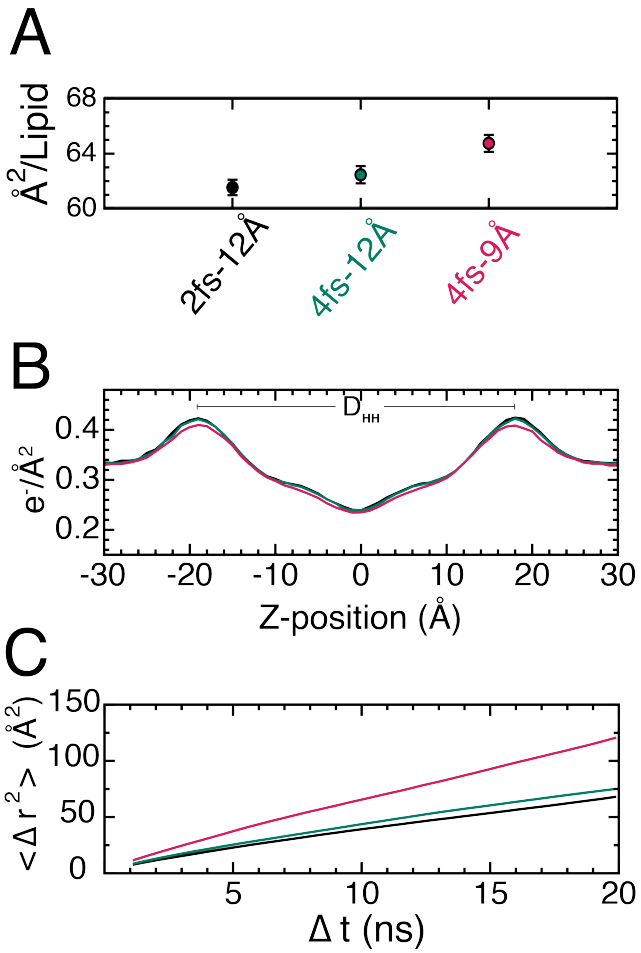

Figure D.6: Plot Summary information for Top6 system. A) Area per lipid for the three systems tested. B) Electron Density plots. C) Diffusion Plots.

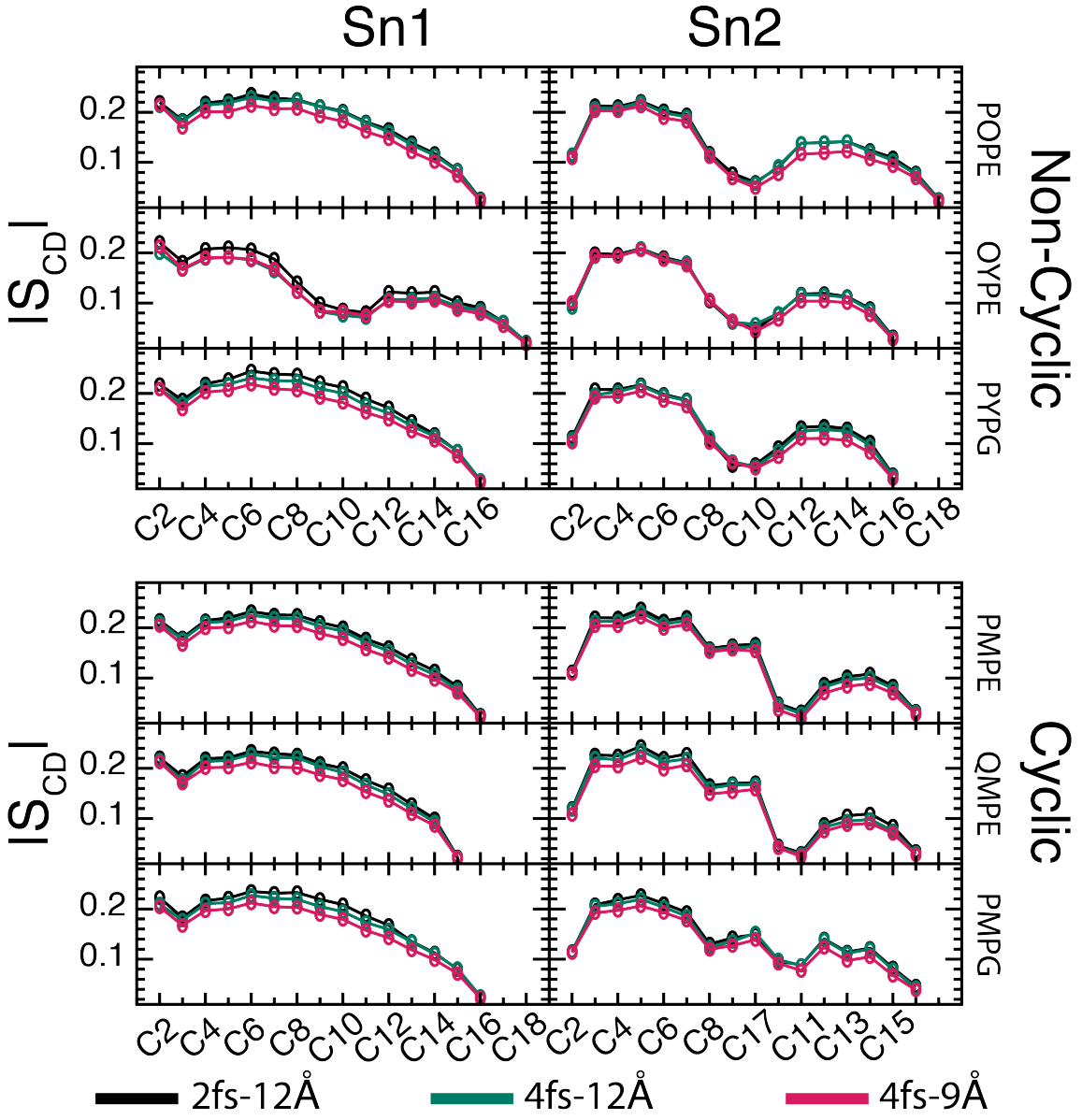

Figure D.7: Plots of order parameters from Top6 systems. 2-12 shown in black, 4-12 shown in green, and 4-9 in red. Left column are the Sn1 tails and right column Sn2. Upper cluster are non-cyclic order parameters and the lower group are cyclic containing tails. Bottom Right panel has C17 (the cyclic carbon) inserted between C9 and C10.

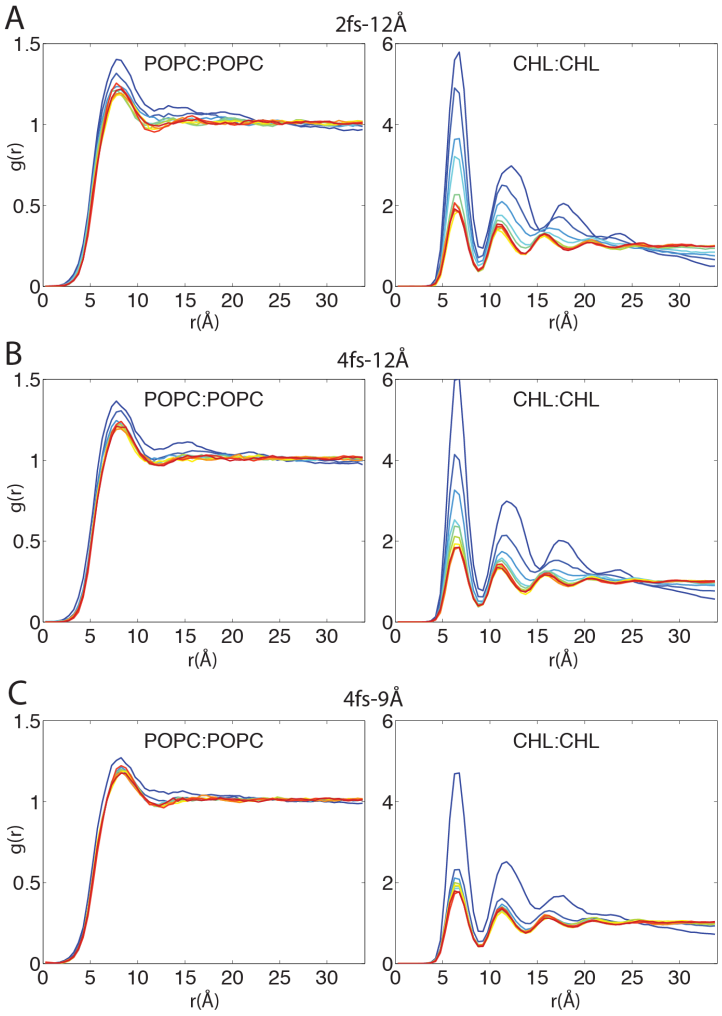

Figure D.8: Time evolution of the radial pair distribution functions g(r) for POPC:POPC and CHL:CHL from the 2-12 simulation (a), the 4-12 simulation (b), and the 4-9 simulation (c). Calculated g(r) is averaged in 100-ns blocks and colored by simulation time, with blue, green and red indicating the beginning, the middle and the end of a simulation, respectively.

System	Lipid Top:Bottom	Atom Count	H_2O/Lipid	Ions
DPPC	240:240	113064	35.125	84
POPE	240:240	107969	33.25	80
DOPC	240:240	122505	39.0	96
Top6	PMPE 116:116 POPE 32:32 QMPE 32:32 PMPG 24:24 PYPG 20:20 OYPE 16:16	109605	35.26	176
OmpF	POPE 88:88	99154	115.84	819
GPCR				
L8	POPE 53:52	26696	39.57	0

Table D.1: Summary of systems.

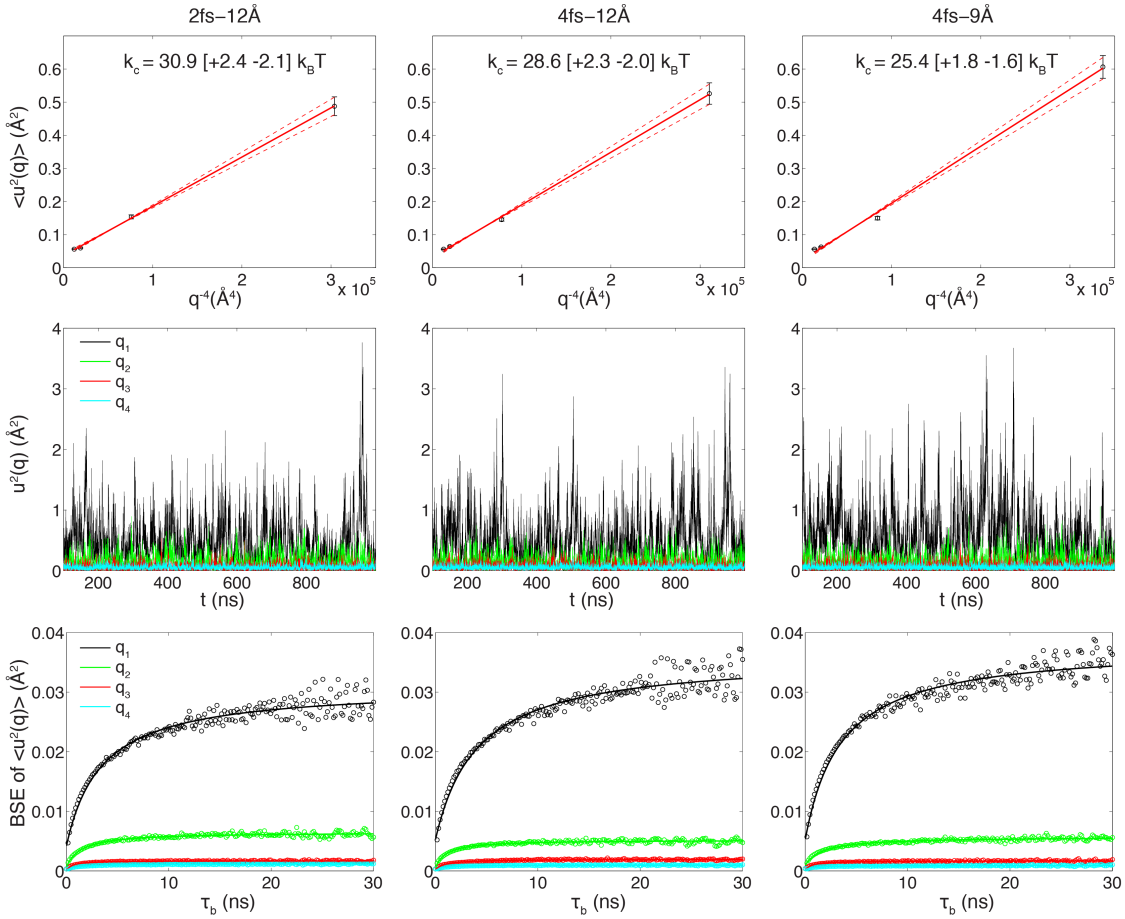

Figure D.9: Undulation analysis of a POPC bilayer with 680 lipids. (a) The bending modulus k_c obtained from the slope of $\langle u^2(q)\rangle$ versus q^{-4}. The estimated uncertainty in k_c is given in square brackets. (b) $u^2(q)$ as a function of simulation time. (c) The blocked standard error (BSE) in $\langle u^2(q)\rangle$ as a function of the block size τ_b. Results of the lowest wavenumber ($q_1 \approx 0.04$ Å^{-1}) are colored in black circles, with the black solid curve representing a least square fit using a rational polynomial function. Similarly, results for the next three wavenumbers are colored in green, red and blue, respectively.

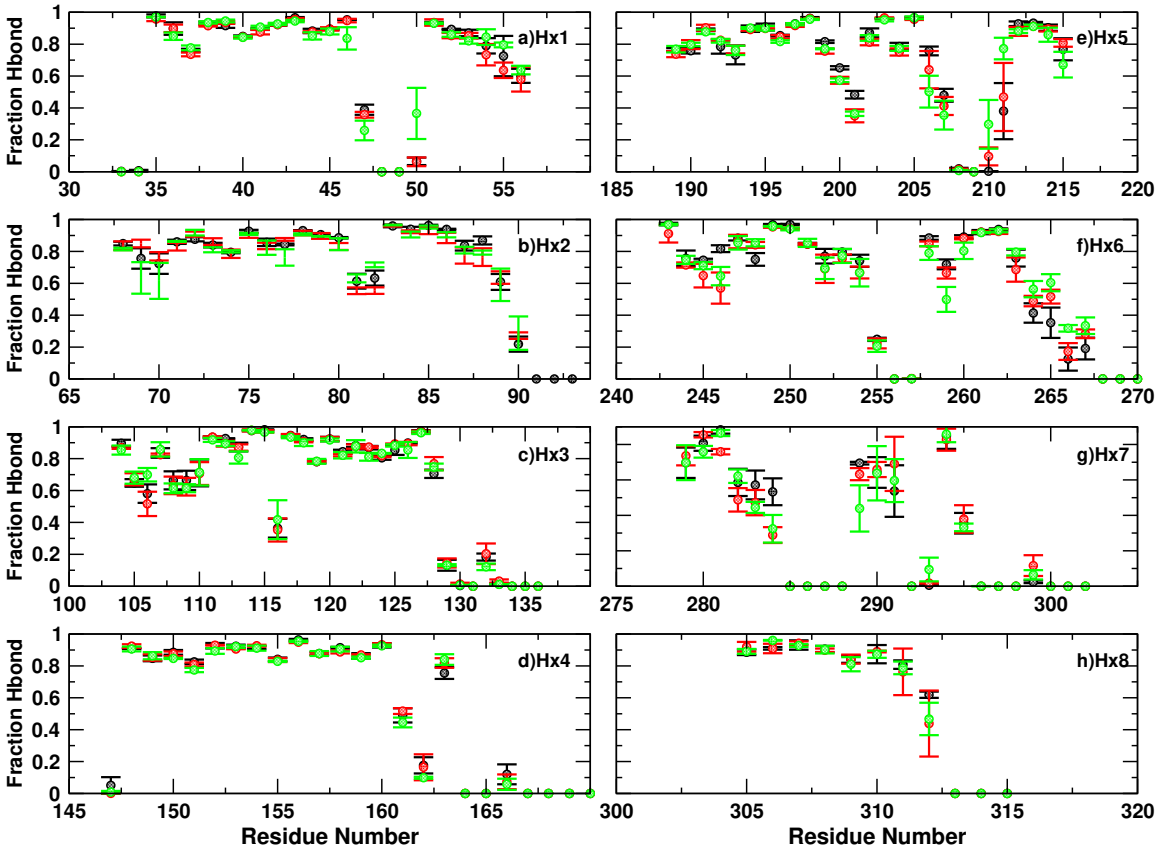

Figure D.10: Transmembrane hydrogen bonding between i and i+4 residues for each of the seven transmembrane $\alpha-$helices of CB2, as well as Helix 8. Left Column: a) Transmembrane helix 1, b) Transmembrane helix 2, c) Transmembrane helix 3, d) Transmembrane helix 4. Right Column: e) Transmembrane helix 5, f) Transmembrane helix 6, g) Transmembrane helix 7, h) helix 8. 2-12data is black, 4-12data is red, and 4-9data is green.

REFERENCES

[1] T. J. Silhavy, D. Kahne, and S. Walker, "The bacterial cell envelope," *Cold Spring Harb. Perspect. Biol.*, vol. 2, a000414, 2010.

[2] C. R. Raetz and C. Whitfield, "Lipopolysaccharide endotoxins," *Annu. Rev. Biochem.*, vol. 71, pp. 635–700, 2002.

[3] H. Nikaido, "Molecular basis of bacterial outer membrane permeability revisited," *Microbiol. Mol. Biol. Rev.*, vol. 67, pp. 593–656, 2003.

[4] L. Gan, S. Chen, and G. J. Jensen, "Molecular organization of Gram-negative peptidoglycan," *Proc. Natl. Acad. Sci. USA*, vol. 105, pp. 18 953–18 957, 2008.

[5] J. C. Gumbart, M. Beeby, G. J. Jensen, and B. Roux, "*Escherichia coli* peptidoglycan structure and mechanics as predicted by atomic-scale simulations," *PLoS Comput. Biol.*, vol. 10, e1003475, 2014.

[6] M. Beeby, J. C. Gumbart, B. Roux, and G. J. Jensen, "Architecture and assembly of the Gram-positive cell wall," *Mol. Microbiol.*, vol. 88, pp. 664–672, 2013.

[7] E. I. Tocheva, J. Lopez-Garrido, H. V. Hughes, J. Fredlund, E. Kuru, M. S. Vannieuwenhze, Y. V. Brun, K. Pogliano, and G. J. Jensen, "Peptidoglycan transformations during *Bacillus subtilis* sporulation," *Mol. Microbiol.*, vol. 88, pp. 673–686, 2013.

[8] W. Vollmer, D. Blanot, and M. A. de Pedro, "Peptidoglycan structure and architecture," *FEMS Microbiol. Rev.*, vol. 32, pp. 149–167, 2008.

[9] Z. Gitai, N. A. Dye, A. Reisenauer, M. Wachi, and L. Shapiro, "MreB actin-mediated segregation of a specific region of a bacterial chromosome," *Cell*, vol. 120, pp. 329–341, 2005.

[10] K. E. Daly, K. C. Huang, N. S. Wingreen, and R. Mukhopadhyay, "Mechanics of membrane bulging during cell-wall disruption in Gram-negative bacteria," *Phys. Rev. E*, vol. 83, p. 041 922, 2011.

[11] A. L. Koch, "The biophysics of the Gram-negative periplasmic space," *Crit. Rev. Microbiol.*, vol. 24, pp. 23–59, 1998.

[12] W. Vollmer and S. J. Seligman, "Architecture of peptidoglycan: More data and more models," *Trends Microbiol.*, vol. 18, pp. 59–66, 2010.

[13] H. Y. Jiang and S. X. Sun, "Morphology, growth, and size limit of bacterial cells," *Phys. Rev. Lett.*, vol. 105, p. 028 101, 2010.

[14] L. Furchtgott, N. S. Wingreen, and K. C. Huang, "Mechanisms for maintaining cell shape in rod-shaped Gram-negative bacteria," *Mol. Microbiol.*, vol. 80, pp. 340–353, 2011.

[15] E. Rojas, J. A. Theriot, and K. C. Huang, "Response of *Escherichia coli* growth rate to osmotic shock," *Proc. Natl. Acad. Sci. USA*, vol. 111, pp. 7807–7812, 2014.

[16] E. R. Rojas, G. Billings, P. D. Odermatt, G. K. Auer, L. Zhu, A. Miguel, F. Chang, D. B. Weibel, J. A. Theriot, and K. C. Huang, "The outer membrane is an essential load-bearing element in Gram-negative bacteria," *Nature*, 2018, In press.

[17] D. S. Cayley, H. J. Guttman, and M. T. Record Jr., "Biophysical characterization of changes in amounts and activity of *Escherichia coli* cell and compartment water and turgor pressure in response to osmotic stress," *Biophys. J.*, vol. 78, pp. 1748–1764, 2000.

[18] M. Arnoldi, M. Fritz, E. Buerlein, M. Radmacher, E. Sackmann, and A. Boulbitch, "Bacterial turgor pressure can be measured by atomic force microscopy," *Phys. Rev. E*, vol. 62, pp. 1034–1044, 2000.

[19] X. Yao, J. Walter, S. Burke, S. Stewart, M. H. Jericho, D. Pink, R. Hunter, and T. J. Beveridge, "Atomic force microscopy and theoretical considerations of surface properties and turgor pressures of bacteria," *Colloids Surfaces B: Biointerfaces*, vol. 23, pp. 213–230, 2002.

[20] Y. Deng, M. Sun, and J. W. Shaevitz, "Direct measurement of cell wall stress stiffening and turgor pressure in live bacterial cells," *Phys. Rev. Lett.*, vol. 107, pp. 158 101–1–158101–4, 2011.

[21] V. R. F. Matias, A. Al-Amoudi, J. Dubocher, and T. J. Beveridge, "Cryo-transmission electron microscopy of frozen-hydrated sections of *Escherichia coli* and *Pseudomonas aeruginosa*," *J. Bacteriol.*, vol. 185, pp. 6112–6118, 2003.

[22] A. T. Asmar, J. L. Ferreira, E. J. Cohen, S. H. Cho, M. Beeby, K. T. Hughes, and J. F. Collet, "Communication across the bacterial cell envelope depends on the size of the periplasm," *PLoS Biol.*, vol. 15, e2004303, 2017.

[23] V. Braun, "Covalent lipoprotein from the outer membrane of *Escherichia coli*," *Biochim. Biophys. Acta*, vol. 415, pp. 335–377, 1975.

[24] W. Shu, J. Liu, H. Ji, and M. Lu, "Core structure of the outer membrane lipoprotein from *Escherichia coli* at 1.9 Å resolution," *J. Mol. Biol.*, vol. 299, pp. 1101–1112, 2000.

[25] F. Samsudin, M. L. Ortiz-Suarez, T. J. Piggot, P. J. Bond, and S. Khalid, "OmpA: A flexible clamp for bacterial cell wall attachment," *Structure*, vol. 24, pp. 2227–2235, 2016.

[26] E. Cascales, A. Bernadac, M. Gavioli, J.-C. Lazzaroni, and R. Lloubes, "Pal lipoprotein of *Escherichia coli* plays a major role in outer membrane integrity," *J. Bacteriol.*, vol. 184, pp. 754–759, 2002.

[27] H. Suzuki, Y. Nishimura, S. Yasuda, A. Nishimura, M. Yamada, and Y. Hirota, "Murein-lipoprotein of *Escherichia coli*: A protein involved in the stabilization of bacterial cell envelope," *Molec. Gen. Genet.*, vol. 167, pp. 1–9, 1978.

[28] I. Sonntag, H. Schwarz, Y. Hirota, and U Henning, "Cell envelope and shape of *Escherichia coli*: Multiple mutants missing the outer membrane lipoprotein and other major outer membrane proteins," *J. Bacteriol.*, vol. 136, pp. 280–285, 1978.

[29] K. A. Sochacki, I. A. Shkel, M. T. Record, and J. C. Weisshaar, "Protein diffusion in the periplasm of *E. coli* under osmotic stress," *Biophys. J.*, vol. 100, pp. 22–31, 2011.

[30] P. Tieleman, H. Leontiadou, A. Mark, and S. Marrink, "Simulation of pore formation in lipid bilayers by mechanical stress and electric fields," *J. Am. Chem. Soc.*, vol. 125, pp. 6382–6383, 2003.

[31] A. S. Reddy, D. T. Warshaviak, and M. Chachisvilis, "Effect of membrane tension on the physical properties of DOPC lipid bilayer membrane," *Biochim. Biophys. Acta*, vol. 1818, pp. 2271–2281, 2012.

[32] D. Needham and R. S. Nunn, "Elastic deformation and failure of lipid bilayer membranes containing cholesterol," *Biophys. J.*, vol. 58, pp. 997–1009, 1990.

[33] K. Olbrich, W. Rawicz, D. Needham, and E. Evans, "Water permeability and mechanical strength of polyunsaturated lipid bilayers," *Biophys. J.*, vol. 79, pp. 321–327, 2000.

[34] W. Rawicz, K. C. Olbrich, T. McIntosh, D. Needham, and E. Evans, "Effect of chain length and unsaturation on elasticity of lipid bilayers," *Biophys. J.*, vol. 79, pp. 328–339, 2000.

[35] J. F. Nagle and S. Tristram-Nagle, "Structure of lipid bilayers," *Biochim. Biophys. Acta*, vol. 1469, pp. 159–195, 2000.

[36] K. J. Tierney, D. E. Block, and M. L. Longo, "Elasticity and phase behavior of DPPC membrane modulated by cholesterol, ergosterol and ethanol," *Biophys. J.*, vol. 89, pp. 2481–2493, 2005.

[37] G. Popescu, T. Ikeda, K. Goda, C. A. B. Popescu, and M. Laposata, "Optical measurement of cell membrane tension," *Phys. Rev. Lett.*, vol. 97, p. 218 101, 2006.

[38] J. B. Klauda, R. M. Venable, J. A. Freites, J. W. O'Connor, D. J. Tobias, C. Mondragon-Ramirez, I. Vorobyov, A. D. MacKerell Jr., and R. W. Pastor, "Update of the CHARMM all-atom additive force field for lipids: Validation on six lipid types," *J. Phys. Chem. B*, vol. 114, pp. 7830–7843, 2010.

[39] R. M. Venable, F. L. H. Brown, and R. W. Pastor, "Mechanical properties of lipid bilayers from molecular dynamics simulation," *Chem. Phys. Lipids*, vol. 192, pp. 60–74, 2015.

[40] H. Leontiadou, A. E. Mark, and S. J. Marrink, "Molecular dynamics simulations of hydrophilic pores in lipid bilayers," *Biophys. J.*, vol. 86, pp. 2156–2164, 2004.

[41] J. Neder, B. West, P. Nielaba, and F. Schmid, "Coarse-grained simulations of membranes under tension," *J. Chem. Phys.*, vol. 132, p. 115 101, 2010.

[42] H. S. Muddana, R. R. Gullapalli, E. Manias, and P. J. Butler, "Atomistic simulation of lipid and DiI dynamics in membrane bilayers under tension," *Phys. Chem. Chem. Phys.*, vol. 13, pp. 1368–1378, 2011.

[43] J. Y. Xie, G. H. Ding, and M. Karttunen, "Molecular dynamics simulations of lipid membranes with lateral force: Rupture and dynamic properties," *Biochim. Biophys. Acta*, vol. 1838, pp. 994–1002, 2014.

[44] J. Frauenfeld, J. Gumbart, E. O. van der Sluis, S. Funes, M. Gartmann, B. Beatrix, T. Mielke, O. Berninghausen, T. Becker, K. Schulten, and R. Beckmann, "Cryo-EM structure of the ribosome-SecYE complex in the membrane environment," *Nat. Struct. Mol. Biol.*, vol. 18, pp. 614–621, 2011.

[45] K. R. Pandit and J. B. Klauda, "Membrane models of *E. coli* containing cyclic moieties in the aliphatic lipid chain," *Biochim. Biophys. Acta Biomembr.*, vol. 1818, pp. 1205–1210, 2012.

[46] E. L. Wu, X. Cheng, S. Jo, H. Rui, K. C. Song, E. Dávila-Contreras, Y. Qi, J. Lee, V. Monje-Galvan, R. M. Venable, J. B. Klauda, and W. Im, "CHARMM-GUI membrane builder toward realistic biological membrane simulations," *J. Comput. Chem.*, vol. 35, pp. 1997–2004, 2014.

[47] C. Balusek and J. C. Gumbart, "Role of the native outer-membrane environment on the transporter BtuB," *Biophys. J.*, vol. 111, pp. 1409–1417, 2016.

[48] P. Rassam, N. A. Copeland, O. Birkholz, C. Toth, M. Chavent, A. L. Duncan, S. J. Cross, N. G. Housden, R. Kaminska, U. Seger, D. M. Quinn, T. J. Garrod, M. S. Sansom, J. Piehler, C. G. Baumann, and C. Kleanthous, "Supramolecular assemblies underpin turnover of outer membrane proteins in bacteria," *Nature*, vol. 523, no. 7560, pp. 333–336, 2015.

[49] J. K. Liu, E. J. O'Brien, J. A. Lerman, K. Zengler, B. O. Palsson, and A. M. Feist, "Reconstruction and modeling protein translocation and compartmentalization in *Escherichia coli* at the genome-scale," *BMC Syst. Biol.*, vol. 8, p. 110, 2014.

[50] M. Linden, P. Sens, and R. Phillips, "Entropic tension in crowded membranes," *PLoS Comput. Biol.*, vol. 8, no. 3, e1002431, 2012.

[51] A. D. Dupuy and D. M. Engelman, "Protein area occupancy at the center of the red blood cell membrane," *Proc. Natl. Acad. Sci. U.S.A.*, vol. 105, pp. 2848–2852, 2008.

[52] J. C. Phillips, R. Braun, W. Wang, J. Gumbart, E. Tajkhorshid, E. Villa, C. Chipot, R. D. Skeel, L. Kale, and K. Schulten, "Scalable molecular dynamics with NAMD," *J. Comput. Chem.*, vol. 26, pp. 1781–1802, 2005.

[53] M. J. Abraham, T. Murtola, R. Schulz, S. Páll, J. C. Smith, B. Hess, and E. Lindahl, "GROMACS: High performance molecular simulations through multi-level parallelism from laptops to supercomputers," *SoftwareX*, vol. 1-2, pp. 19–25, 2015.

[54] R. B. Best, J. Mittal, M. Feig, and A. D. MacKerell, Jr., "Inclusion of many-body effects in the additive CHARMM protein CMAP potential results in enhanced cooperativity of α-helix and β-hairpin formation," *Biophys. J.*, vol. 103, pp. 1045–1051, 2012.

[55] S. Nosé, "A unified formulation of the constant temperature molecular dynamics methods," *J. Chem. Phys.*, vol. 81, p. 511, 1984.

[56] Q. Hoover, "Canonical dynamics: Equilibrium phase-space distributions," *Phys. Rev. A*, vol. 31, 16951697, 1985.

[57] S. E. Feller, Y. H. Zhang, R. W. Pastor, and B. R Brooks, "Constant pressure molecular dynamics simulations — The Langevin piston method," *J. Chem. Phys.*, vol. 103, pp. 4613–4621, 1995.

[58] M. Parrinello and A. Rahman, "Polymorphic transitions in single crystals: A new molecular dynamics method," *J. Appl. Phys.*, vol. 52, pp. 721–733, 1981.

[59] T. A. Darden, D. M. York, and L. G. Pedersen, "Particle mesh Ewald: An N log N method for Ewald sums in large systems," *J. Chem. Phys.*, vol. 98, pp. 10 089–10 092, 1993.

[60] W. Humphrey, A. Dalke, and K. Schulten, "VMD – Visual Molecular Dynamics," *J. Mol. Graphics*, vol. 14, pp. 33–38, 1996.

[61] D. Marsh, "Lateral pressure in membranes," *Biochim. Biophys. Acta*, vol. 1286, pp. 183–223, 1996.

[62] K. Murzyn, T. Rog, and M. Pasenkiewicz-Gierula, "Phosphatidylethanolamine-phosphatidylglycerol bilayer as a model of the inner bacterial membrane," *Biophys. J.*, vol. 88, pp. 1091–1103, 2005.

[63] S. E. Feller and R. W. Pastor, "Constant surface tension simulations of lipid bilayers: The sensitivity of surface areas and compressibilities," *J. Chem. Phys.*, vol. 111, pp. 1281–1287, 1999.

[64] E. Lindahl and O. Edholm, "Spatial and energetic-entropic decomposition of surface tension in lipid bilayers from molecular dynamics simulations," *J. Chem. Phys.*, vol. 113, pp. 3882–3893, 2000.

[65] M. D Tomasini, C. Rinaldi, and M. S. Tomassone, "Molecular dynamics simulations of rupture in lipid bilayers," *Exp. Biol. Med*, vol. 235, pp. 181–188, 2010.

[66] C. Storm, J. J. Pastore, F. C. MacKintosh, T. C. Lubensky, and P. A. Janmey, "Nonlinear elasticity in biological gels," *Nature*, vol. 435, pp. 191–194, 2005.

[67] K. A. Erk, K. J. Henderson, and K. R. Shull, "Strain stiffening in synthetic and biopolymer networks," *Biomacromolecules*, vol. 11, pp. 1358–1363, 2010.

[68] T. J. Piggot, D. A. Holdbrook, and S. Khalid, "Electroporation of the *E. coli* and *S. aureus* membranes: Molecular dynamics simulations of complex bacterial membranes," *J. Phys. Chem. B*, vol. 115, pp. 13 381–13 388, 2011.

[69] C. Hong, D. P. Tieleman, and Y. Wang, "Microsecond molecular dynamics simulations of lipid mixing," *Langmuir*, vol. 30, pp. 11 993–2001, 2014.

[70] J. H. Borrell and O. Doménech, "Critical temperature of 1-palmitoyl-2-oleoyl-*sn*-glycero-3-phosphoethanolamine monolayers and its possible biological relevance," *J. Phys. Chem. B*, vol. 121, pp. 6882–6889, 2017.

[71] S. Baoukina, L. Monticelli, S. J. Marrink, and D. P. Tieleman, "Pressure-area isotherm of a lipid monolayer from molecular dynamics simulations," *Langmuir*, vol. 23, pp. 12 617–12 623, 2007.

[72] M. Herrmann, E. Schneck, T. Gutsmann, K. Brandenburg, and M. Tanaka, "Bacterial lipopolysaccharides form physically cross-linked, two-dimensional gels in the presence of divalent cations," *Soft Mat.*, vol. 11, pp. 6037–6044, 2015.

[73] E. Schneck, T. Schubert, O. V. Konovalov, B. E. Quinn, T. Gutsmann, K. Brandenburg, R. G. Oliveira, D. A. Pink, and M. Tanaka, "Quantitative determination of ion distributions in bacterial lipopolysaccharide membranes by grazing-incidence X-ray fluorescence," *Proc. Natl. Acad. Sci. U.S.A.*, vol. 107, pp. 9147–9151, 2010.

[74] J. V. Höltje, "Growth of the stress-bearing and shape-maintaining murein sacculus of *Escherichia coli*," *Microbiol. Mol. Biol. Rev.*, vol. 62, pp. 181–203, 1998.

[75] X. Yao, M. Jericho, D. Pink, and T. Beveridge, "Thickness and elasticity of Gram-negative murein sacculi measured by atomic force microscopy," *J. Bacteriol.*, vol. 181, pp. 6865–6875, 1999.

[76] R. D. Turner, S. Mesnage, J. K. Hobbs, and S. J. Foster, "Molecular imaging of glycan chains couples cell-wall polysaccharide architecture to bacterial cell morphology," *Nat. Commun.*, vol. 9, p. 1263, 2018.

[77] M. L. Gardel, J. H. Shin, F. C. MacKintosh, L. Mahadevan, P. Matsudaira, and D. A. Weitz, "Elastic behavior of cross-linked and bundled actin networks," *Science*, vol. 304, pp. 1301–1305, 2004.

[78] A. L. Koch and S. Woeste, "Elasticity of the sacculus of *Escherichia coli*," *J. Bacteriol.*, vol. 174, pp. 4811–4819, 1992.

[79] T. Pilizota and J. W. Shaevitz, "Fast, multiphase volume adaptation to hyperosmotic shock by *Escherichia coli*," *PLoS One*, vol. 7, e35205, 2012.

[80] S. B. Zimmerman and S. O. Trach, "Estimation of macromolecule concentrations and excluded volume effects for the cytoplasm of *Escherichia coli*," *J. Mol. Biol.*, vol. 222, pp. 599–620, 1991.

[81] R. J. Ellis, "Macromolecular crowding: Obvious but underappreciated," *Trends Biochem. Sci.*, vol. 26, p. 2001, 597–604.

[82] J. P. Michel, Y. X. Wang, I. Kiesel, Y. Gerelli, and V. Rosilio, "Disruption of asymmetric lipid bilayer models mimicking the outer membrane of Gram-negative bacteria by an active plasticin," *Langmuir*, vol. 33, pp. 11 028–11 039, 2017.

[83] T. Abraham, S. R. Schooling, T. J. Beveridge, and J. Katsaras, "Monolayer film behavior of lipopolysaccharide from *Pseudomonas aeruginosa* at the air-water interface," *Biomacromolecules*, vol. 9, pp. 2799–2804, 2008.

[84] A. P. Le Brun, L. A. Clifton, C. E. Halbert, B. Lin, M. Meron, P. J. Holden, J. H. Lakey, and S. A. Holt, "Structural characterization of a model gram-negative bacterial surface using lipopolysaccharides from rough strains of *Escherichia coli*," *Biomacromolecules*, vol. 14, pp. 2014–2022, 2013.

[85] P. W. Fowler, J. Hélie, A. Duncan, M Chavent, H. Kolds, and M. S. P. Sansom, "Membrane stiffness is modified by integral membrane proteins," *Soft Mat.*, vol. 12, pp. 7792–7803, 2016.

[86] W. Arunmanee, M. Pathania, A. S. Solovyova, A. P. Le Brun, H. Ridley, A. Baslé, B. van den Berg, and J. H. Lakey, "Gram-negative trimeric porins have specific LPS binding sites that are essential for porin biogenesis," *Proc. Natl. Acad. Sci. USA*, vol. 113, pp. 5034–5043, 2016.

[87] H. H. Tuson, G. K. Auer, L. D. Renner, M. Hasebe, C. Tropini, M. Salick, W. C. Crone, A. Gopinathan, K. C. Huang, and D. B. Weibel, "Measuring the stiffness of bacterial cells from growth rates in hydrogels of tunable elasticity," *Mol. Microbiol.*, vol. 84, pp. 874–891, 2012.

[88] R. Buda, Y. Liu, J. Yang, S. Hegde, K. Stevenson, F. Bai, and T. Pilizota, "Dynamics of *Escherichia coli*'s passive response to a sudden decrease in external osmolarity," *Proc. Natl. Acad. Sci. USA*, vol. 113, pp. 5838–5846, 2016.

[89] Š. Baláž, "Lipophilicity in trans-bilayer transport and subcellular pharmacokinetics," *Persp. Drug Disc. Des.*, vol. 19, no. 1, pp. 157–177, 2000.

[90] M. Kansy, F. Senner, and K. Gubernator, "Physicochemical high throughput screening: Parallel artificial membrane permeation assay in the description of passive absorption processes," *J. Med. Chem.*, vol. 41, no. 7, pp. 1007–1010, 1998.

[91] A. Avdeef, S. Bendels, L. Di, B. Faller, M. Kansy, K. Sugano, and Y. Yamauchi, "PAMPA–critical factors for better predictions of absorption," *J. Pharm. Sci.*, vol. 96, pp. 2893–2909, 2007.

[92] P. Artursson, K. Palm, and K. Luthman, "Caco-2 monolayers in experimental and theoretical predictions of drug transport," *Adv. Drug Deliv. Rev.*, vol. 46, 27–ł43, 2001.

[93] R. B. van Breemen and Y. Li, "Caco-2 cell permeability assays to measure drug absorption," *Expert Opin. Drug Metab. Toxicol.*, vol. 1, no. 2, pp. 175–185, 2005.

[94] J. D. Irvine, L. Takahashi, K. Lockhart, J. Cheong, J. W. Tolan, H. E. Selick, and J. R. Grove, "MDCK (Madin-Darby canine kidney) cells: A tool for membrane permeability screening," *J. Pharm. Sci.*, vol. 88, pp. 28–33, 1999.

[95] C. Hansch, "Quantitative approach to biochemical structure-activity relationships," *Acc. Chem. Res.*, vol. 2, no. 8, pp. 232–239, 1969.

[96] T. R. Stouch, J. R. Kenyon, S. R. Johnson, X.-Q. Chen, A. Doweyko, and Y. Li, "In silico ADME/Tox: Why models fail," *J. Comp.-Aided Mol. Design*, vol. 17, no. 2–4, pp. 83–92, 2003.

[97] R. V. Swift and R. E. Amaro, "Back to the future: Can physical models of passive membrane permeability help reduce drug candidate attrition and move us beyond QSPR?" *Chem. Biol. Drug Des.*, vol. 81, no. 1, pp. 61–71, 2013.

[98] L. Zhang, J. Tan, D. Han, and H. Zhu, "From machine learning to deep learning: Progress in machine intelligence for rational drug discovery," *Drug Discov. Today*, vol. 22, no. 11, pp. 1680–1685, 2017.

[99] A. Finkelstein and A. Cass, "Permeability and electrical properties of thin lipid membranes," *J. Gen. Physiol.*, vol. 52, pp. 145–172, 1968.

[100] J. M. Diamond and Y. Katz, "Interpretation of nonelectrolyte partition coefficients between dimyristoyl lecithin and water," *J. Mol. Biol.*, vol. 96, pp. 121–154, 1974.

[101] G. M. Torrie and J. P. Valleau, "Nonphysical sampling distributions in monte carlo free-energy estimation: Umbrella sampling," *J. Comput. Phys.*, vol. 23, no. 2, pp. 187–199, 1997.

[102] E. Darve, D. Rodríguez-Gómez, and A. Pohorille., "Adaptive biasing force method for scalar and vector free energy calculations.," *J. Chem. Phys.*, vol. 128, no. 14, p. 144 120, 2008.

[103] J. Hénin, G. Fiorin, C. Chipot, and M. L. Klein, "Exploring multidimensional free energy landscapes using time-dependent biases on collective variables," *J. Chem. Theory Comput.*, vol. 6, no. 1, pp. 35–47, 2010.

[104] A. Laio and M. Parrinello, "Escaping free-energy minima," *Proc. Natl. Acad. Sci. USA*, vol. 99, no. 20, pp. 12 562–11 256, 2002.

[105] C. T. Lee, J. Comer, C. Herndon, N. Leung, A. Pavlova, R. V. Swift, C. Tung, C. N. Rowley, R. E. Amaro, C. Chipot, Y. Wang, and J. C. Gumbart, "Simulation-based approaches for determining membrane permeability of small compounds," *J. Chem. Inf. Model.*, vol. 56, no. 4, pp. 721–733, 2016.

[106] E. Awoonor-Williams and C. N.Rowley, "Molecular simulation of nonfacilitated membrane permeation," *Biochim. Biophys. Acta Biomembr.*, vol. 1858, no. 7, pp. 1672–1687, 2016.

[107] T. W. Keenan and D. J. Morre, "Phospholipid class and fatty acid composition of golgi apparatus isolated from rat liver and comparison with other cell fractions," *J. Biol. Chem.*, vol. 9, pp. 19–25, 1970.

[108] R. C. Pfleger, N. G. Anderson, and F. Snyder, "Lipid class and fatty acid composition of rat liver plasma membranes isolated by zonal centrifugation," *Biochemistry*, vol. 7, no. 8, pp. 2826–2833, 1968.

[109] M. V. Varma, I. Gardner, S. J. Steyn, P. Nkansah, C. J. Rotter, C. Whitney-Pickett, H. Zhang, L. Di, M. Cram, K. S. Fenner, and A. F. El-Kattan, "PH-Dependent solubility and permeability criteria for provisional biopharmaceutics classification (BCS and BDDCS) in early drug discovery.," *Mol. Pharmacol.*, vol. 9, no. 5, pp. 1199–1212, 2012.

[110] F. Lombardo, M. Y. Shalaeva, K. A. Tupper, and F. Gao, "Elog$Doct$: A tool for lipophilicity determination in drug discovery. 2. Basic and neutral compounds," *J. Med. Chem.*, vol. 44, no. 15, pp. 2490–2497, 2001.

[111] A. Avdeef, "Absorption and drug development: Solubility, permeability, and charge state," *John Wiley Sons, Inc.*, vol. New Jersey, 2012.

[112] J. C. Owicki and H. M. McConnell, "Theory of protein-lipid and protein-protein interactions in bilayer.," *Proc. Natl. Acad. Sci. USA*, vol. 76, no. 10, pp. 4750–4754, 1979.

[113] K. Fricke, K. Wirthensohn, R. Laxhuber, and E. Sackmann, "Flicker spectroscopy of erythrocytes. A sensitive method to study subtle changes of membrane bending stiffness," *Eur. Biophys. J.*, vol. 14, pp. 67–81, 1986.

[114] E. A. Evans and R. Skalak, "Mechanics and thermodynamics of biomembranes: Part 1," *CRC Crit. Rev. Bioeng*, vol. 3, pp. 181–330, 1979.

[115] L. J. Lis, M. McAlister, N. Fuller, and R. P. Rand, "Measurement of the lateral compressibility of several phospholipid bilayers," *Biophys. J.*, vol. 37, pp. 667–672, 1982.

[116] J. R. Elliott, D. Needham, J. P. Dilger, O. Brandt, and D. A. Haydon, "A quantitative explanation of the effects of some alcohols on gramicidin single-channel lifetime," *Biochim. Biophys. Acta*, vol. 814, pp. 401–404, 1983.

[117] W. Helfrich, "Elastic properties of lipid bilayers: Theory and possible experiments," *Phys. Rev. Lett.*, vol. 97, pp. 693–703, 1973.

[118] E. Evans, "Bending resistance and chemically induced moments in membrane bilayers.," *Biophys. J.*, vol. 14, pp. 923–931, 1974.

[119] H. Huang, "Deformation free energy of bilayer membrane and its effect on gramicidin channel lifetime," *Biophys. J.*, vol. 50, pp. 1061–1070, 1986.

[120] C. Nielsen, M. Goulian, and O. Andersen, "Energetics of inclusion-induced bilayer deformations," *Biophys. J.*, vol. 74, pp. 1966–1983, 1998.

[121] J. Lundbæk, P. Birn, J. Girshman, A. Hansen, and O. Andersen, "Membrane stiffness and channel function," *Biochemistry*, vol. 35, pp. 3825–3830, 1996.

[122] M. Goulian, O. Mesquita, D. Fygenson, C. Nielsen, O. Andersen, and A. Libshaber, "Gramicidin channel kinetics under tension.," *Biophys. J.*, vol. 74, pp. 328–337, 1998.

[123] N. Dan, A. Berman, P. Pincus, and S. Safran, "Membrane-induced interactions between inclusions," *J. Phys. II (Fr.)*, vol. 4, pp. 1713–1725, 1994.

[124] N. Dan and S. Safran, "Effect of lipid characteristics on the structure of transmembrane proteins," *Biophys. J.*, vol. 75, pp. 1410–1414, 1998.

[125] K. Vanommeslaeghe and A. D. M. Jr., "Automation of the CHARMM general force field (CGenFF) I: Bond perception and atom typing," *J. Chem. Inf. Model.*, vol. 52, no. 12, pp. 3144–3154, 2012.

[126] K. Vanommeslaeghe, E. P. Raman, and A. D. M. Jr., "Automation of the CHARMM general force field (CGenFF) II: Assignment of bonded parameters and partial atomic charges," *J. Chem. Inf. Model.*, vol. 52, no. 12, pp. 3155–3168, 2012.

[127] R. B. Best, X. Zhu, J. Shim, P. E. Lopes, J. Mittal, M. Feig, and A. D. MacKerell Jr., "Optimization of the additive CHARMM all-atom protein force field targeting improved sampling of the backbone ϕ, ψ and side-chain χ_1 and χ_2 dihedral angles," *J. Chem. Theory Comput.*, vol. 8, pp. 3257–3273, 2012.

[128] X. Jin, T. Luong, N. Reese, H. Gaona, V. Collazo-Velez, C. Vuong, B. Potter, J. C. Sousa, R. Olmeda, Q. Li, L. Xie, J. Zhang, P. Zhang, G. Reichard, V. Melendez, S. R. Marcsisin, and B. S. Pybus, "Comparison of MDCK-MDR1 and Caco-2 cell based permeability assays for anti-malarial drug screening and drug investigations," vol. 70, no. 2, pp. 188–194, 2014.

[129] J. Lombard, "Once upon a time the cell membranes: 175 years of cell boundary research," *Biol. Direct*, vol. 9, p. 32, 2014.

[130] N. Kuerka, B. van Oosten, J. Pan, F. A. Heberle, T. A. Harroun, and J. Katsaras, "Molecular Structures of Fluid Phosphatidylethanolamine Bilayers Obtained from Simulation-to-Experiment Comparisons and Experimental Scattering Density Profiles," *J. Phys. Chem. B*, vol. 119, pp. 1947–1956, 2015.

[131] X. Zhuang, J. R. Makover, W. Im, and J. B. Klauda, "A systematic molecular dynamics simulation study of temperature dependent bilayer structural properties," *Biochim. Biophys. Acta Biomembr.*, vol. 1838, pp. 2520–2529, 2014.

[132] A. Botan, F. Favela-Rosales, P. F. J. Fuchs, M. Javanainen, M. Kandu, W. Kulig, A. Lamberg, C. Loison, A. Lyubartsev, M. S. Miettinen, L. Monticelli, J. Mtt, O. H. S. Ollila, M. Retegan, T. Rg, H. Santuz, and J. Tynkkynen, "Toward atomistic resolution structure of phosphatidylcholine headgroup and glycerol backbone at different ambient conditions," *J. Phys. Chem. B*, vol. 119, pp. 15 075–15 088, 2015.

[133] X. Zhuang, E. M. Dvila-Contreras, A. H. Beaven, W. Im, and J. B. Klauda, "An extensive simulation study of lipid bilayer properties with different head groups, acyl chain lengths, and chain saturations," *Biochim. Biophys. Acta Biomembr.*, vol. 1858, pp. 3093–3104, 2016.

[134] K. Pluhackova, S. A. Kirsch, J. Han, L. Sun, Z. Jiang, T. Unruh, and R. A. Bckmann, "A Critical Comparison of Biomembrane Force Fields: Structure and Dynamics of Model DMPC, POPC, and POPE Bilayers," *J. Phys. Chem. B*, vol. 120, pp. 3888–3903, 2016.

[135] M. Doktorova, D. Harries, and G. Khelashvili, "Determination of bending rigidity and tilt modulus of lipid membranes from real-space fluctuation analysis of molecular dynamics simulations," *Phys. Chem. Chem. Phys.*, vol. 19, pp. 16 806–16 818, 2017.

[136] C. Kandt, W. L. Ash, and D. Peter Tieleman, "Setting up and running molecular dynamics simulations of membrane proteins," *Methods*, vol. 41, pp. 475–488, 2007.

[137] E. Lindahl and M. S. P. Sansom, "Membrane proteins: Molecular dynamics simulations," *Curr. Opin. Struct. Biol.*, vol. 18, pp. 425–431, 2008.

[138] M. Chavent, A. L. Duncan, and M. S. Sansom, "Molecular dynamics simulations of membrane proteins and their interactions: From nanoscale to mesoscale," *Curr. Opin. Struct. Biol.*, vol. 40, pp. 8–16, 2016.

[139] A. P. Lyubartsev and A. L. Rabinovich, "Force field development for lipid membrane simulations," *Biochim. Biophys. Acta Biomembr.*, vol. 1858, pp. 2483–2497, 2016.

[140] D. Poger, B. Caron, and A. E. Mark, "Validating lipid force fields against experimental data: Progress, challenges and perspectives," *Biochim. Biophys. Acta Biomembr.*, vol. 1858, pp. 1556–1565, 2016.

[141] C. J. Dickson, B. D. Madej, Å. A. Skjevik, R. M. Betz, K. Teigen, I. R. Gould, and R. C. Walker, "Lipid14: The AMBER lipid force field," *J. Chem. Theory Comput.*, vol. 10, pp. 865–879, 2014.

[142] J. P. M. Jambeck and A. P. Lyubartsev, "An extension and further validation of an all-atomistic force field for biological membranes," *J. Chem. Theory Comput.*, vol. 8, pp. 2938–2948, 2012.

[143] A. Kukol, "Lipid models for united-atom molecular dynamics simulations of proteins," *J. Chem. Theory Comput.*, vol. 5, pp. 615–626, 2009.

[144] N. Schmid, A. P. Eichenberger, A. Choutko, S. Riniker, M. Winger, A. E. Mark, and W. F. van Gunsteren, "Definition and testing of the GROMOS force-field versions 54A7 and 54B7," *Eur. Biophys. J.*, vol. 40, pp. 843–856, 2011.

[145] D. Poger and A. E. Mark, "Lipid bilayers: The effect of force field on ordering and dynamics," *J. Chem. Theory Comput.*, vol. 8, pp. 4807–4817, 2012.

[146] Y. Wang, T. Zhao, D. Wei, E. Strandberg, A. S. Ulrich, and J. P. Ulmschneider, "How reliable are molecular dynamics simulations of membrane active antimicrobial peptides?" *Biochim. Biophys. Acta Biomembr.*, vol. 1838, pp. 2280–2288, 2014.

[147] K. Vanommeslaeghe, E. Hatcher, C. Acharya, S. Kundu, S. Zhong, J. Shim, E. Darian, O. Guvench, P. Lopes, I. Vorobyov, and A. D. MacKerell Jr., "CHARMM general force field: A force field for drug-like molecules compatible with the CHARMM all-atom additive biological force fields," *J. Comput. Chem.*, vol. 31, pp. 671–690, 2010.

[148] S. Jo, T. Kim, V. G. Iyer, and W. Im, "CHARMM-GUI: A web-based graphical user interface for CHARMM," *J. Comput. Chem.*, vol. 29, pp. 1859–1865, 2008.

[149] S. Jo, J. B. Lim, J. B. Klauda, and W. Im, "CHARMM-GUI membrane builder for mixed bilayers and its application to yeast membranes," *Biophys. J.*, vol. 97, no. 1, pp. 50–58, 2009.

[150] J. Lee, X. Cheng, J. M. Swails, M. S. Yeom, P. K. Eastman, J. A. Lemkul, S. Wei, J. Buckner, J. C. Jeong, Y. Qi, S. Jo, V. S. Pande, D. A. Case, C. L. Brooks, A. D. MacKerell, J. B. Klauda, and W. Im, "CHARMM-GUI input generator for NAMD, GROMACS, AMBER, OpenMM, and CHARMM/OpenMM simulations using the charmm36 additive force field," *J. Chem. Theory Comput.*, vol. 12, pp. 405–413, 2016.

[151] T. Romo and A. Grossfield, "Loos: An extensible platform for the structural analysis of simulations," *31st Annual International Conference of the IEEE EMBS*, pp. 2332–2335, 2009.

[152] T. D. Romo, N. Leioatts, and A. Grossfield, "Lightweight object oriented structure analysis: Tools for building tools to analyze molecular dynamics simulations," *J. Comp. Chem.*, vol. 35, pp. 2305–2318, 2014.

[153] Y. Wang, C. B. Harrison, K. Schulten, and J. A. McCammon, "Implementation of accelerated molecular dynamics in NAMD," *Comput. Sci. Discov.*, vol. 4:015002, 2011, (11 pages).

[154] K. A. Feenstra, B. Hess, and H. J. C. Berendsen, "Improving efficiency of large time-scale molecular dynamics simulations of hydrogen-rich systems," *J. Comput. Chem.*, vol. 20, pp. 786–798, 1999.

[155] C. W. Hopkins, S. Le Grand, R. C. Walker, and A. E. Roitberg, "Long-time-step molecular dynamics through hydrogen mass repartitioning," *J. Chem. Theory Comput.*, vol. 11, pp. 1864–1874, 2015.

[156] R. Francesco and S. Martin, "Thermodynamics and kinetics of largetimestep molecular dynamics," *J. Comput. Chem.*, vol. 33, pp. 475–483, 2012.

[157] J.-P. Ryckaert, G. Ciccotti, and H. J. C. Berendsen, "Numerical integration of the cartesian equations of motion of a system with constraints: Molecular dynamics of n-alkanes," *J. Comput. Phys.*, vol. 23, pp. 327–341, 1977.

[158] S. Miyamoto and P. A. Kollman, "Settle: An analytical version of the SHAKE and RATTLE algorithm for rigid water models," *J. Comput. Chem.*, vol. 13, pp. 952–962, 1992.

[159] B. Loubet, W. Kopec, and H. Khandelia, "Accelerating All-Atom MD Simulations of Lipids Using a Modified Virtual-Sites Technique," *J. Chem. Theory Comput.*, vol. 10, pp. 5690–5695, 2014.

[160] P. Bjelkmar, P. Larsson, M. A. Cuendet, B. Hess, and E. Lindahl, "Implementation of the CHARMM force field in GROMACS: Analysis of protein stability effects from correction maps, virtual interaction sites, and water models," *J. Chem. Theory Comput.*, vol. 6, pp. 459–466, 2010.

[161] K. Olesen, N. Awasthi, D. S. Bruhn, W. Pezeshkian, and H. Khandelia, "Faster simulations with a 5 fs time step for lipids in the charmm force field," *J. Chem. Theory Comput.*, vol. 14, pp. 3342–3350, 2018.

[162] D. Case, R. Betz, D. Cerutti, T. Cheatham, III, T. Darden, R. Duke, T. Giese, H. Gohlke, A. Goetz, N. Homeyer, S. Izadi, P. Janowski, J. Kaus, A. Kovalenko, T. Lee, S. LeGrand, P. Li, C. Lin, T. Luchko, R. Luo, B. Madej, D. Mermelstein, K. Merz, G. Monard, H. Nguyen, H. Nguyen, I. Omelyan, A. Onufriev, D. R. Roe, A. Roitberg, C. Sagui, C. Simmerling, W. Botello-Smith, J. Swails, R. Walker, J. Wang, R. Wolf, X. Wu, L. Xiao, and P. Kollman, *AMBER 2016*. University of California, San Francisco, 2016.

[163] M. J. Harvey, G. Giupponi, and G. D. Fabritiis, "ACEMD: Accelerating biomolecular dynamics in the microsecond time scale," *J. Chem. Theory Comput.*, vol. 5, pp. 1632–1639, 2009.

[164] A. A. Petruk, S. Varriale, M. R. Coscia, L. Mazzarella, A. Merlino, and U. Oreste, "The structure of the CD3 $\zeta\zeta$ transmembrane dimer in POPC and raft-like lipid bilayer: A molecular dynamics study," *Biochim. Biophys. Acta Biomembr.*, vol. 1828, pp. 2637–2645, 2013.

[165] X. Liu, S. Ahn, A. W. Kahsai, K.-C. Meng, N. R. Latorraca, B. Pani, A. J. Venkatakrishnan, A. Masoudi, W. I. Weis, R. O. Dror, X. Chen, R. J. Lefkowitz, and B. K. Kobilka, "Mechanism of intracellular allosteric β_2AR antagonist revealed by X-ray crystal structure," *Nature*, vol. 548, pp. 480–484, 2017.

[166] D. Wacker, S. Wang, J. D. McCorvy, R. M. Betz, A. J. Venkatakrishnan, A. Levit, K. Lansu, Z. L. Schools, T. Che, D. E. Nichols, B. K. Shoichet, R. O. Dror, and B. L. Roth, "Crystal structure of an LSD-bound human serotonin receptor," *Cell*, vol. 168, 377–389.e12, 2017.

[167] A. R. Braun, E. G. Brandt, O. Edholm, J. F. Nagle, and J. N. Sachs, "Determination of electron density profiles and area from simulations of undulating membranes," *Biophys. J.*, vol. 100, no. 9, pp. 2112–2120, 2011.

[168] A. Kohlmeyer and J. Vermaas, *Akohlmey/topotools: Release 1.7*, Apr. 2017.

[169] H. Martinez-Seara and T. Róg, *Biomolecular Simulations. Methods in Molecular Biology, Methods and Protocols*. Humana Press, 2013, vol. 924, ch. Molecular Dynamics Simulations of Lipid Bilayers: Simple Recipe of How to Do It.

[170] N. Michaud-Agrawal, E. J. Denning, T. B. Woolf, and O. Beckstein, "Mdanalysis: A toolkit for the analysis of molecular dynamics simulations," *J. Comput. Chem.*, vol. 32, no. 10, pp. 2319–2327, 2011.

[171] J. C. Gumbart, M. B. Ulmschneider, A. Hazel, S. H. White, and J. P. Ulmschneider, "Computed free energies of peptide insertion into bilayers are independent of computational method," *J. Membr. Biol.*, vol. 251, no. 3, pp. 345–356, 2018.

[172] C. Hong, D. P. Tieleman, and Y. Wang, "Microsecond molecular dynamics simulations of lipid mixing," *Langmuir*, vol. 30, no. 40, pp. 11 993–12 001, 2014.

[173] A. Grossfield and D. M. Zuckerman, "Quantifying uncertainty and sampling quality in biomolecular simulations," vol. 5, pp. 23–48, 2009.

[174] E. Yamashita, M. V. Zhalnina, S. D. Zakharov, O. Sharma, and W. A. Cramer, "Crystal structures of the OmpF porin: function in a colicin translocon," *EMBO J.*, vol. 27, no. 15, pp. 2171–2180, 2008.

[175] S. Pezeshki, C. Chimerel, A. N. Bessonov, M. Winterhalter, and U. Kleinekathofer, "Understanding ion conductance on a molecular level: an all-atom modeling of the bacterial porin OmpF," *Biophys. J.*, vol. 97, no. 7, pp. 1898–1906, 2009.

[176] P. S. Crozier, D. Henderson, R. L. Rowley, and D. D. Busath, "Model channel ion currents in NaCl-extended simple point charge water solution with applied-field molecular dynamics," *Biophys. J.*, vol. 81, no. 6, pp. 3077–3089, 2001.

[177] A. Aksimentiev and K. Schulten, "Imaging alpha-hemolysin with molecular dynamics: ionic conductance, osmotic permeability, and the electrostatic potential map," *Biophys. J.*, vol. 88, no. 6, pp. 3745–3761, 2005.

[178] R. W. Benz, F. Castro-Román, D. J. Tobias, and S. H. White, "Experimental validation of molecular dynamics simulations of lipid bilayers: A new approach," *Biophys. J.*, vol. 88, no. 2, pp. 805–817, 2005.

[179] H. I. Petrache, S. W. Dodd, and M. F. Brown, "Area per lipid and acyl length distributions in fluid phosphatidylcholines determined by 2H NMR spectroscopy," *Biophys. J.*, vol. 79, no. 6, pp. 3172–3192, 2000.

[180] N. Kučerka, S. Tristram-Nagle, and J. F. Nagle, "Closer look at structure of fully hydrated fluid phase DPPC bilayers," *Biophys. J.*, vol. 90, no. 11, pp. L83–L85, 2006.

[181] N. Kučerka, M. P. Nieh, and J. Katsaras, "Fluid phase lipid areas and bilayer thicknesses of commonly used phosphatidylcholines as a function of temperature," *Biochim. Biophys. Acta Biomembr.*, vol. 1808, pp. 2761–2771, 11 2011.

[182] E. Egberts, S. Marrink, and H. J. C. Berendsen, "Molecular dynamics simulation of a phospholipid membrane," pp. 423–436, 22 1994.

[183] J. Wohlert, W. K. den Otter, O. Edholm, and W. J. Briels, "Free energy of a transmembrane pore calculated from atomistic molecular dynamics simulations," *J. Chem. Phys.*, vol. 124, p. 154 905, 2006.

[184] L. S. Vermeer, B. L. de Groot, V. Réat, A. Milon, and J. Czaplicki, "Acyl chain order parameter profiles in phospholipid bilayers: Computation from molecular dynamics simulations and comparison with ^{2}H NMR experiments," *Eur. Biophys. J.*, vol. 36, pp. 919–931, 2007.

[185] M. Camley B.A. Lerner, R. Pastor, and F. Brown, "Strong influence of periodic boundary conditions on lateral diffusion in lipid bilayer membranes.," *J. Chem. Phys.*, vol. 143, p. 243 113, 24 2015.

[186] R. M. Venable, H. I. Inglfsson, M. G. Lerner, B. S. Perrin, B. A. C. Jr., S. J. Marrink, F. L. H. Brown, and R. W. Pastor, "Lipid and peptide diffusion in bilayers: The saffmandelbrck model and periodic boundary conditions," *JPCB*, vol. 121, no. 15, pp. 3443–3457, 2017.

[187] G. Orädd, P. W. Westerman, and G. Lindblom, "Lateral diffusion coefficients of separate lipid species in a ternary raft-forming bilayer: A pfg-nmr multinuclear study," *Biophys. J.*, vol. 89, pp. 315–320, 2005.

[188] G. Lindblom and G. Orädd, "Lipid lateral diffusion and membrane heterogeneity.," *BBA*, vol. 1788, no. 1, pp. 234–244, 2009.

[189] N. Kučerka, J. F. Nagle, J. N. Sachs, S. E. Feller, J. Pencer, A. Jackson, and J. Katsaras, "Lipid bilayer structure determined by the simultaneous analysis of neutron and x-ray scattering data," *Biophys. J.*, vol. 95, no. 5, 2356–2367, 2008.

[190] M. Rappolt, A. Hickel, F. Bringezu, and K. A. Lohner, "Mechanism of the lamellar/inverse hexagonal phase transition examined by high resolution x-ray diffraction," *Biophys. J.*, vol. 84, no. 5, pp. 3111–3122, 2003.

[191] R. P. Rand and V. A. Parsegian, "Hydration forces between phospholipid bilayers," vol. 988, no. 3, pp. 351–376, 1989.

[192] N. Kučerka, S. Tristram-Nagle, and J. F. Nagle, "Structure of fully hydrated fluid phase lipid bilayers with monounsaturated chains," *J. Membr. Biol.*, vol. 208, no. 3, pp. 193–202, 2005.

[193] F. Heinemann, V. Betaneli, F. A. Thomas, and P. Schwille, "Quantifying lipid lateral diffusion by fluorescence correlation spectroscopy: A critical treatise," *Langmuir*, vol. 28, no. 37, pp. 13 395–13 404, 2012.

[194] H. Hwang, N. Paracinic, J. M.Parks, J. H.Lakey, and J. C.Gumbart, "Distribution of mechanical stress in the escherichia coli cell envelope," *Biophys. J.*, vol. 1860, no. 12, pp. 2566–2575, 2018.

[195] W. D. Bennett, C. K. Hong, Y. Wang, and D. P. Tieleman, "Antimicrobial peptide simulations and the influence of force field on t he free energy for pore formation in lipid bilayers," *J. Chem. Theory Comput.*, vol. 12, no. 9, pp. 4524–4533, 2016.

[196] D. Marsh, "Elastic curvature constants of lipid monolayers and bilayers," *Chem. Phys. Lett.*, vol. 144, no. 2, pp. 146–159, 2006.

[197] S. W. Cowan, R. M. Garavito, J. N. Jansonius, J. A. Jenkins, R. Karlsson, N. Konig, E. F. Pai, R. A. Pauptit, P. J. Rizkallah, and J. P. Rosenbusch, "The structure of OmpF porin in a tetragonal crystal form," *Structure*, vol. 3, no. 10, pp. 1041–1050, 1995.

[198] M. Watanabe, J. Rosenbusch, T. Schirmer, and M. Karplus, "Computer simulations of the OmpF porin from the outer membrane of *Escherichia coli*," *Biophys. J.*, vol. 72, pp. 2094–2102, 1997.

[199] N. R. Latorraca, A. J. Venkatakrishnan, and R. O. Dror, "Gpcr dynamics: Structures in motion," *Chemical Reviews*, vol. 117, pp. 139–155, 2017.

[200] D. P. Hurst, A. Grossfield, D. L. Lynch, S. Feller, T. D. Romo, K. Gawrisch, M. C. Pitman, and P. H. Reggio, "A lipid pathway for ligand binding is necessary for a cannabinoid g protein-coupled receptor," *J. Biol. Chem.*, vol. 285, pp. 17 954–17 964, 2010.

[201] C. L. Wennberg, T. Murtola, B. Hess, and E. Lindahl, "Lennard-Jones lattice summation in bilayer simulations has critical effects on surface tension and lipid properties," *J. Chem. Theory Comput.*, vol. 9, 3527–3537, 2013.

[202] A. N. Leonard, R. W. Pastor, and J. B. Klauda, "Parameterization of the CHARMM all-atom force field for ether lipids and model linear ethers," *J. Phys. Chem. B*, vol. 122, 6744–6754, 2018.

[203] H. Li, J. Chowdhary, L. Huang, X. He, A. D. MacKerell, and B. Roux, "Drude Polarizable Force Field for Molecular Dynamics Simulations of Saturated and Unsaturated Zwitterionic Lipids," *J. Chem. Theory Comput.*, vol. 13, pp. 4535–4552, 2017.

[204] A. N. Leonard, A. C. Simmonett, F. C. Pickard IV, J. Huang, R. M. Venable, J. B. Klauda, B. R. Brooks, and R. W. Pastor, "Comparison of additive and polarizable models with explicit treatment of long-range lennard-jones interactions using alkane simulations," *J. Chem. Theory Comput.*, vol. 14, pp. 948–958, 2018.

[205] L. Picas, F. Rico, and S. Scheuring, "Direct measurement of the mechanical properties of lipid phases in supported bilayers," *Biophys. J.*, vol. 102, pp. L01–L03, 2012.

VITA

Hyea Hwang was born in 1986 in South Korea to parents Gyueob Hwang and Joohee Hong. She attended the Georgia Institute of Technology from 2009 to 2013 and graduated with a B.S. in Chemical and Biomolecular Engineering. There, she studied simulated moving bed (SMB) chromatographic separation, and she graduated with highest honors. In 2014, she came to the Materials Science and Engineering department at the Georgia Institute of Technology for its Ph.D program. She pursued computational biophysics research under the guidance of Professor James Gumbart. In 2017, she earned a Science Graduate Student Research (SCGSR) fellowship from the Dept. of Energy, after which she worked at Oak Ridge National Lab for 9 months under the mentorship of Dr. Jerry Parks.

Journal articles

Distribution of mechanical stress in the *Escherichia coli* cell envelope. H. Hwang, N. Paracini, J. M. Parks, J. H. Lakey, and J. C. Gumbart. *Biochimica et Biophysica Acta (BBA) Biomembranes.* 1860:2566-2575, 2018.

Structural basis for substrate selection by the translocation and assembly module of the β-barrel assembly machinery. R. S. Bamert, K. Lundquist, H. Hwang, C. T. Webb, T. Shiota, C. J. Stubenrauch, M. J. Belousoff, R. J. A. Goode, R. B. Schittenhelm, R. Zimmerman, M. Jung, J. C. Gumbart, and T. Lithgow. *Mol. Microbiology.* 106:142-156, 2017.

Redox-Driven Conformational Dynamics in a Photosystem-II-Inspired β-Hairpin Maquette Determined through Spectroscopy and Simulation. H. Hwang, T. McCaslin, A. Hazel, C. Pagba, C. Nevin, A. Pavlova, B. Barry, and J. C. Gumbart. *J. Physical Chemistry B.* 121:3536-3545, 2017.

Living on the edge: Simulations of bacterial outer-membrane proteins. A. Pavlova, H. Hwang, K. Lundquist, C. Balusek, and J. C. Gumbart. *Biochimica et Biophysica Acta (BBA) Biomembranes.* 1858:17531759, 2016.

Water distribution in dentin matrices: Bound vs.unbound water. K. A. Agee, A. Prakki, T.

Abu-Haimed, G. H. Naguib, M. A. Nawareg, A. Tezvergil-Mutluay, D. L. Scheffel, C. Chen, S. S. Jang, H. Hwang, M. Brackett, G. Grgoire, F. R. Tay, L. Breschi, D. H. Pashley. *Dental Materials.* 31:205-216, 2015.

Book Chapters

Diverse protein-folding pathways and functions of β-hairpins and β-sheets. C. Balusek, H. Hwang, A. Hazel, K. Lundquist, A. Pavlova, and J. C. Gumbart. In L. Olivares-Quiroz, O. Guzman-Lopez, H.E. Jardon-Valadez, editors, Quantitative Models for Microscopic to Macroscopic Biological Macromolecules and Tissues. Springer. pp. 1-20. 2018.